INFRARED THERMOGRAPHY AND THERMOELASTIC STRESS ANALYSIS OF COMPOSITE MATERIALS AND STRUCTURAL SYSTEMS

A Thesis
Presented to
The Academic Faculty

By

Shane M. Johnson

In Partial Fulfillment
Of the Requirements for the Degree
Master of Science in the
School of Civil and Environmental Engineering

Georgia Institute of Technology

August 2006

INFRARED THERMOGRAPHY AND THERMOELASTIC STRESS ANALYSIS OF COMPOSITE MATERIALS AND STRUCTURAL SYSTEMS

Approved by:

Dr. Rami Haj–Ali, Advisor
School of Civil and Environmental Engineering
Georgia Institute of Technology

Dr. Donald White
School of Civil and Environmental Engineering
Georgia Institute of Technology

Dr. Kenneth Will
School of Civil and Environmental Engineering
Georgia Institute of Technology

Date Approved: July 16, 2006

ACKNOWLEDGEMENTS

My thanks and appreciation go to Dr. Rami Haj–Ali, my advisor, for his guidance, encouragement, persistence, patience and expert advice. Interaction with him has inspired my love of research and has allowed me to seek new and exciting challenges. My gratitude also goes to my colleagues Rani El–Hajjar, Anastasia Muliana, Bo Siou Wei, and Hoan Kee Kim for all the scientific discussions. Thanks are also in order to Bradley Boyce of Stress Photonics Inc. for his expert advise and valuable technical assistance in the field of Infrared Thermographic Stress Analysis. Thanks to Erian Armanios for opening his composites manufacturing lab to my research group, and thanks to Xinyuan Tan for guiding me to manufacturing quality composites.

My admiration and respect goes to a friend at Georgia Tech who has been an amazing source of hope and inspiration: John Bunyasaranand. Finally, my deepest thanks go to my wonderful family especially my sister, Emily (the mother of my beautiful niece, Selma), my grandmother Sally, and most importantly to my mother Donna for her endless love and continuous encouragement during this endeavor.

TABLE OF CONTENTS

LIST OF TABLES

LIST OF FIGURES

SUMMARY

This study expands on the work of El–Hajjar and Haj–Ali on a quantitative thermoelastic strain analysis method for composite materials. Computational models for various prepreg and thick–section composites are validated with experiments using this quantitative strain analysis method. This study provides this thermomechanical calibrations for prepreg S2–glass/epoxy, Carbon/epoxy, and pultruded E–glass/polyester. A research collaboration with the Institute of Paper Science and Technology (IPST) focused on infrared thermography for defect detection in wood and fibrous materials and structural systems. This study provides some detailed information on various testing setups for fiber and corrugated board systems to analyze anomalies and manufacturing defects. Quantitative infrared thermography is suggested as a preferred method for assessing the bond quality in corrugated paper systems. Methods for tracking full–field thermal data during fatigue have been developed for FRP composites. The temperature changes on the surface of an FRP composite caused by damage during fatigue are tracked and thermoelastic stress analysis (TSA) technique is developed to relate the surface deformation to the IR emission. Infrared thermography is developed for fatigue damage detection in FRP composites with stochastic methods for analyzing this full–field data. Future damage detection techniques in aging aircraft will require quantitative and non–contact nondestructive evaluation (NDE) methods especially for composite components. Infrared (IR) thermograpy techniques are qualitatively used to assess and indirectly infer the durability of structural systems. A research collaboration with Lockheed Martin for non–destructive evaluation of composite lap shear joints led to a development of thermoelastic stress analysis techniques for evaluation aerospace structures. Infrared thermography is used to investigate failure initiation and progression in composite lap shear joints.

CHAPTER 1

INTRODUCTION

1.1 Thermography

This chapter presents a literature review of the significant studies characterizing the use of infrared thermography and thermoelastic stress analysis for composite materials and structural systems. In addition, a review of fatigue damage detection in composite materials is presented. The final section of this chapter will outline the objectives and research approach of the present study.

Thermography is the science of measuring temperature changes on the surface of materials due to stress generated thermal fields (SGTF) or externally applied thermal fields (EATF). Thermography is a non–destructive investigation (NDI) tool that allows remote sensing capabilities to detect imperfections or characterize materials. This NDI tool typically requires a sensitive infrared camera capable of detecting temperatures changes less than 0.05 mK. Sensitivities commonly reported during the 1980's were 0.1K, and in many cases trouble with data measurements was reported due to ambient conditions. Since that time, methods to process and measure thermal data such as Stress Pattern Analysis by Thermal Emission (SPATE) where points are scanned in a point–by–point manner under adjustable computer control have developed into fast and accurate full–field Thermo–elastic Stress Analysis (TSA) methods. SPATE methods required 1–2 hours to obtain a single image scanning 50 points per second. Thermoelasticity measurement systems today have a thermal resolution of at least 1 mK for a full–field image with exposure times of 1 minute or less. This temperature sensitivity allows for more sophisticated remote sensing capabilities to exploit damage and damage progression in materials and structural components.

Materials must be excited to expose imperfections. Thermography can be used to detect anomalies spatially because imperfections disrupt heat transfer. An excitation source is the heat source that introduces energy to cause heat energy transfer to occur. Excitation sources can be applied by externally applied thermal fields or by mechanical means for stress generated thermal fields. In either case the thermal field produced is dependent on the emissivity of the material investigated. Emissivity is the ability and efficiency of a material to emit, reflect, or absorb energy. The choice of EATF or SGTF depends on the application, service conditions, material properties, and experience. In the field, the service conditions such as vibrations may be used to excite the material. In many cases discrimination of damage effects is difficult, and the particular method of IR–thermography used is based on the desire to illuminate and excite the particular imperfections of interest.

1.2 Quantitative Thermography and Thermoelastic Stress Analysis in Composites

Quantitative infrared thermography NDE methods are non–contact full–field techniques whereby an IR camera with digital sensors is used to detect small changes of temperature due to different sources. The later can be in the form of an irreversible applied mechanical load, direct heat source, ultrasonic stress waves, among others. The overall goal is to subject the structure or the material to thermomechanical deformation that produce spatial variations in the surface temperatures and allow correlation between measured IR field and the stress or strain on the surface. Under adiabatic and reversible conditions in isotropic materials, the application of a small cyclic load will induce small and repeated variations in temperature that are proportional to the sum of principle stresses. Kelvin (Thomson, 1878) was the first to propose this thermoelastic principal. He used thermodynamics–based derivations to obtain a linear relation between the temperature change and the first stress–invariant. The recent advances and affordability of charged–coupled–device (CCD) cameras, with fast acquisition systems, have

lead to a powerful and quantitative thermoelastic stress analysis (TSA) measurement techniques. The first invariant of the stress can be measured on the surface of loaded coupons made of homogeneous materials. TSA has been also applied in composite materials to measure stresses in thin laminated composites with and without damage. Limited attention has been directed to quantitative TSA in multi–layered fiber reinforced plastic (FRP) composite materials. In laminated composites, several difficulties may arise in the use of TSA, such as the effects of mean stress and frequency dependent testing. Temperature diffusion and non–adiabatic approaches have been proposed to model the thermoelastic effect in laminated composites. Dunn (1993) used a mathematical model to account for the thermal conduction in the top epoxy layer of a graphite/epoxy composite. Kyriakopoulos et al. (1992) used heat conduction finite element analysis to quantify the TSA signal in the absence of adiabatic conditions. In the case of thin laminates, the IR camera was found to detect temperature changes on the surface ply alone. Van Hemelrijck et al. (1992) utilized a non–adiabatic theory approach that took into account the interlaminar heat transfer and obtained good correlation between theoretical and experimental results of the surface temperature for a cross–ply carbon/epoxy laminate. The technique was also used for qualitative and limited quantitative studies. For example, Zhang et al. (1989–1990) studied the dependence of the thermal coefficients of thermal expansion, thickness of surface matrix resin, loading frequency, and changes in absolute temperature on the TSA signal. They noticed an effect of the surface resin thickness. By altering the resin thickness, they found that the TSA signal is highest without a surface layer and above a certain thickness the TSA signal is constant–independent of specimen thickness. They related this effect to a lack of heat transfer from the load carrying fibers to the surface at greater thicknesses. They also researched stress concentrations in the knit–yarn fiber intersections in a woven carbon/epoxy laminate. A mean stress effect was observed in the glass/epoxy composite that was studied. Dulieu–Smith et al. (1997) reported test results of a full–field stress

characterization on a woven tee–joint with FRP laminated fillets. Cunningham et al. (2001) used a DeltaTherm IR detection system to characterize damage around a circular hole in a laminated plate with unidirectional E–glass/epoxy.

Johnson et al (2004) showed fatigue damage progression in thick–section composites with Thermoelastic Stress Analysis (TSA). Mackin and Roberts (2000) tracked static damage progression in ceramic matrix composites using TSA on double edge notched specimens. Kageyama et al. (1989) suggested a damage threshold approach based on 3D FEA, and used TSA with linear elastic fracture mechanics to measure the crack propagation in notched carbon/epoxy laminates. Differential infrared thermography was proposed and used to track the damage in $[\pm 45^{o}]$ and $[0/90^{o}]$ type graphite/epoxy laminates by Lohr et al (1987). In their experiment, the measured temperature was seen to decrease as the number of cycles increased due to cracking in the epoxy surface layer. This effect was more pronounced under higher frequencies and made quantitative TSA difficult for these composite material systems. Adding a thick resin surface layer was found to stabilize the TSA signal and attenuate the heat transfer from the carbon/epoxy inner layers. Mackenzie (1989) and Welch and Zickel (1993) investigated the characteristics of the thermal radiation signal emitted from different surface coatings. The solution of Mackenzie for the thermal wave problem characterized the IR flux amplitude from the surface as a function of IR reflection and thermal material properties of the considered substrate–coat–air system. Using material properties of a typical paint coating, a range of thicknesses and applied thermal frequencies was identified to allow the coat to act as a strain witness layer. Barone and Patterson (1998) proposed using a polymeric coating to extract the strain field from TSA measurements. Their method was applied for isotropic substrates. Good correlation between analytical solutions and measured TSA responses was obtained for aluminum plates with circular holes.

El–Hajjar and Haj–Ali (2003–2004) proposed a technique to measure the sum of the direct strains on the surface of thick section and orthotropic composites to the TSA signal obtained

from the surface of the specimen. Their method was verified experimentally and compared favorably with finite–element (FE) simulations of notched and cracked coupons. This method was used to verify damage studies in thick–section composite materials, considered by Kilic and Haj–Ali (2003) and Haj–Ali and El–Hajjar (2003).

1.3 Fatigue Damage Detection of Composite Materials

Damage mechanisms including delamination, transverse cracking, fiber fracture, fiber debonding, matrix cracking, and fiber bridging have been investigated by various traditional and non–traditional tools. Extensometers and strain gauges have been used to characterize static and fatigue damage by stiffness degredation measures. Acoustic emission has been a valuable tool for researchers because many damage mechanisms produce acoustic events, and the location of an acoustic event can be located with a number of transducers and sophistocated data processing software. Dye enhanced X–ray radiography has been used to investigate the extent of damage due to delaminations. Photoelasticy and thermoelasticy can also be used to investigate the strain state on the surface of composite materials to investigate strain redistributions due to damage. The following selection of references has been collected to highlight various traditional and non–traditional experimental techniques for investigating composite material systems.

The failure of a few fibres under fatigue loading can give rise to local stress–concentration in the matrix and at the fibre–matrix interface leading to the development of fatigue damage. Damage may also develop at local microdefects such as misaligned fibres, resin rich regions, or voids (Matthews et al., 1994). Fatigue damage mechanisms can be complicated and may not be characterized using a single stiffness measurement. Talreja (1987) described the need to use four stiffness properties in order to characterize the fatigue induced damage in a unidirectional glass /polyester specimen. Different damage mechanisms can effect the transverse and shear modulus whereas, such as matrix microcracking, while others reduce the axial modulus. Several studies have recently been performed to identify fatigue damage mechanisms. Zhang et al.

(1990) proposed a thermoelasticity theory for estimating damage in anisotropic materials and using the TSA method. The effective damage tensor was evaluated based on the TSA measurements. They assumed that the degree of damage can be expressed as a function of effective area. It was shown, for glass/epoxy laminates, that there was no significant difference between the values measured from the effective modulus using those from the extensometer. Luong, M. P. (1998) studied the fatigue limit of metal using IR camera as a non–destructive method. He suggested that damage and failure process can be analyzed and described in terms of thermoplasticity using infrared thermography. Thermoplasticity can indicate the occurrence of intrinsic dissipation and it can be used to evaluate the fatigue strength. Bremond et al. (2001) also illustrated the advantages of infrared theromography as a non–destructive method showing stress concentrations developing as a result of cracks approximately ten microns in size growing with increasing load on an automotive component. Kageyama et al. (1989) suggested a damage threshold approach based on 3D FEA, and used TSA with linear elastic fracture mechanics to measure the crack propagation in notched carbon/epoxy laminates. Differential infrared thermography was proposed and used to track the damage in $\pm 45^{o}$ and $0/90^{o}$ graphite /epoxy laminates by Lohr et al. (1987). In their experiment, the measured temperature was seen to decrease as the number of cycles increased due to cracking in the epoxy surface layer. Xian et al (1986) investigated the fatigue damage of carbon/epoxy laminates with and without notches. The three stages of heat generating process (the initial temperature rise, the equilibrium stage and further temperature increase) were observed with IR camera during the fatigue test. A similar result was observed in the paper presented by Wang et al. (2000). They investigated the fatigue behavior of superalloy manufactured with Co–Cr materials using IR camera. In their paper, another stage called final temperature drop was added to the three stages. El–Hajjar and Haj–Ali (2003, 2004) proposed a technique to measure the sum of the direct strains on the surface of thick section and multi–layered composites. The TSA signal obtained from the surface of the

specimen was related to the sum of the direct strains. Damage in thick–section composite materials used in this study was also considered by Kilic and Haj–Ali (2003) and Haj–Ali and El–Hajjar (2003). Characterization of the fatigue damage process in the FRP composites is important in developing fatigue and fracture criteria. Infrared thermography provides a means of measuring the temperature changes on the surface due to the applied cyclic loading. In this paper, a thick–section pultruded FRP composite will be monitored in real–time to detect the progression of fatigue damage. An attempt is made to characterize the damage evolution with respect to the temperature response in thick–section FRP composites using an IR–TSA technique in lieu of using several strain gages to measure different stiffness properties as suggested by Talreja (1987).

O'Brian et al. (1993) investigated damage and failure of angle ply laminated composites at or near the free edge noting that laminate plate theory may be unconservative. They investigated laminates using 3D FEA for each configuration looking at in–plane shear and transverse normal stresses as indicators of a problem with laminate plate theory. In–plane transverse tensile stresses have the greatest magnitude at the free edge of the laminate, and laminate plate theory uses the minimum values in the interior of the laminate. The experimental part of this study employed microscopes and X–ray radiography on straight coupons of AS4/350–6 graphite epoxy prepreg with $[0_2/\theta_2/-\theta_2]_s$ lay–ups where $\theta = (15, 20, 25, 30)$. O'Brian et al. developed delamination models showing delaminations starting from the free edge and growing across the straight coupon at an angle θ. Strain energy release rate solutions were introducted for local delaminations from matrix cracks, and these measures were used to describe the load–life fatigue behavior of angleply laminates.

Scrivner investigated the effects of stress ratio on edge delamination characteristics in AS4/3502 $[\pm 25_2/90]_s$ graphite/epoxy laminated composites. Delamination onset was defined as 5% of the laminate width in 1" by 12" straight coupons. The [25/90] interface was monitored

with a microscope at 9x magnification because this area exhibits the maximum mismatch of Poisson's ratio. Dye penetrant–enhanced x–ray radiography was used to determine the damage state of the laminate. They showed S–N curves where delamination onset was defined as the final state. They also used delamination growth rate curves (da/dn vs Gmax/Gc) to show that the rate of delamination growth increased with increasing strain energy release rate. FEM was used to determine the strain energy release rate for a given delamination, and a power law relationship was used to fit the delamination growth rate curves.

Swain et al. (1993) investigated the effect of interleaves on the damage mechanisms and residual strength of notched composite laminates subjected to axial fatigue loading. Interleaving is the act of adding adhesive layers between plies. The effect of interleaving is to locally strengthen ply interface by reducing interlaminar stresses and to require more energy to propagate a delamination than conventional laminates. For this study the authors chose AS4/985 and AS4/1808 carbon epoxy laminates in a $[0/45/90/-45]_{2s}$ and $[0/45/90/-45]_{4s}$ respectively with an open–hole geometry. They described the effect of interleaving with normalized stiffness vs. normalized life curves and by looking at residual strength. Faituge loading of the laminates was executed at 10 Hz with R=0.1, and at specific intervals the test was stopped and a stiffness value was obtained by measuring the strain with a 1 in gage length extensometer centered on the notch. Delamination originated at the center hole and specimen edges and propagated inward. Predominant delamination occurred at the outer [0/45] interfaces. The authors noted that 0 degree fiber fracture was not a relevant damage mechanism. The stiffness values were calculated by dividing the applied stress by the measured strain. In this case the strain was measured by a 1 in gage length extensometer centered on the notch. The authors found that interleaves did not suppress delamination, but they did slow delamination growth rate. Swain et al. suggested interleaving at critical locations for notch blunting effects to reduce laminate mass and improve stiffness. The authors outlined specific specimen preparation procedures followed for

fabrication of the open–hole specimens such as cutting with a diamond abrasive saw and drilling the .25 in hole with a diamond abrasive core drill. During drilling, the back of the specimen was supported with plastic to prevent delamination.

Motivated by a lack of accurate models that predict changes in stress distribution and corresponding changes in residual properties during fatigue damage development Bakis et al. (1989) began an experimental investigation of the interaction of fatigue damage, the global state of deformation, and the residual strength, stiffness, and life in two contrasting open–hole graphite/epoxy laminates under fully reversed cyclic loading. The experimental study involved a number of non–destructive evalutaion tools to investigate Cycom AS4/1808 graphite/epoxy laminates with $[0/45/90/-45]_{4s}$ and $[0/45/0/-45]_{4s}$ lay–up configurations. Surface deformations were inferred from the measurements of surface strains with photoelasticy and measurements of dynamic, adiabatic temperature change during cyclic loading of the specimen using an Ometron Incorporated SPATE 8000. An effective secant stiffness of the specimen was monitored with a 1 in extensometer centered on the notch. The group related stiffness to the current damage state using dye penetrant to quantify the damage state. They outlined a testing sequence to take x–ray radiography, stiffness, residual strength, photoelasticy, and thermography measurements. Photoelasticy and thermography were to be used three times during the fatigue life of the specimens. Line interrogations at specific locations on the notched specimen were plotted and compared for the photoelstic and thermographic measurements. The fatigue lifetimes of interest were between 5,000 and 20,000 cycles. The group noted that thermography showed growth of a region near zero thermal emission around the notch, and they related this growth to surface ply fracture and delamination. The group qualitatively related residual strength to changes in stress distributions noticeable with IR–images and noticed redistributions of strain around damage zones. The group prepared the specimens with flat black paint for high, uniform emissivity and diffuse surface finish.

Reifsnider et al. (1977) expanded on the work of Pagano and Pipes to develop an understanding of on the interlaminar, normal, and shear stresses distribution on delamination of quasi isotropic graphite/epoxy laminates. An experimental study of two quasi isotropic stacking sequences utilizing ultrasonic pulse echo and high magnification microscopy showed that the difference between Type I: $[0/\pm 45/90]_s$ and Type II: $[0/90/\pm 45]_s$ is a difference in the distribution of interlaminar stresses through the thickness of the laminate. They showed that for a Type I laminate due to an in–plane loading, a tensile normal stress throughout the thickness with a maximum at the [–45/90] interface where delamination is expected. They showed that for a Type II laminate that delamination is not predicted for this laminate for to an in–plane loading because interlaminar stresses are compressive. Delamination does occur in Type II at the grips due to cyclic loading and local peculiarities of the stress field at the grips. The group pointed out a interaction effects between delamination and transverse cracking.

Lessard et al. (1991) investigated the initiation and progression of damage for the compression response of composite open–hole specimens. Load shortening measurements, microscopy, and dye–enhanced x–radiography were used to investigate the load–deflection compressive response, the damage progression before final failure, the ultimate load of failure for each specimen, the corresponding modes of failure, and the effect of ply clustering for various cross ply, angle ply and quasi–isotropic lay–ups. Out of plane displacements are restrained for all compression testing. An extensometer mounted over the open–hole measures axial strain. They found that ply orientation significantly affects damage mechanisms as well as initiation and progression of damage of composites in compression. Notched $[(\pm 30)_6]_s$ specimens did now show damage prior to failure where as the $[(0/90)_6]_s$ specimens showed cracks developing along 0 degree lines in the 0 degree layers emanating from the hole boundary.

Bakis et al. (1991) investigated the adiabatic thermoelastic effect in AS4/3502 and T300/5208 carbon/epoxy prepreg laminated composites. Straight coupon geometries of various

lay–up sequences were tested at different frequencies, and the group found no practical frequency range between 0.5 and 50 Hz in which purely adiabatic deformations occurred in the composite. Bakis et al. hypothesized that the nonadiabatic effects present during cycling of laminated composites is due to either time–dependent viscoelastic deformations in the epoxy resin or a decreasing Poisson's ratio. They also reported that the available thermoelastic properties are questionable for the dynamic problem. Thermoelastic stress analysis images were taken at 30 to 40 percent of specimen's ultimate strength to prevent damage development during a scan. Also, the SPATE 8000 system in 1989 was capable of producing one full–field image in a 2 hour scan. Two quasi–isotropic T300/5208 laminates with stacking sequences of $[45/90/-45/0]_s$ and $[0/90/\pm 45]_s$ with an open–hole type geometry should theoretically have globally identical strain field. The group showed that two quasi–isotropic laminates resulted in different measured thermoelastic emission patterns for different stacking sequences. The group suggested that these different patterns in globally identical strain fields could not have been predicted without a micromechanical or lamina level analysis.

1.4 Present Study

This study expands on the work of El–Hajjar and Haj–Ali on a quantitative thermoelastic strain analysis method for composite materials. El–Hajjar and Haj–Ali verified fracture mechanics computational models for thick–section pultruded E–glass/polyester and E–glass/vinylester composites with experiments using this quantitative strain analysis method. In chapter 2 this study provides this thermomechanical calibrations for prepreg S2–glass/epoxy, Carbon/epoxy, and pultrueded E–glass/polyester.

A research collaboration with the Insitute of Paper Science and Technology (IPST) focused on infrared thermography for defect detection in wood and fibrous materials and structural systems. This study presented in chapter 3 provides some detailed information on various testing setups for fiber and corrugated board systems to analyze anomalies and manufacturing defects.

This study also suggests the use of quantitative infrared thermography for a preferred method for assessing the bond quality in corrugated paper systems.

Methods for tracking full–field thermal data during fatigue have been developed for FRP composites. The temperature changes on the surface of an FRP composite caused by damage during fatigue are tracked and thermoelastic stress analysis (TSA) technique is developed to relate the surface deformation to the IR emission. Chapter 4 presents infrared thermography for fatigue damage detection in FRP composites with stochaistic methods for analyzing this full–field data.

Future damage detection techniques in aging aircraft will require quantitative and non–contact nondestructive evaluation (NDE) methods especially for composite components. Infrared (IR) thermograpy techniques have been qualitatively used to assess and indirectly infer the durability of structural systems. IR–NDE tests to ascertain the health and integrity of the structure over time, especially around connection areas and other critical locations where potential damage can occur. Quantitative NDE–IR methods have received limited attention, especially in composite materials, because these require rapid data acquisitions and signal processing coupled with high resolution and full–field IR. These are past limitations of electronic hardware and the software. One objective of this research was to examine composite components under loading and extract deformation measures from the emitted IR field of the tested components. A research collarobation with Lockheed Martin for non–destructive evaluation of composite lap shear joints led to a development of thermoelastic stress analysis techniques for evaluation aerospace structures. Chapter 5 presents a study on infrared thermography for failure initiation and progression in composite lap shear joints. This study also presents some generic finite element results for analyzing bond characteristics in lap joints.

A new methods is presented for determining stress intensity factors in composite materials. This new method utilizes the quantitative thermoelastic strain analysis method described in

Chapter 2 together with computational analysis of the full–field thermoelastic data around a crack tip to measure fracture parameters for mixed mode loading conditions. Chapter 7 presents a thermoelastic determination of stress intensity factors for multi–layered materials.

CHAPTER 2

A Quantitative Thermoelastic Strain Analysis Method

2.1 Methodology

A experimental thermoelastic stress/strain analysis (TSA) technique is presented to measure the sum of the normal surface strains in FRP composites. The new method proposed by El–Hajjar and Haj–Ali (2003) can be used to verify computational models by providing a full–field measurement of the strain (or stress) invariant. This chapter will present the derivation for this quantitative TSA method, steps to acquire a thermomechanical calibration constant, and a verification of a computational model with a composite open–hole specimen. To obtain the thermomechanical calibration constant the composite material tested is given an isotropic surface coat that acts as a strain witness and provides optimal thermal conditions for TSA. During the calibration, the infrared (IR) signal from the coat is measured, and strains in the axial and transverse loading directions are recorded while the specimen under a uniform state of stress is cyclically loaded. This quantitative thermoelastic strain analysis method allows a single material constant, comprised of the thermomechanical properties of the composite, to be calibrated such that the measured IR signal can be related to the sum of the in–plane strains. The theoretical derivation of this new method assumes steady state, adiabatic conditions and applies a thermomechanical theory to the case of multi–layered composite materials. The proposed method is validated by its application to Carbon/epoxy, S2–glass/epoxy, and thick–section E–glass/polyester composites. Finally, this method is used to verify computational models of unidirectional carbon/epoxy and S2–glass/epoxy FRP systems under multi–axial states of stress.

2.2 Derivation

The formulation directly relates the measured TSA signal to the sum of the in–plane strains in a coated composite laminate. Some basic assumptions on this formulation are applied beginning with a basic thermoelastic equation, mechanical properties of the surface coat, and simplifications on the structural characteristics of laminated composites. The elastic stiffness of the isotropic coat is assumed to be negligible. The thermomechanical material response of the coat is considered linear elastic and independent of the mean applied stress and loading frequency. Figure 2.1 schematically illustrates a typical layered composite with surface coatings. The surface coating is assumed to account for the thermoelastic response. The individual layers are assumed to be perfectly bonded together. and the TSA signal is interpreted to represent the change in the sum of the in–plane strains of each layer. The constant of proportionality that relates the TSA signal to the change of the sum of orthogonal surface strains is a thermomechanical material constant and can be calibrated experimentally from uniform TSA measurements when the strains are known. A uniform TSA signal can be obtained from cyclic loading of straight coupon geometries of coated FRP composites.

Assuming a perfect bond and displacement continuity between the layers of the orthotropic composite results in the same in–plane strains in all the layers when a uniform in–plane loading is applied. Assuming traction continuity provides a further simplification in which the multi–layered composite has the same uniform out–of–plane stresses. Traction and displacement continuity allow treating the multi–layered composite as a system with equivalent linear anisotropic stress–strain relations.

A thermomechanical relation is necessary to more fully describe the composite system and the coupling required to relate the TSA signal to the sum of the in–plane strains. A basic equation governing the thermoelastic effect is given by (Wong, 1987):

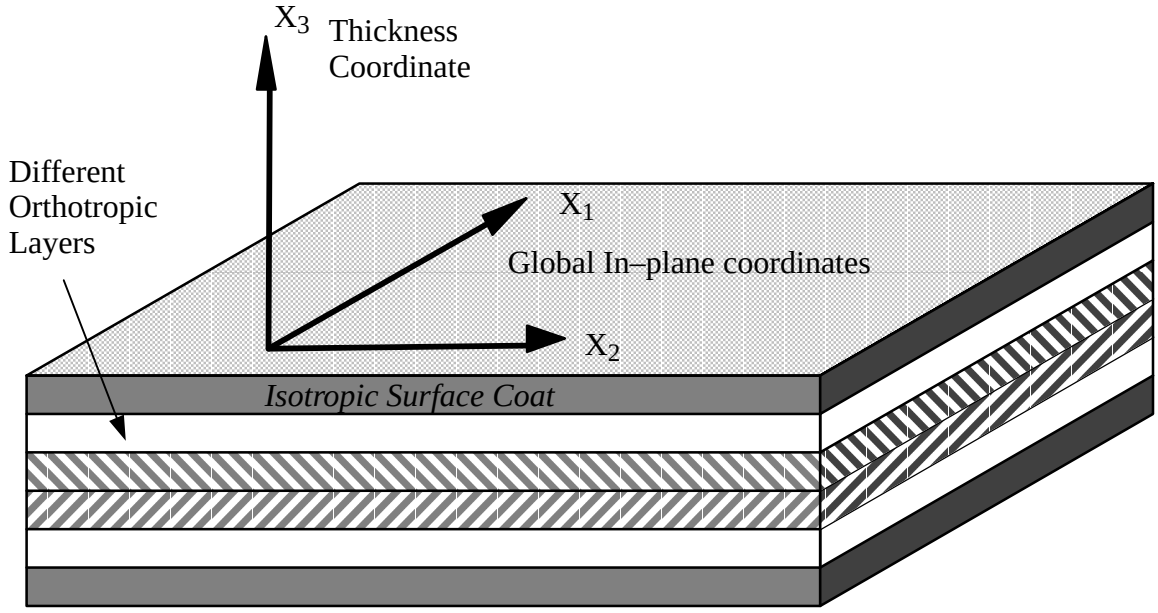

Figure 2.1. Schematic cross–sectional view of a layered orthotropic composite with surface coatings

$$Q_{i,i} = T \frac{\partial \sigma_{ij}}{\partial T} \dot{\varepsilon}_{ij} - \rho_o C_\varepsilon \dot{T} + \rho_o \dot{R} \tag{2.1}$$

Where Q_i is the heat flux through the surface whose outward directed normal is n_i, T is temperature, σ_{ij} is the stress tensor, ε_{ij} is the strain tensor, ρ_o is the density, C_ε is the specific heat at constant deformation ($\dot{\varepsilon}_{ij} = 0$), and $\dot{R}$ is the heat production rate per unit mass by the internal heat sources. The thermomechanical constitutive law for a linear anisotropic material is given by Hooke's law:

$$d\sigma_{ij} = C_{ijkl} d\varepsilon_{kl} - C_{ijmn} \alpha_{mn} dT \tag{2.2}$$

Where C_{ijkl} is the fourth rank tensor of the material constants, α_{mn} are the coefficients of thermal expansion and dT is the change in temperature. If the material properties are assumed to remain constant with change in temperature, then the stress change in temperature is simply:

$$\frac{\partial \sigma_{ij}}{\partial T} = - C_{ijmn} \alpha_{mn} \tag{2.3}$$

Assuming adiabatic conditions with no internal heat sources $Q_{i,i} = 0$, and $\dot{R} = 0$, Equations (2.1) and (2.3) are combined to give:

$$\rho_o C_\varepsilon \frac{\dot{T}}{T} = - C_{ijmn} \alpha_{mn} \dot{\varepsilon}_{ij} \tag{2.4}$$

Next, assuming small strain theory, and using the incremental form of Equation (2.2) to express for $C_{ijmn} d\varepsilon_{ij}$, Equation (2.4) is rewritten as:

$$\rho_o C_\varepsilon \frac{dT}{T} = - \alpha_{mn} [d\sigma_{mn} + C_{mnpq} \alpha_{pq} dT] \tag{2.5}$$

For the special case of an in–plane transversely isotropic coat under a state of plane stress, the in–plane material properties are equal, $\alpha_{11} = \alpha_{22} = \alpha$, $C_{11pq} = C_{22pq}$, $d\sigma_{33} = 0$. Placing these conditions on Equation (2.5), it is then seen that the thermoelastic effect is dependent only on the in–plane properties:

$$\left[\frac{\rho_o C_\varepsilon}{T} + C_{mnpq}\alpha_{mn}\alpha_{pq}\right] dT = - (\alpha_{11} d\sigma_{11} + \alpha_{22} d\sigma_{22}) = - \alpha(d\sigma_{11} + d\sigma_{22}) \tag{2.6}$$

The general stress–strain relation for the in–plane isotropic coat is:

$$\begin{Bmatrix} \sigma_{11} \\ \sigma_{22} \\ \sigma_{33} \\ \tau_{23} \\ \tau_{13} \\ \tau_{12} \end{Bmatrix} = \begin{bmatrix} C_{11} & C_{12} & C_{13} & 0 & 0 & 0 \\ C_{12} & C_{11} & C_{13} & 0 & 0 & 0 \\ C_{13} & C_{13} & C_{33} & 0 & 0 & 0 \\ 0 & 0 & 0 & C_{44} & 0 & 0 \\ 0 & 0 & 0 & 0 & C_{44} & 0 \\ 0 & 0 & 0 & 0 & 0 & (C_{11} - C_{12})/2 \end{bmatrix} \begin{Bmatrix} \varepsilon_{11} \\ \varepsilon_{22} \\ \varepsilon_{33} \\ \gamma_{23} \\ \gamma_{13} \\ \gamma_{12} \end{Bmatrix} \tag{2.7}$$

The plane stress assumption ($\sigma_{33} = 0$) in this layer allows the out–of–plane strain ε_{33} to be expressed in terms of the in–plane strain components:

$$\varepsilon_{33} = - \frac{C_{13}}{C_{33}}(\varepsilon_{11} + \varepsilon_{22}) = - \frac{C_{13}}{C_{33}} \varepsilon_{\alpha\alpha} \; ; \qquad \alpha = 1, 2 \tag{2.8}$$

The first stress invariant can then be expressed as:

$$\Delta\sigma = \sigma_{\alpha\alpha} = \sigma_{11} + \sigma_{22} = \frac{\left(C_{11}C_{33} + C_{12}C_{33} - 2C_{13}^{\,2}\right)}{C_{33}}(\varepsilon_{11} + \varepsilon_{22}) \tag{2.9}$$

Physically, the infrared detector measures an un–calibrated TSA signal, S, that is directly proportional to a surface temperature change. Equation (2.6) can be used to relate the TSA signal from the surface coat to the change of the first stress invariant through a parameter k_σ:

$$\Delta\sigma = k_\sigma \; S \tag{2.10}$$

Substituting Equation (2.9) into (2.10) results in:

$$\frac{\left(C_{11}C_{33} + C_{12}C_{33} - 2C_{13}^{\,2}\right)}{C_{33}}(\Delta\varepsilon_{11} + \Delta\varepsilon_{22}) = k_\sigma \; S \tag{2.11}$$

Next, enforcing traction and displacement continuity between the layers in orthotropic laminates yields the same in–plane strains in each layer of a medium subjected to in–plane loading. A new constant k_ε can then be defined as:

$$k_\varepsilon = \frac{C_{33}}{\left(C_{11}C_{33} + C_{12}C_{33} - 2C_{13}^{\,2}\right)} \; k_\sigma \tag{2.12}$$

This enables formulating a new thermoelastic equation, similar to Equation (2.10), in terms of the in–plane strains using the new relationship:

$$\Delta\varepsilon_{\alpha\alpha} = k_\varepsilon \; S \qquad \alpha = 1, 2 \tag{2.13}$$

2.3 Experimental Setup

A DeltaTherm DT1500 thermoelasticity measurement system was used to acquire the thermal measurements. The DeltaTherm's infrared array detector synchronized with the applied cyclical loading enables the detection of the transient thermoelastic effect. The infrared detector acts as a transducer, which converts the incident radiant energy into electrical signals. A lock–in analyzer (a signal–processing unit) extracts the thermoelastic information from the detector's output signal by using the reference signal from the loading device. The TSA–IR system uses the reference signal to reject any non–stress related thermal emissions. The frequency should be high enough to prevent heat transfer due to stress gradients during the load cycle. The Delta–Therm has a thermal resolution of at least 1 mK for image exposure times of one minute

or less. Figure 2.2 shows the testing setup along with a schematic of the TSA data acquisition (Figure 2.3). The IR camera captures images at rates of more than 400 frames per second. The applied load signal is used to integrate synchronized TSA images that correspond to peak values of loading. The integration of the captured images is a temporal smoothing process performed over a specified period. In this study, a period of 1–2 min was used. The cyclic load was applied using an MTS 810 servo–hydraulic test system with a 22.2 kN(50 kip) capacity. The accuracy of the recorded strains is within 50 micro–strain and the load is within 0.22 kN (50lb). The tested specimens are coated with black paint (Krylon Ultra Flat) to improve the surface emissivity. Biaxial strain gauges or orthogonal uni–axial strain gauges are mounted on the backside of the specimen, and the strains are recorded as a cyclic loading is applied at a frequency of 5 – 20 Hz.

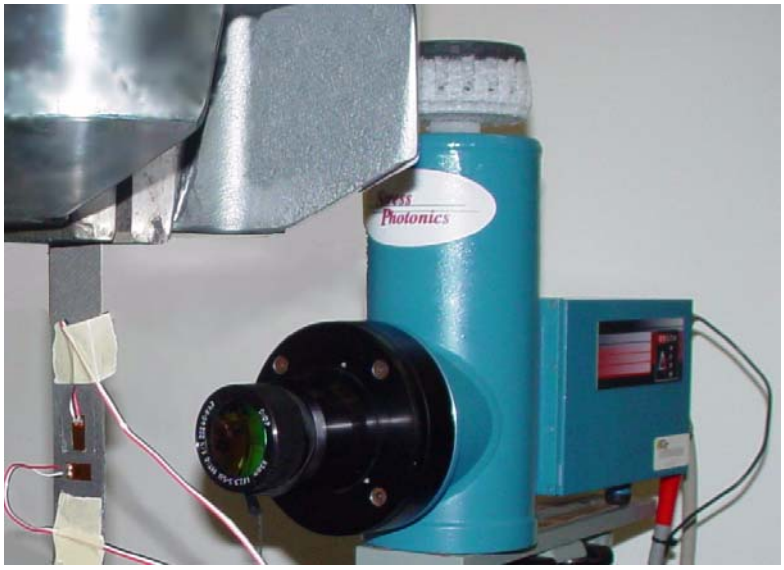

Figure 2.2. Infrared camera used to observe a specimen during a TSA test

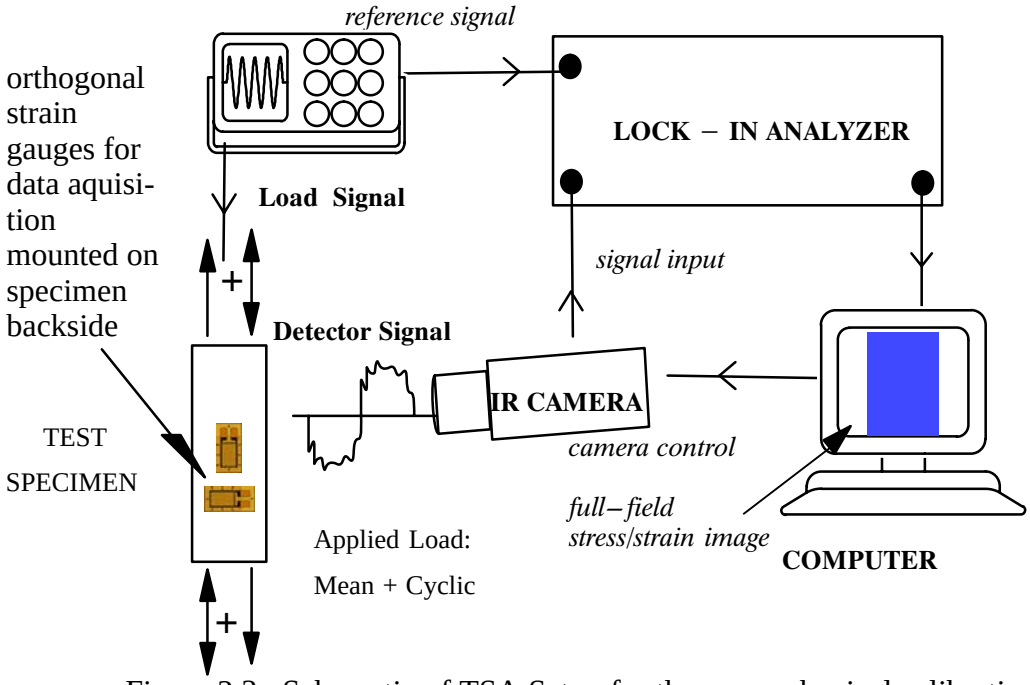

Figure 2.3. Schematic of TSA Setup for thermomechanical calibration

2.4 Static Testing of Various FRP Composites

The proposed TSA method was calibrated for E–glass/polyester pultruded, S2–glass/epoxy prepreg, and Carbon/Epoxy FRP composite systems. The FRP coupons were tested with the load applied parallel and transverse to the major stiffness axis. The mechanical properties of the tested coupons are shown in Table 2.1 The E–glass tension coupons were 25.4 mm (1.00 in.) wide, had 152.4 mm (6 in.) ungripped length and a thickness of 12.2 mm (0.48 in.). The S2–glass tension coupons were 25.4 mm (1.00 in.) wide, had 152.4 mm (6 in.) ungripped length. A uniform thickness of 2.26 mm (0.089 in) was achieved for the $[0_5/90/0_5]$ system using an autoclave, and a uniform thickness of 1.78 mm (0.070 in) was achieved for the quasi–isotropic system using an autoclave. The unidirectional Carbon/epoxy tension coupons were 25.4 mm (1.00 in.) wide, had 152.4 mm (6 in.) ungripped length and a thickness of 1.16 mm (0.046 in.). Biaxial strain gages were oriented in the material directions to measure the surface strains. The TSA effect was calibrated for the linear elastic region of the stress–strain response curve (< 0.25

%) as shown in Figures 2.4, 2.5 and 2.6. Time effects on the stress–strain response during each cyclic load application were not considered significant and the material was assumed to be under steady–state conditions. The effective properties of the Pultruded E–Glass/Epoxy system in Table 2.1 were obtained by Haj–Ali and El–Hajjar in 2003. The stress/strain relationships for the carbon/epoxy and S2–glass/epoxy systems are shown in Figures 2.4, 2.5, and 2.6.

Table 2.1 Effective properties

System	Unit	E_{11}	E_{22}	G_{12}	v_{12}
Pultruded E–Glass/Epoxy	GPa (Msi)	17.1 (2.484)	9.96 (1.444)	3.5 (0.507)	0.283
Carbon/ Epoxy	GPa (Msi)	120. (17.46)	10.5 (1.235)	6.9 (1.010)	0.333
S2–Glass/ Epoxy $[0_5/90/0_5]$	GPa (Msi)	49.4 (7.168)	17.3 (2.830)	13.6 (1.976)	0.229
S2–Glass/ Epoxy $[–45/0/45/90]_s$	GPa (Msi)	26.7 (3.879)	26.7 (3.879)	17.5 (2.536)	0.307

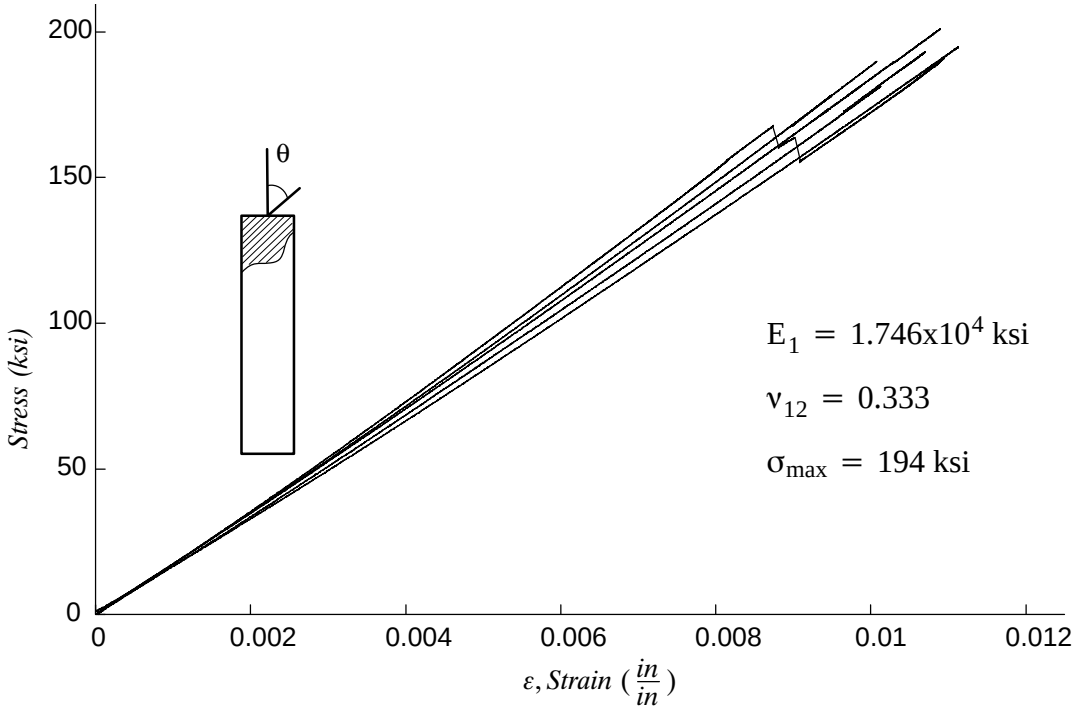

Figure 2.4. Stress vs. strain for 0 degree unidirectional carbon lay–up

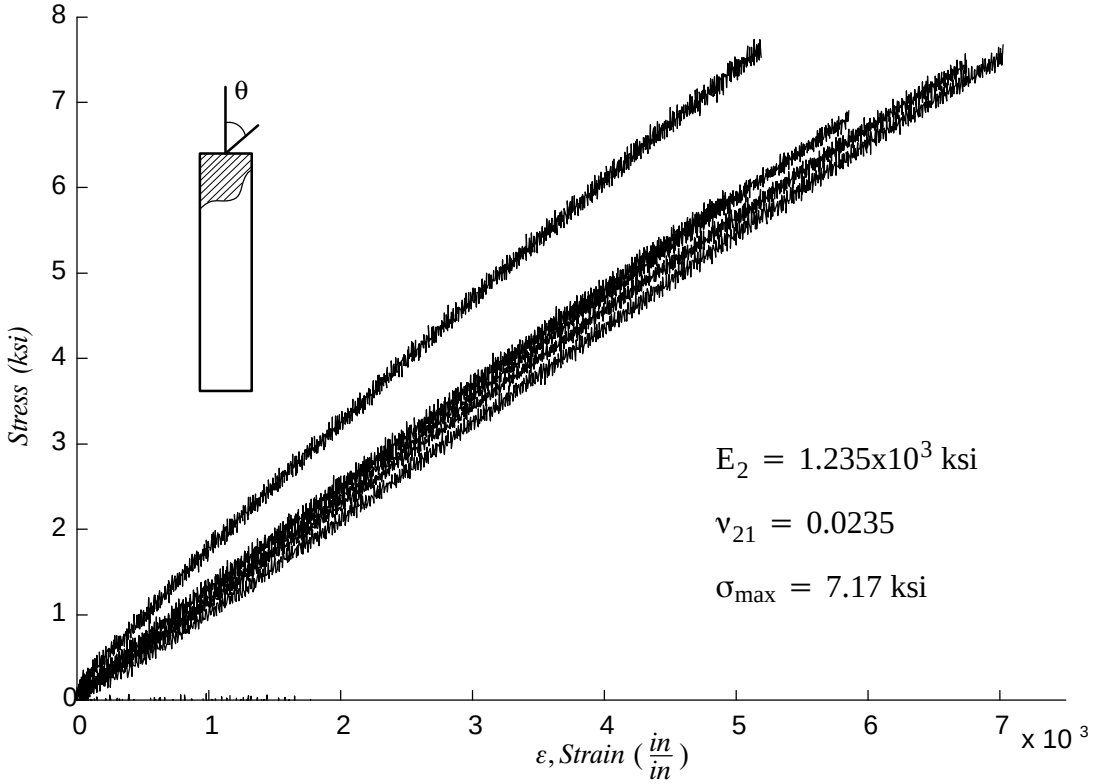

Figure 2.5. Stress vs. strain for 90 degree unidirectional carbon lay–up

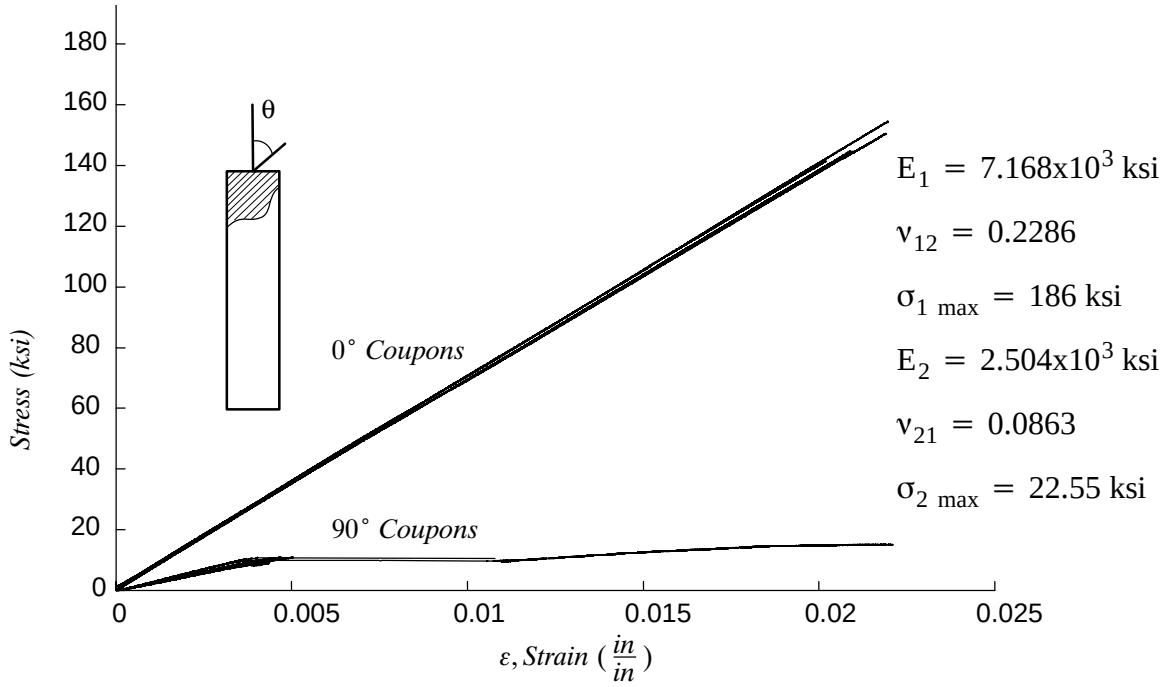

Figure 2.6. Stress vs. strain for HYE E773FR/S2 [0_5/90/0_5] lay–up

2.5 Thermomechanical Calibrations for Various FRP Composites

A calibration shown in Figure 2.7 was repeated in this study for the pultruded system used by Haj–Ali and El–Hajjar in 2003. The thermomechanical constant obtained in this study is 9.8 % lower than the value obtained by their group, 5.5973 x10^4 camera units/(in/in). The difference may be due to differences in the numerical algorithms used to obtain TSA averages for the specimen, ways of processing the strain data to calculate, degrad ation of the camera sensors over time, or variablity and differences in manufacturing of the pultruded E–glass/epoxy plates.

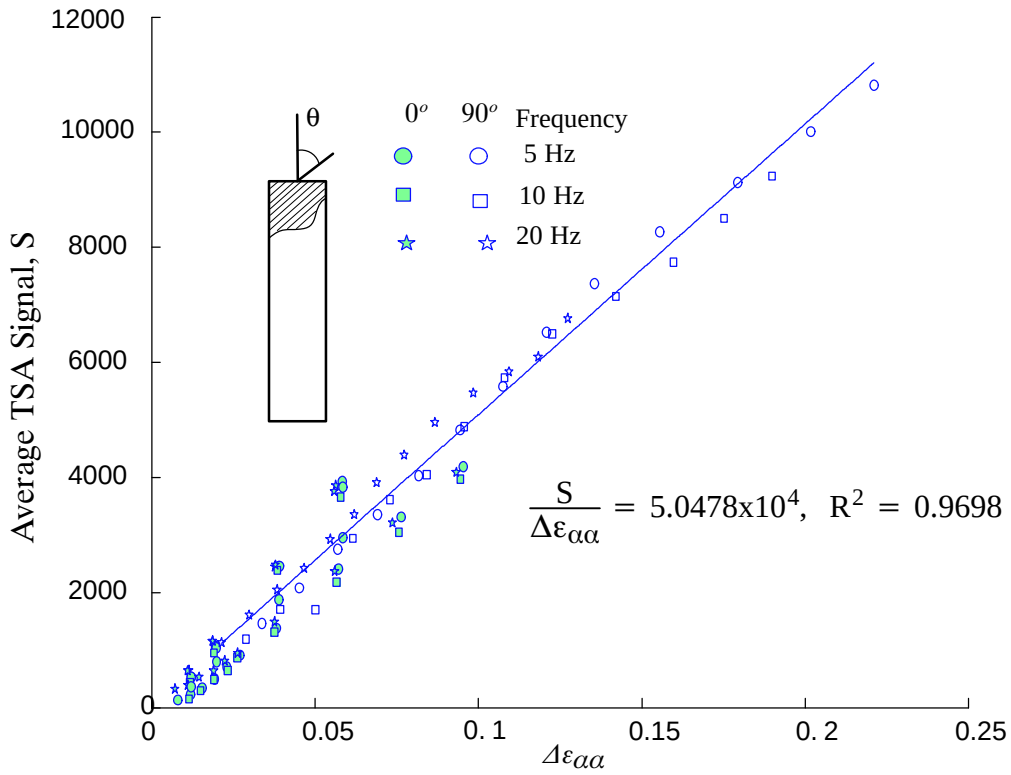

Figure 2.7. Thermo–mechanical calibration for E–glass/epoxy

In the following example, a unidirectional carbon/epoxy system is investigated. The stress/strain relationship is shown in Figures 2.4 and 2.5. Notice in the calibration in Figure 2.8 that the 90º specimens show a slightly different slope than the 0º specimens. One should be aware of verifying computational models 2 distinct calibration constants. The thickness of the surface coat should be considered in this case. It may be necessary to characterize certain layups with 2 calibration constants especially if a proper isotropic coat is not applied.

Also notice in Figure 2.8 that a small number of data points were taken at high frequencies for the larger change in strain values. This is because the MTS machine was not tuned for each frequency. The error in the change in force applied to the specimen was neglected since the relation is in terms of the change in the sum of measured strains and TSA signal.

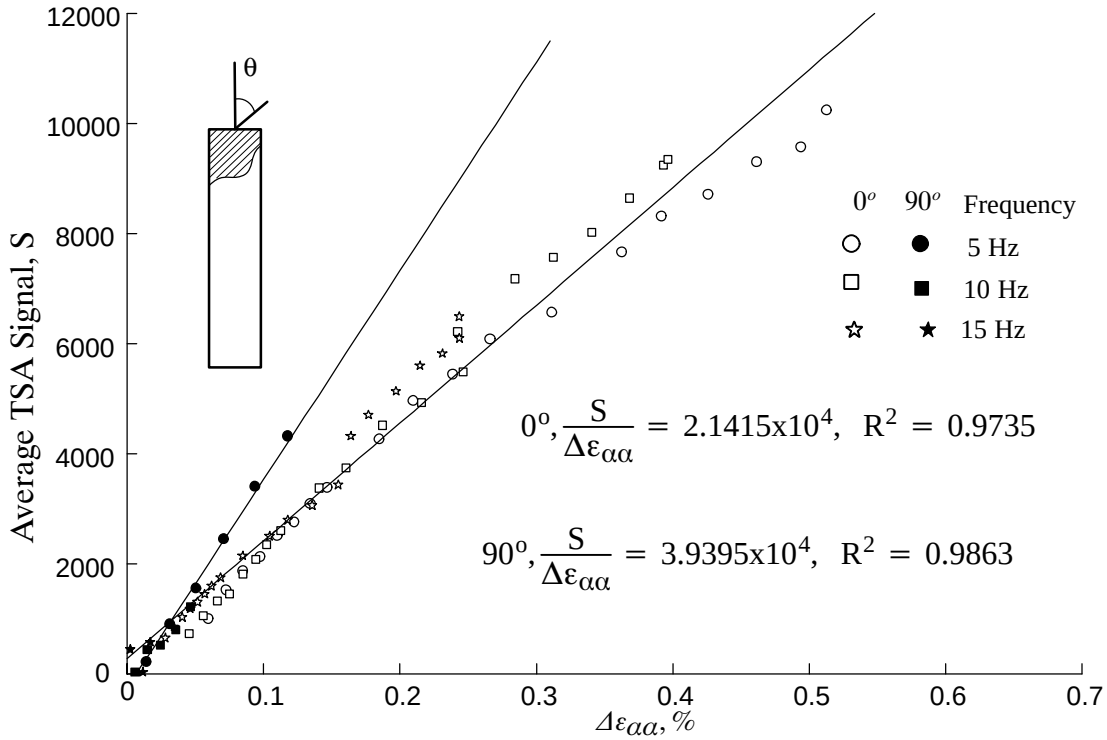

Figure 2.8. Thermo–mechanical calibration for unidirectional carbon lay–up

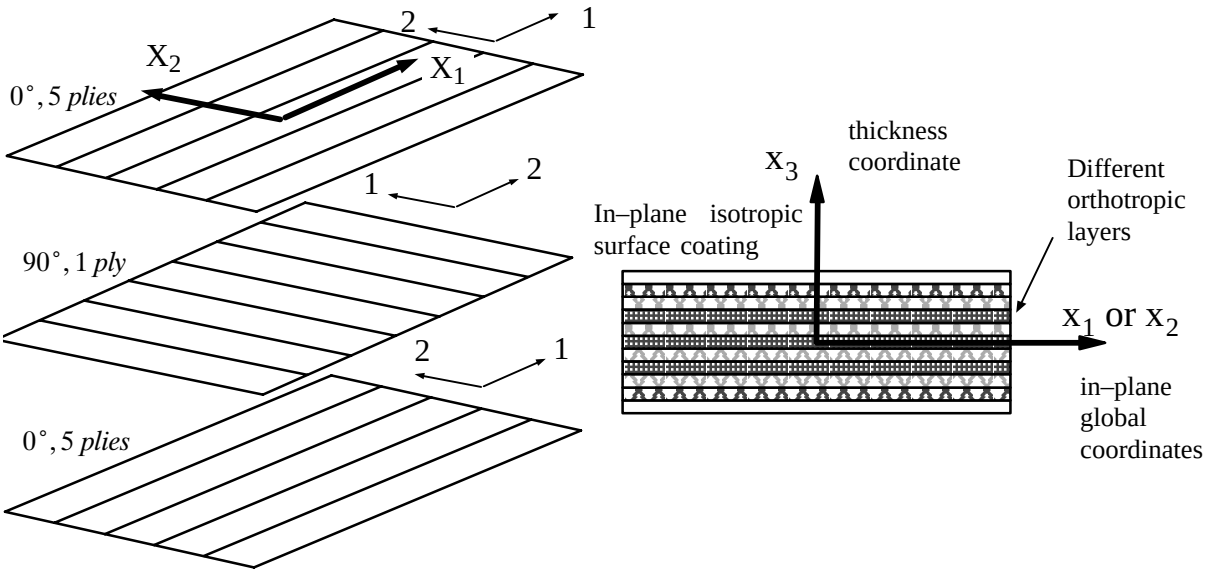

Figure 2.9. HYE E773FR/S2 [0_5/90/0_5] lay–up

Notice in the calibration in Figure 2.10 that the 90º specimens show a different slope than the 0º specimens. The thickness of the surface coat should be considered in this case. It is

necessary to characterize this layups with 2 calibration constants or apply an isotropic coat. An additonal epoxy coating of approximately 0.3 mm (0.12 in) was cured at room temperature to the surface of the $[0_5/90/0_5]$ lay–up. This surface coat was then sprayed with flat black paint and the calibration from Figure 2.10 was repeated, and the result is shown in Figure 2.11. As you can see the isotropic surface coat allows the system to be characterized by a single constant that relates the Thermoelastic signal to the sum of the normal strains.

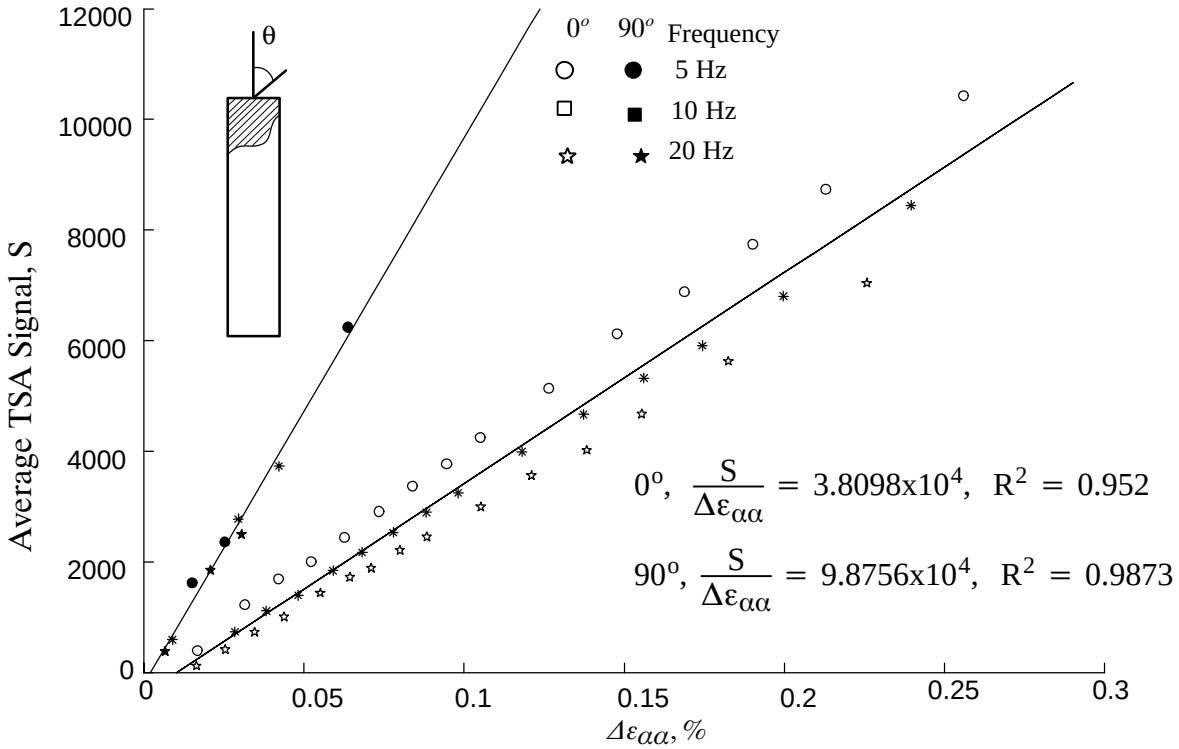

Figure 2.10. Thermo–mechanical calibration for S2–glass/epoxy $[0_5/90/0_5]$ lay–up

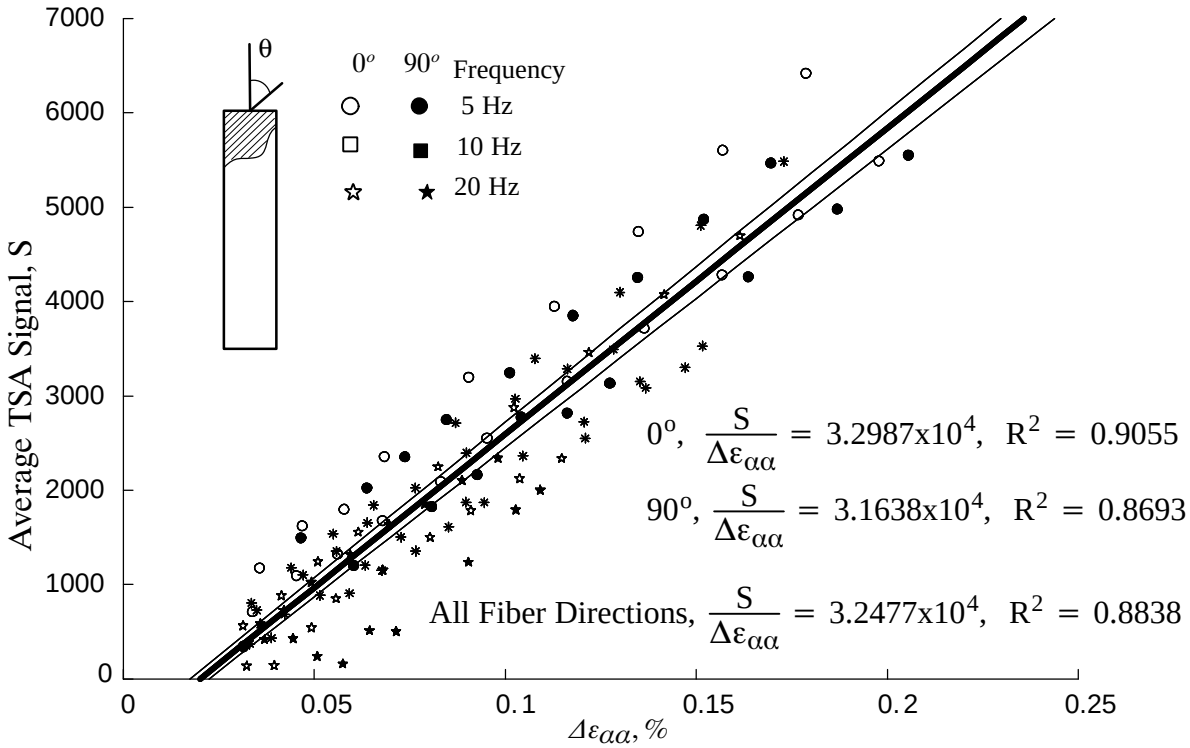

Figure 2.11. Thermo–mechanical calibration for S2–glass/epoxy [0_5/90/0_5] lay–up with additonal epoxy coating

The longitudinal stiffness of the [0_5/90/0_5] system was measured to provide validitiy to the assumption of the negligible stiffness difference in adding the epoxy coating. Table 2.1 shows the values of the standard [0_5/90/0_5], while the properties obtained from the epoxy coated samples are $E_{11} = 42.3$ GPa (6858 ksi) and $E_{22} = 20.4$ GPa (2957 ksi), respectively. These values are within than five percent different than that obtained from uncoated specimens. This change of stiffness due to the epoxy coat can be considered within the experimental error range and justifies using the proposed coat for TSA measurements. The calibration constant labeled "All Fiber Directions", $K_\varepsilon = 3.2477\text{x}10^4$, will be used to validate different coated material systems to show that the epoxy coating is being calibrated in Figure 2.11.

Figure 2.12 shows the themomechanical calibration repeated for a quasi–isotropic S2–glass/Epoxy with a $[-45/0/45/90]_s$ lay–up scheme. This lay–up was chosen because the

surface ply is orientated at –45 degrees from the loading axis. This surface ply tends to change the orientation of the thermoelastic signal with the angle of the surface ply. Two different quasi–isotropic lay–ups should theoretically have globally identical strain field. Bakis et al. (1991) showed that two quasi–isotropic laminates resulted in different measured thermoelastic emission patterns for different stacking sequences. Adding an isotropic surface coat to the quasi–isotropic laminate acts as a strain witness. Two different quasi–isotropic lay–ups with the same added isotropic surface coating should theoretically have the same thermoelastic emission pattern for different stacking sequences. The thickness of the surface coat is the subject for future research.

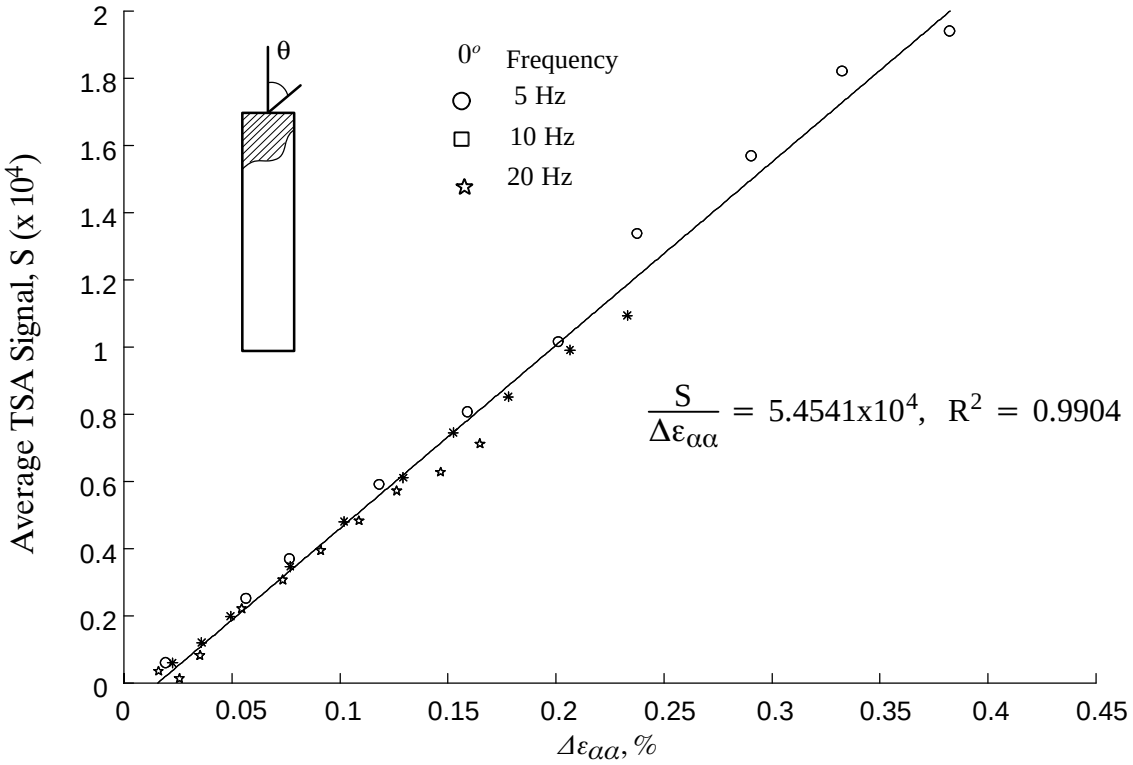

Figure 2.12. Thermo–mechanical calibration for quasi–isotropic S2–glass/epoxy lay–up

2.6 Validation Under Multi–Axial State of Stress

A standard open–hole specimen ASTM D 5766/ D 5766M was chosen for validation of the calibration under a multi–axial state of stress. The specimen dimensions were 1.5 in wide, with a centered 0.25 in hole, and an ungripped length of 6 in, and a thickness of 0.046 in. The specimen was cut so that the major stiffness axis is the axial direction of the loaded geometry. The specimen was sprayed with flat black paint and the force on the specimen was recorded as the system was cyclically loaded. This change in force was later used in computational models.

A quarter symmetry finite element model of the open–hole unidirectional carbon/epoxy system with material properties provided in Table 2.1 was chosen for computational analysis. The specimen geometry and finite element mesh are shown in Figure 2.13. The model consisted of 30,000 of Abaqus's CPS8R elements with symmetric boundary conditions on the quarter geometry. A uniformly distributed load (half of that applied to the actual specimen) was applied to the model, and the sum of the in–plane strains along the horizontal and vertical axes through the center of the hole were plotted in Figure 2.15 through 2.18. The results were used to how the experimental results compared to finite element and to show the effect of adding a surface witness layer.

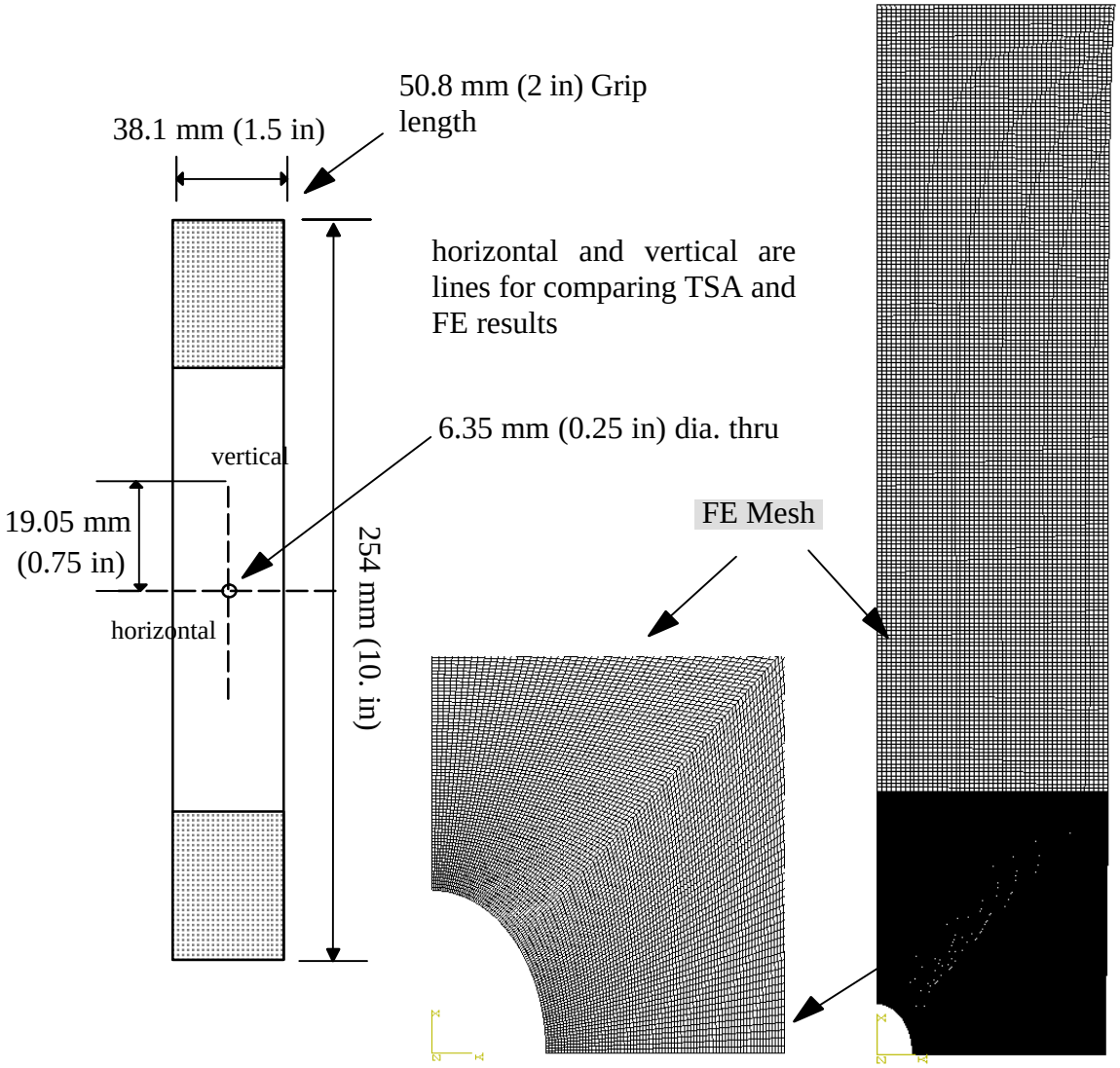

Figure 2.13. Geometry of notched test specimen used to verify the TSA technique and a very refined quarter–model FE mesh used to model the notched specimen

A TSA image of an un–coated unidirectional carbon/epoxy open–hole specimen was taken, and the result is shown in Figure 2.14. Notice in this case a small amount of damage resulted upon drilling the unidirectional composite, and some loose fibers are seen at the hole edge on the left side of the image of the un–coated specimen in Figure 2.14. Future open–hole specimens

were drilled with a brad point drill bit at a low drill speed (600 rpm) as suggested by Mackin et al (2000).

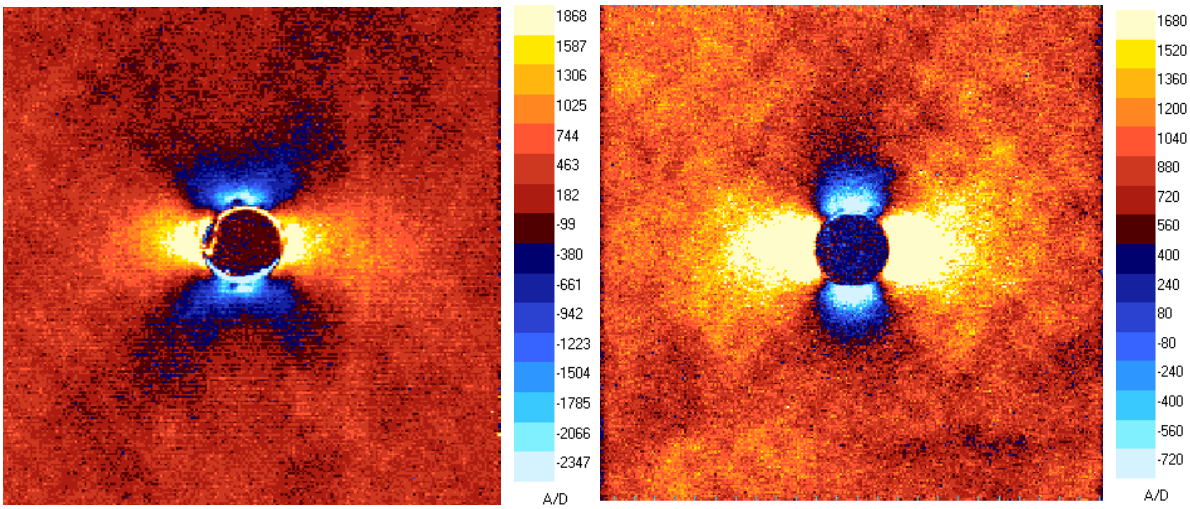

Un–coated Coated

Figure 2.14. TSA images of unidirectional carbon/epoxy

Figures 2.15 and 2.17 show vertical and horizontal line interrogations drawn on the TSA data for a 0 degree specimen through the center of the hole using the 0 degree calibration constant ($k_\varepsilon = 2.1415x10^4$ as shown in Figure 2.8) to scale the data The vertical line interrogation shows thermoelastic data for a 38.1 mm (1.5 in) line through the center of the hole as shown in Figure 2.13. A reasonable accuracy was achieved for model verification using the 0 degree calibration constant with a 0 degree open hole coupon. To verify the proposed calibration, the surface of the specimen must be coated with epoxy or alternative isotropic coat, and the experimental calibration must be re–examined so that a single calibration constant is achieved. In this case however, the 0 degree calibration constant was used because a small error in $\varepsilon_{\alpha\alpha}$ would result from an experimental test where the TSA values are less than 2000 camera units. So within this range of the calibration, a single constant was used to verify a computational model.

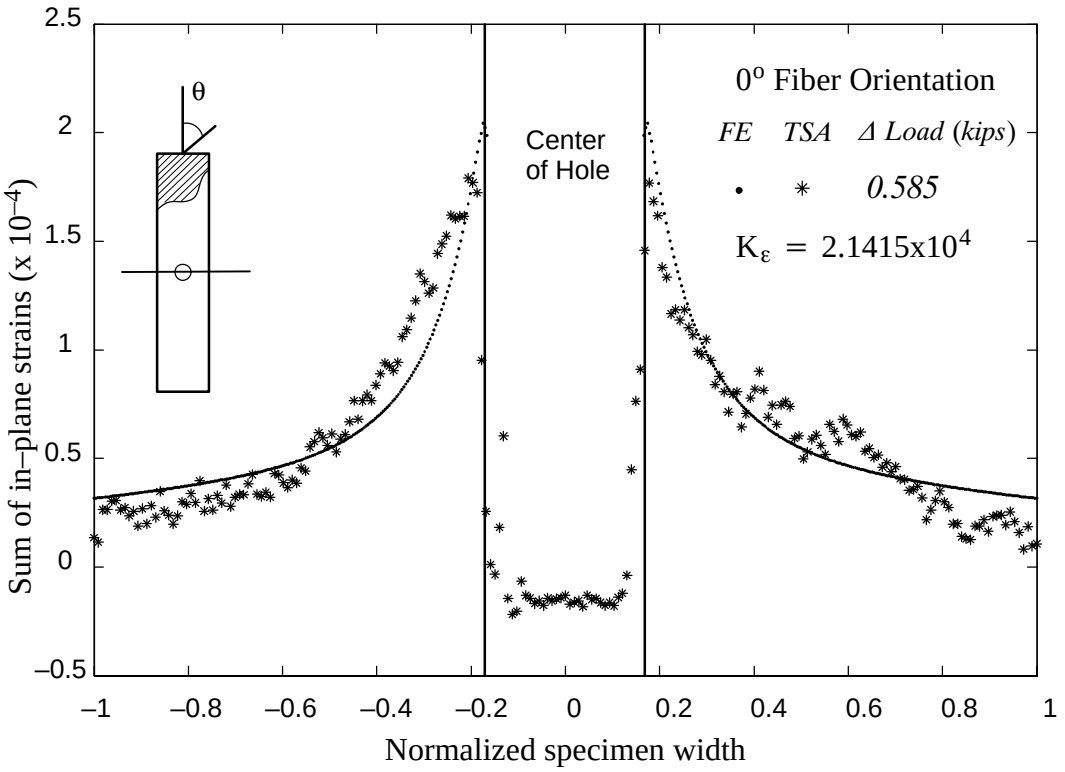

Figure 2.15. Horizontal line interrogation of open–hole geometry for verification of thermomechanical calibration of un–coated unidirectonal carbon/epoxy

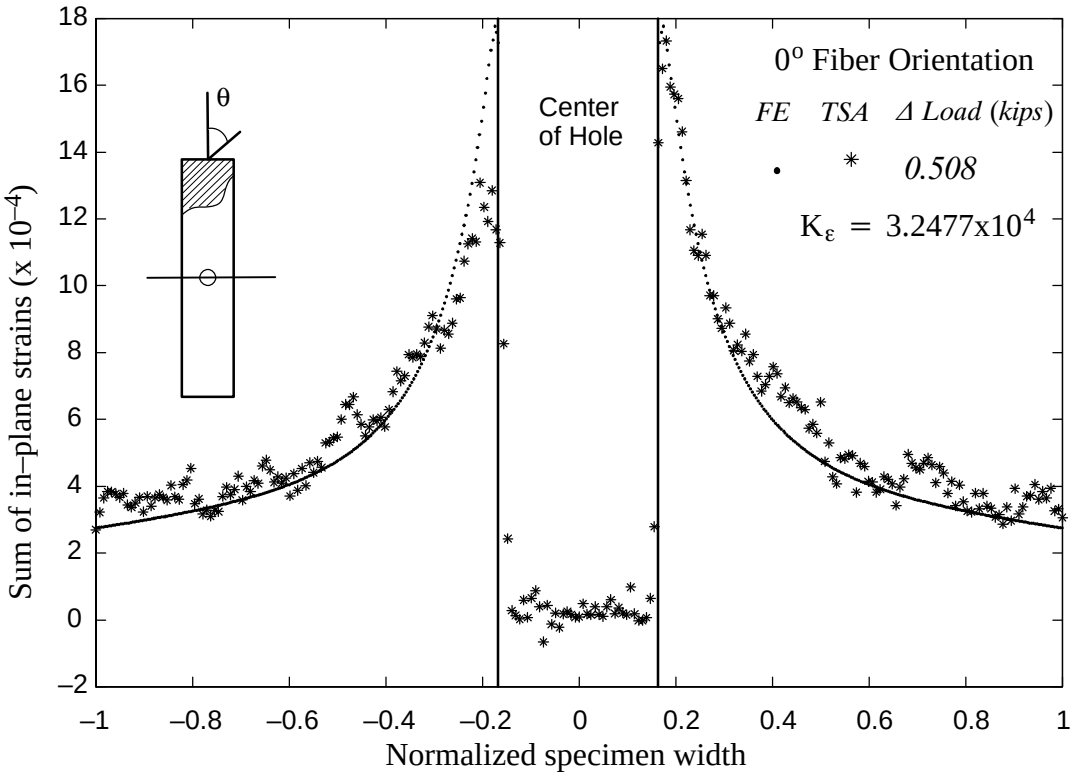

Figure 2.16. Horizontal line interrogation of open−hole geometry for verification of thermomechanical calibration of coated unidirectonal carbon/epoxy

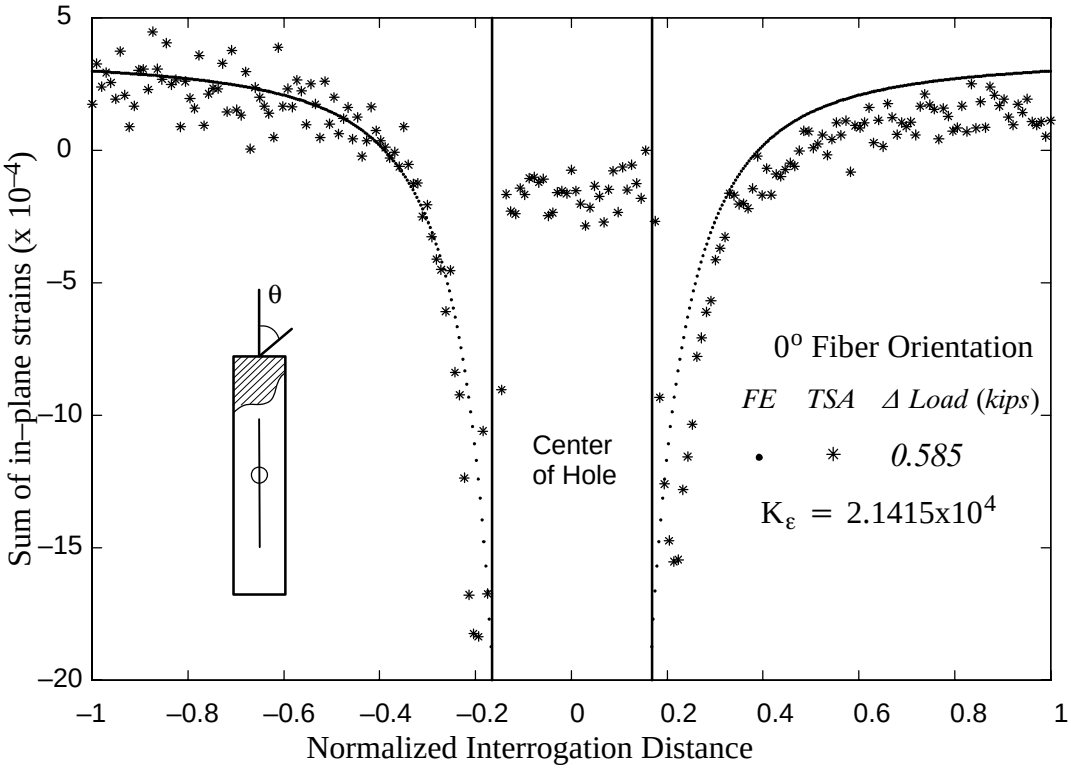

Figure 2.17. Vertical line interrogation of open−hole geometry for verification of thermomechanical calibration of un−coated unidirectional carbon/epoxy

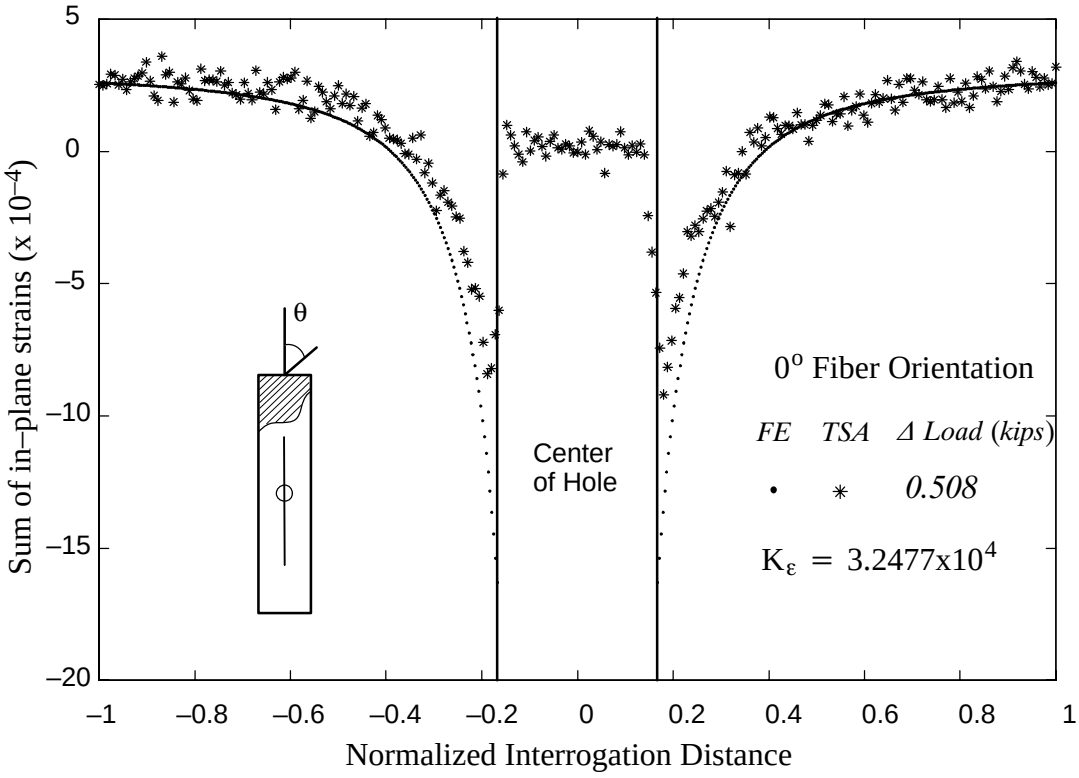

Figure 2.18. Vertical line interrogation of open–hole geometry for verification of thermomechanical calibration of coated unidirectional carbon/epoxy

For validation of the S2–glass/epoxy system the same geometry shown in Figure 2.13 was chosen for validation of the calibration under a multi–axial state of stress. The major stiffness axis is the axial direction of the loaded geometry. The lay–up of the two S2–glass/epoxy systems are quasi–isotropic and a $[0_5/90/0_5]$ lay–up as shown in Figure 2.9. In the case of the $[0_5/90/0_5]$ lay–up, one 90^o ply is placed in the middle of the lay–up to provide additional stability to the system. A uniform thickness of 0.089 in was achieved for this system using an autoclave. A uniform thickness of 0.0662 in was achieved for the quasi–isotropic system using an autoclave. The specimen was sprayed with flat black paint and the force on the specimen was recorded as the system was cyclically loaded. This change in force was later used in computational models. The same quarter geometry finite element mesh was used for the computational analysis of this system with material properties provided in Table 2.1

The computational results for two loading cases with the corresponding experimental loading cases are plotted in Figures 2.20 and 2.24 for the $[0_5/90/0_5]$ lay–up. These experiments take into account the thermomechanical constant provided in Figure 2.10, $k_\varepsilon = 3.8195x10^4$. The full–field infrared signal can be used to verify various specimen geometries and material systems with some accuracy. Notice the uniformity of the TSA signal in Figure 2.19. Overall, the results illustrate the accuracy of the proposed method in determining the full–field strain invariant in various FRP systems. In both cases only a coating of flat black paint was applied to the specimen surface. Improved results may be obtrained by adding a layer of continuous fiber mat material or epoxy to the surface. The 45 layer of S2–glass/epoxy on the surface of the Quasi Isotropic layup shows that the surface ply plays a large role in the thermoelastic response.

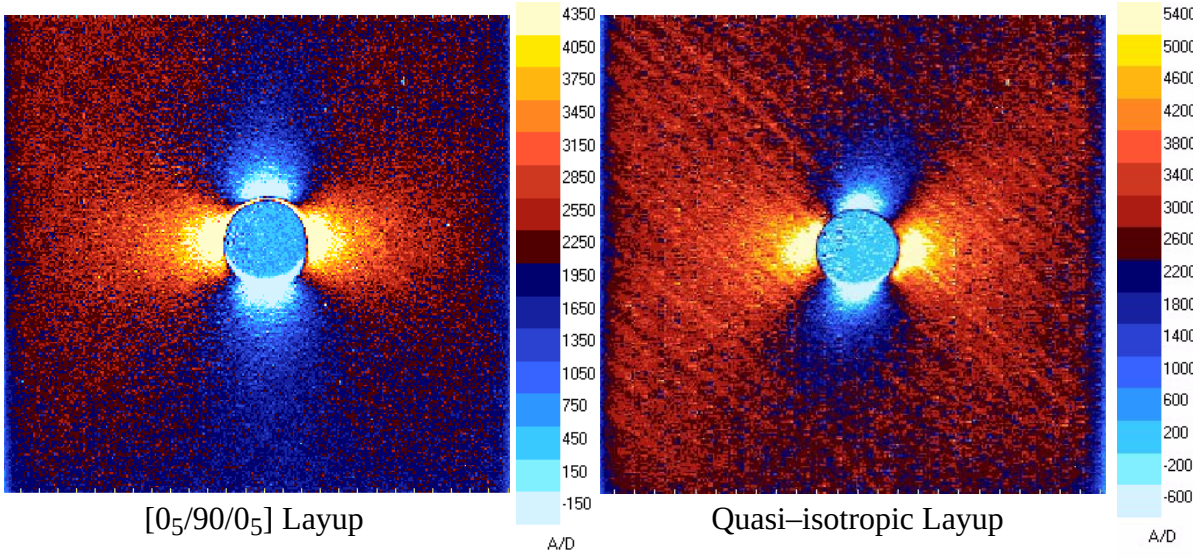

$[0_5/90/0_5]$ Layup Quasi–isotropic Layup

Figure 2.19. TSA images of S2–glass/epoxy

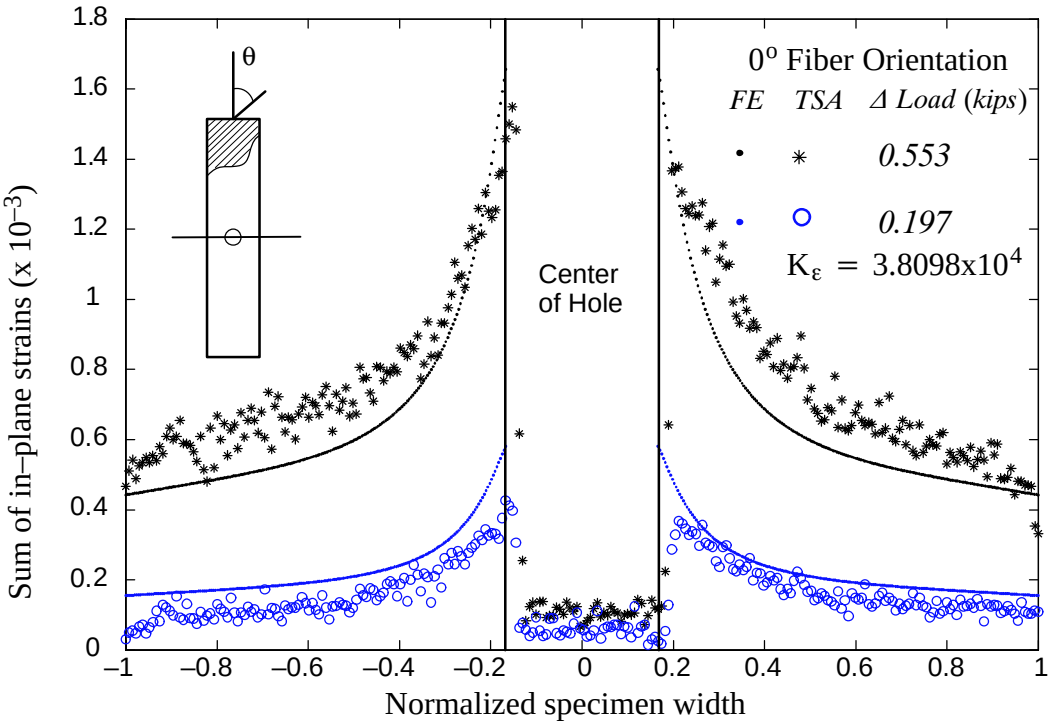

Figure 2.20. Horizontal line interrogation of open−hole geometry for verification of thermomechanical calibration of un−coated S2−glass/epoxy for the $[0_5/90/0_5]$ lay−up

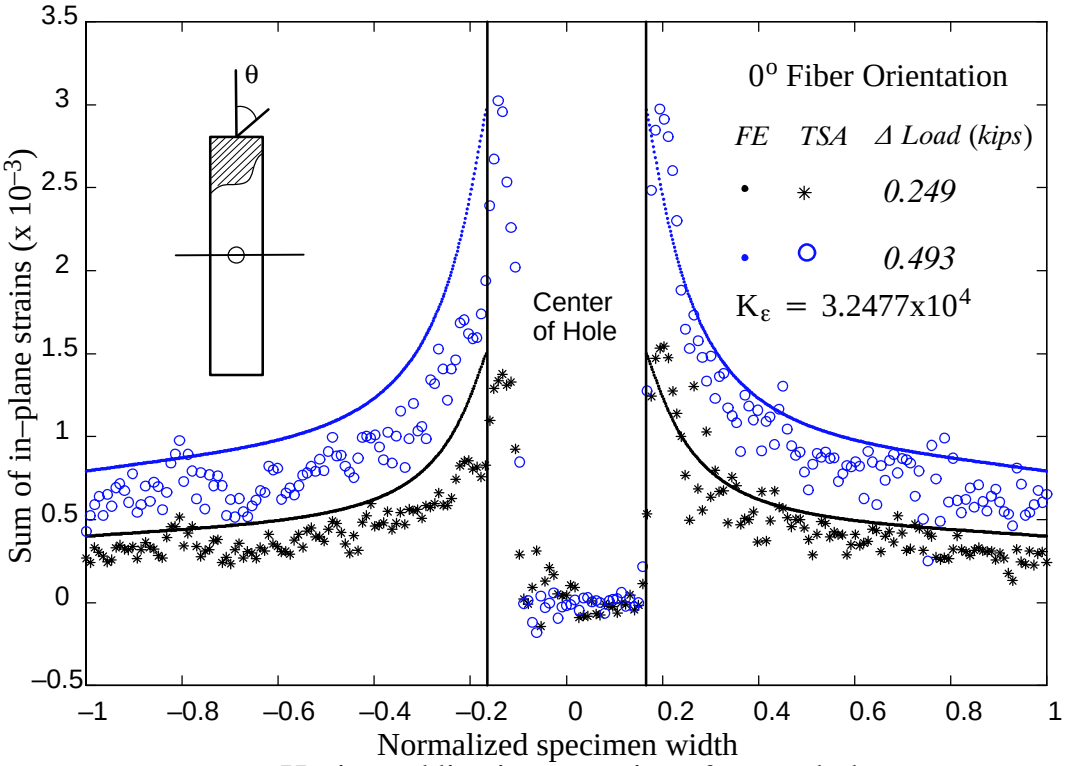

Figure 2.21. Horizontal line interrogation of open−hole geometry for verification of thermomechanical calibration of S2−glass/epoxy with epoxy coating for the $[0_5/90/0_5]$ lay−up

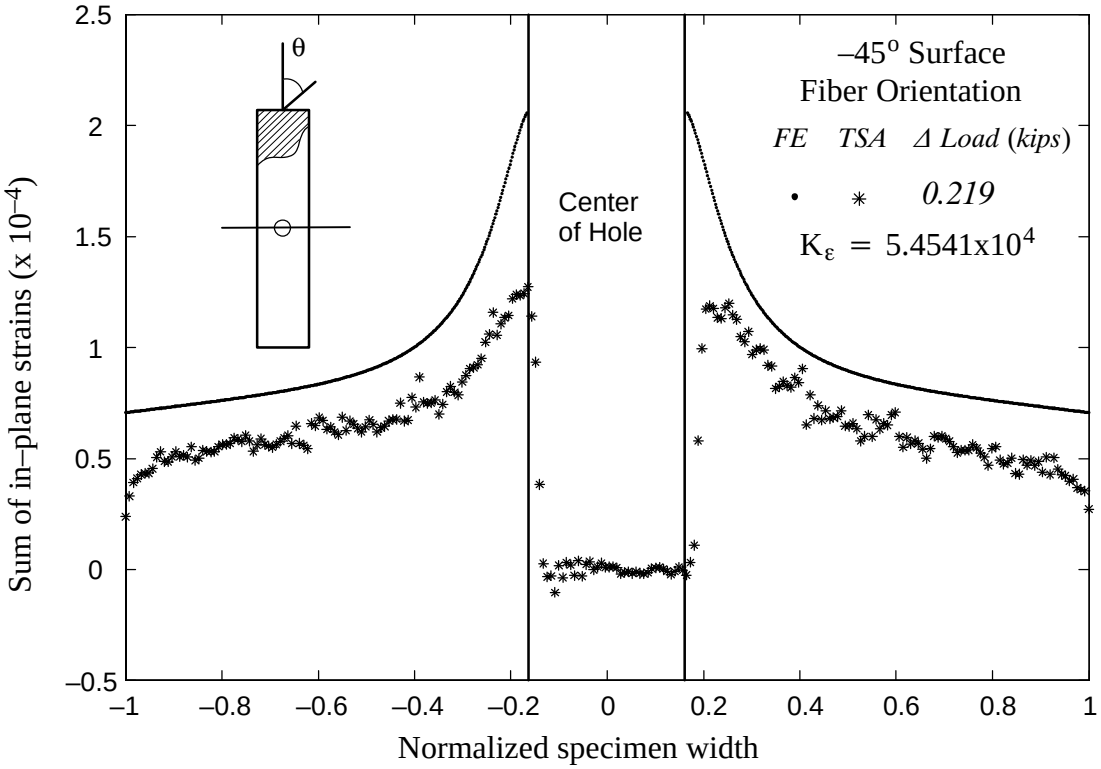

Figure 2.22. Horizontal line interrogation of open−hole geometry for verification of thermomechanical calibration of un−coated quasi−isotropic S2−glass/epoxy

This can be explained due the multi–axial state of stress in the material system of the top layer, i.e. normal and transverse stresses. Previous predictions from this type of calibration were done for the 0^o top layer with predominately axial stresses. This may also explain the good quality in those cases.

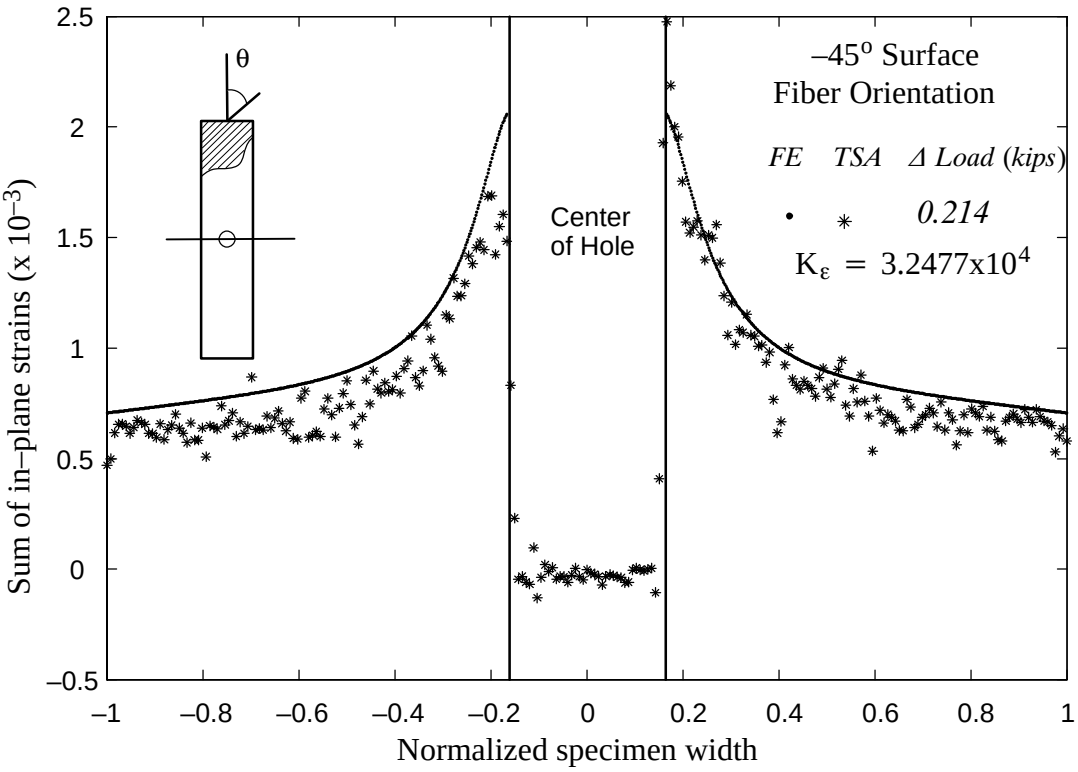

Figure 2.23. Horizontal line interrogation of open−hole geometry for verification of thermomechanical calibration of coated quasi−isotropic S2−glass/epoxy

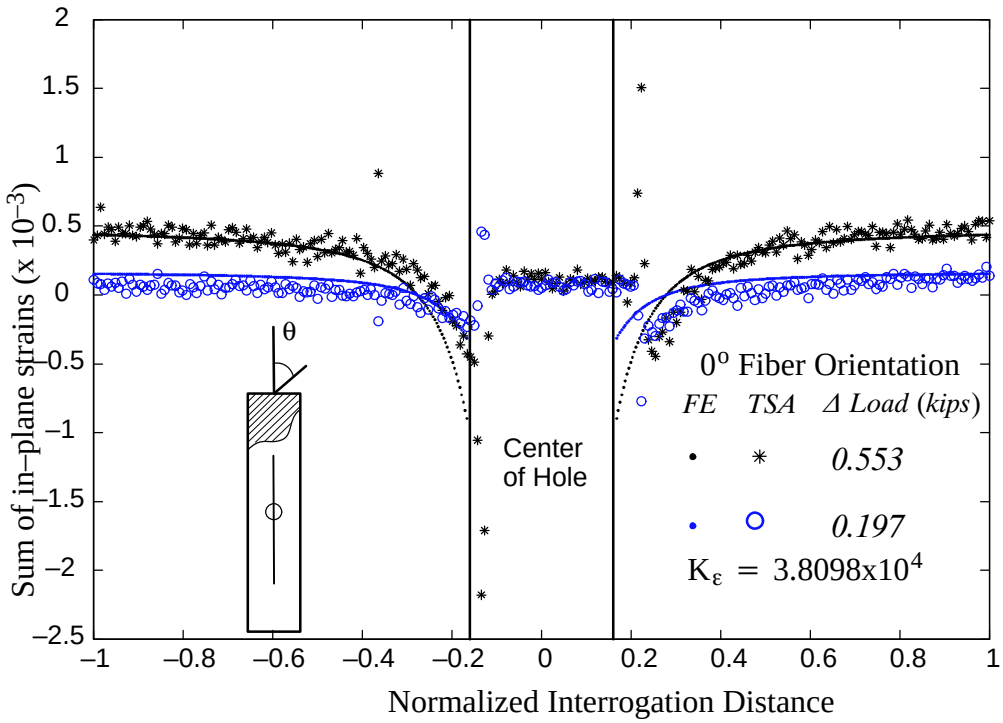

Figure 2.24. Vertical line interrogation of open−hole geometry for verification of thermomechanical calibration of un−coated S2−glass/epoxy for the [0_5/90/0_5] lay−up

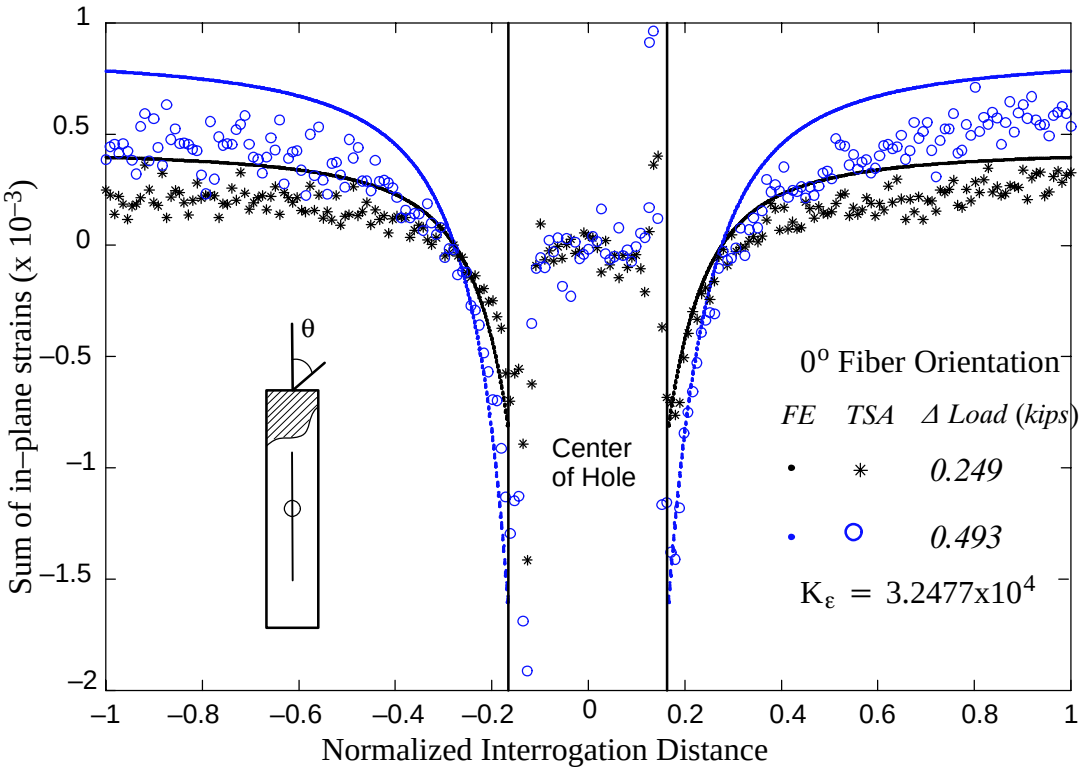

Figure 2.25. Vertical line interrogation of open−hole geometry for verification of thermomechanical calibration of coated S2−glass/epoxy for the $[0_5/90/0_5]$ lay−up

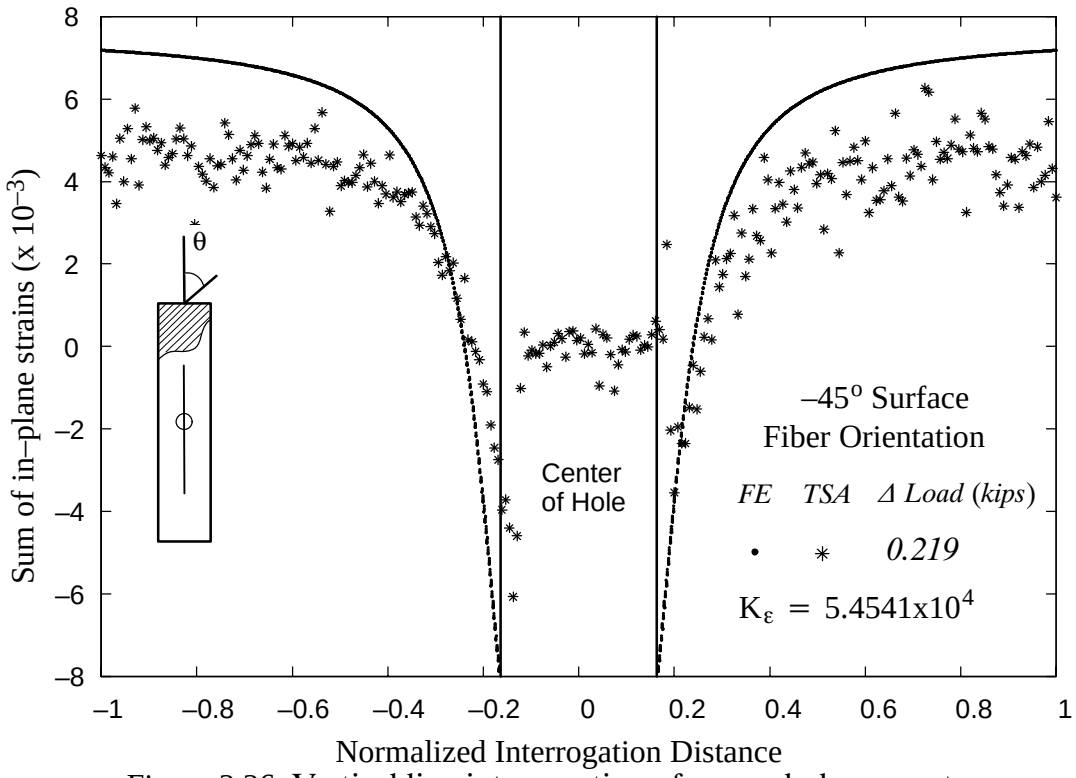

Figure 2.26. Vertical line interrogation of open−hole geometry for verification of thermomechanical calibration of un−coated quasi−isotropic S2−glass/epoxy

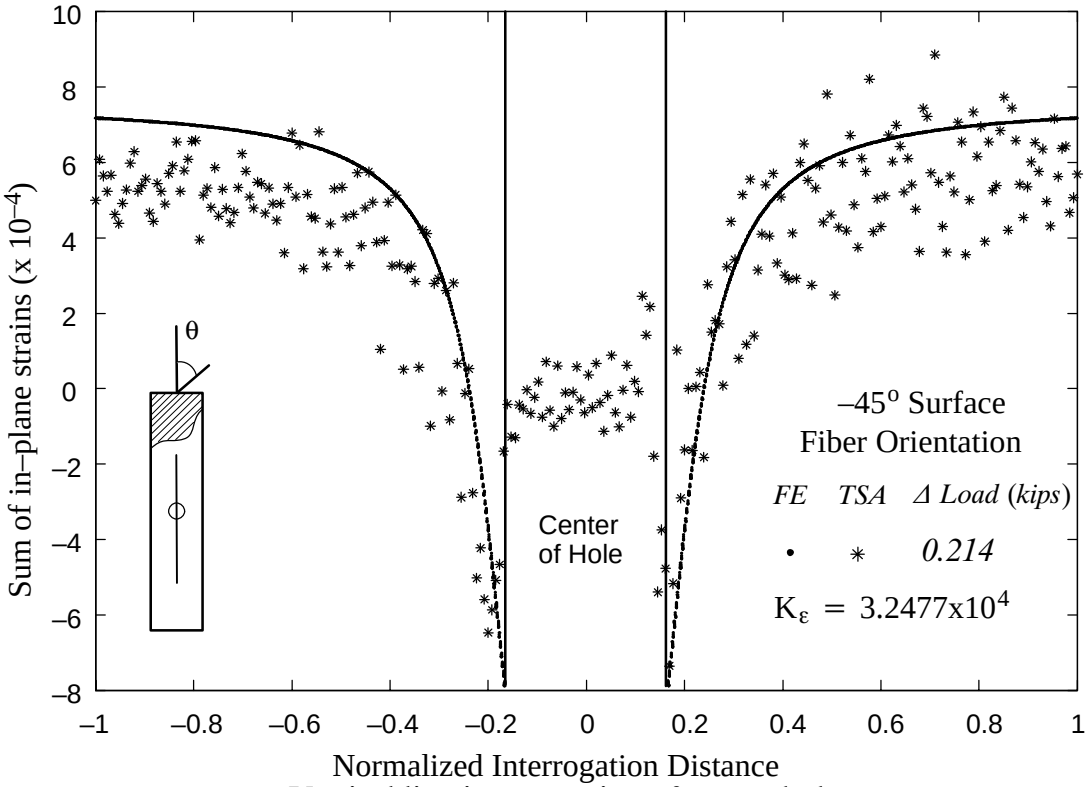

Figure 2.27. Vertical line interrogation of open–hole geometry for verification of thermomechanical calibration of coated quasi–isotropic S2–glass/epoxy

2.7 Conclusions

A experimental thermoelastic stress/strain analysis (TSA) technique developed by El–Hajjar and Haj–Ali (2003) was expanded on in this study to measure the sum of the normal surface strains in a variety of FRP composites including Carbon/epoxy, S2–glass/epoxy, and thick–section E–glass/polyester laminates. The new method relates the Thermoelastic signal to the sum of the normal surface strains in FRP composites, and it provides a full–field measurement of the strain invariant that can be used to verify computational models. The study in this section provides steps to acquire thermomechanical calibration constants and verification with results from finite element open–hole models. The new experimental technique provides excellent correlation with computational models. If an additional isotropic surface coat is not applied, two calibration constants may be needed to describe the system under a multiaxial state

of stress. Further testing is needed to provide insight into the effects of the thickness of the isotropic coating and alternative surface coatings in order to guarantee the required adiabatic conditions. In addition, experimental methods using two calibration constants to eliminate the need for coating can be the subject of further research.

CHAPTER 3

INFRARED THERMOGRAPHY FOR CORRUGATED BOARD DEFECT DETECTION

3.1. Objectives

The objective of this study is to apply a recently developed Infrared Thermography (IR–T) technique to investigate the quality and hidden damage of fiberboard materials and structural systems towards providing the industry with a new non–destructive tool that can be implemented in production environments. The proposed experimental setup employs a high–resolution and automated IR acquisition system able to detect temperature changes with a thermal resolution of 0.001 Kelvin within 1 minute or less. Fibrous material systems subjected to small vibration, cyclic loading, or thermal excitation are monitored with an IR camera which detects defects and damage that would otherwise be hidden. The ultimate objective of the experimental approach is to record the IR images of fiberboard systems with and without damage acquired during manufacturing and service. The technique provides a new non–destructive method of determining the quality of fiberboard systems that will be useful as a quality control tool in converting operations. For example, detection of debonded areas from insufficient or improper glue application in corrugated board may be possible with this technology.

One special quantitative technique of Infrared Thermography is referred to as thermoelastic stress analysis (TSA). This non–contact stress–analysis technique employs a sensitive IR camera to detect small changes of temperature from a stressed body. Under adiabatic and reversible conditions, the application of a small load will induce small and repeated variations in temperature that are proportional to the sum of principal stresses in an isotropic material. Defects in an otherwise uniform specimen result in stress concentrations which are manifested as localized non–uniform emissions of IR. A recent TSA method has been developed and applied for layered composite materials to measure the sum of the direct surface strains using

a top thin–coated in–plane isotropic layer. This technology will be developed and applied to corrugated board specimens to determine whether the proposed technique can detect manufacturing defects systems in corrugated combined board such as debonded medium, creases, or crushed medium. We have demonstrated the utility of the technique to detect defects such as wood shives, glue line defects, stress concentrations, and other damage effects in corrugated board. The method is shown to work for analyzing compression wood in structural wood products. Several test setups are designed for analyzing damage in corrugated board. These infrared thermography methods and setups are developed with the intention of providing industry with a tool that may be implemented with readily available equipment such as mechanical excitation sources typically present in manufacturing environments.

The sensitivity of the infrared thermography techniques presented in this report is found to be dependent on the investigated anomaly of interest. The report outlines how a particular defect can be detected and its IR image under loading can yield information on its thermo–mechanical material properties, such as how to process, examine and enhance the sensitivity of glue line defects and contrast those with uniform or undamaged medium in order to quantify differences with damaged products. Finite element (FE) analyses are performed for perfect material systems in order to guide the experimental post–processing seeking stress patterns that are not within the average spatial responses. Moreover, the FE modeling is used to examing and guide the test setups for different materials and geometries to enhance the thermo–mechanical response of the material and material defects.

Various setups replacing mechanical oscillation with pulsed or spatially sweeping IR beams have been investigated in this study as alternative methods for defect or damage detection. These alternative methods have provided mixed results, but may be preferred methods for exciting particular anomalies when either mechanical excitation sources are not reasonable or when a valuable qualitative inspection is all that is required.

Some tools are outlined which automate defect detection for quantitative analysis of fiberboard structures. The proposed quantitative analysis of infrared images has been implemented to better quantify quality in corrugated board. The method has been developed as a general tool and can be extended to various structural/material systems.

3.2. The Corrugated Board Structure and Manufacturing

Corrugated board has been the most widely used packaging material for more than 100 years for several reasons. Corrugated board is a composite material system that provides a high stiffness to weight ratio at a low cost. The material provides protection to the packaged goods due to excellent impact resistance and thermal insulation properties. Corrugated board comes from renewable resources and is completely biodegradable and recyclable. In addition, the corrugated structure provides printable faces for high marketability.

Before damage detection or explanations for problems present in corrugated board an overview of the manufacturing process for corrugated board will be presented. The process begins when the first facing, the single face liner, is glued to the medium. The medium consists of the flutes that separate the liners of the corrugated board. The corrugated medium is held in place on the corrugating rolls by vacuum, pressure, or mechanical fingers before adhesive is applied by an applicator roll. Both the corrugating medium and the linerboard are preheated before they are glued and pressed together at the pressure roll. A controlled nip pressure is applied to the single–face board. At this stage the single–face board is kept at a temporary holding facility used for a buffer because the double back corrugator operates independently. Glue is applied to the exposed flute tips of the single–face board, and a light pressure adds the double back face to the corrugated structure. Hot plates are then used to cure the adhesive. The structure is finally slitted, scored, and cut in the machine direction (MD) and the cross direction (CD). The final product is a blank that passes to a box–making operation. Figure 3.1 below provides a description of the corrugated box structure.

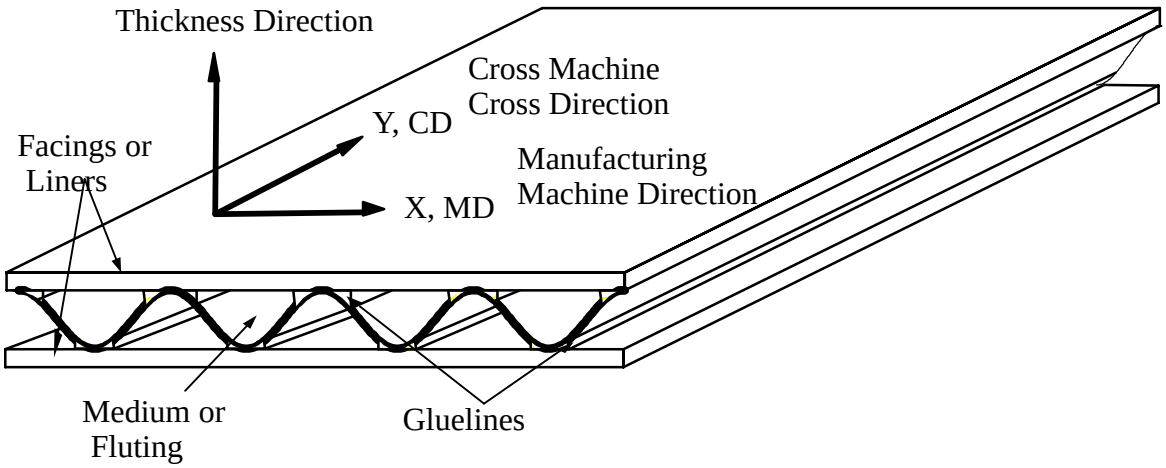

Figure 3.1 Description of corrugated board structure

Single Face

Double Face or Single Wall

Figure 3.2 Single face and double face corrugated material systems

Some important characteristics of the corrugated board structure include the anisotropic nature of the linerboard, and the strength and integrity of the medium. The papermaking process tends to align fibers in the machine direction. The linerboard is stiffer in the machine direction than the cross direction for this reason. The compressive and shear strength of the corrugated board depends on the strength and integrity of the glue lines that hold the fluted structure (medium) to the linerboard. The C–flute geometry is the corrugated board of interest in this study with approximately 130 flutes per meter and a flute height of 3.61 mm. The C–flute is desirable for its relatively good compromise between compressive strength, bending stiffness, and resistance to loads perpendicular to the liner.

3.3. Viewing with IR and Optical Filters

The selected infrared camera is designed with a wavelength sensitivity of the 3–5 microns range. The infrared part of the electromagnetic spectrum usually starts at about 1 micron in the near infrared and ends at 1 mm in the far infrared range. This camera, therefore, operates most effectively in the mid–IR range. Using different optical filters such as long pass or short pass filters was investigated to view the transmission of light through fibrous medium. In some cases, the camera operates outside of its sensitive wavelength range to produce "x–ray" type images. Optical filters can be used with infrared thermography with an understanding of the absorption properties of materials to obtain "x–ray" images of fibrous structures transforming an infrared camera into a powerful qualitative tool. Corrugated board gluelines (shown in Figure 3.1) can be qualitatively assessed without the need for destructive or chemical means such as iodine stains. Figure 3.3 (c) shows a "x–ray" image captured using thermography and selected optical filters.

Some difficulties arise, such as wavelength sensitivity and computational processing, with using infrared cameras for the study on the absorption of light through fibrous medium. Many infrared cameras have optical filters to increase wavelength sensitivity in a certain electromagnetic range. Also, differential thermography systems such as Delta Vision's DT1500 are setup with computational software for lock–in–thermography that processes the radiation over a user specified time interval. Differential thermography systems are designed to obtain temporal and spatial variations of thermal data. It is possible to turn this software processing off to view direct transmission of IR through fibrous medium. For this example, real–time images have been captured without computational processing.

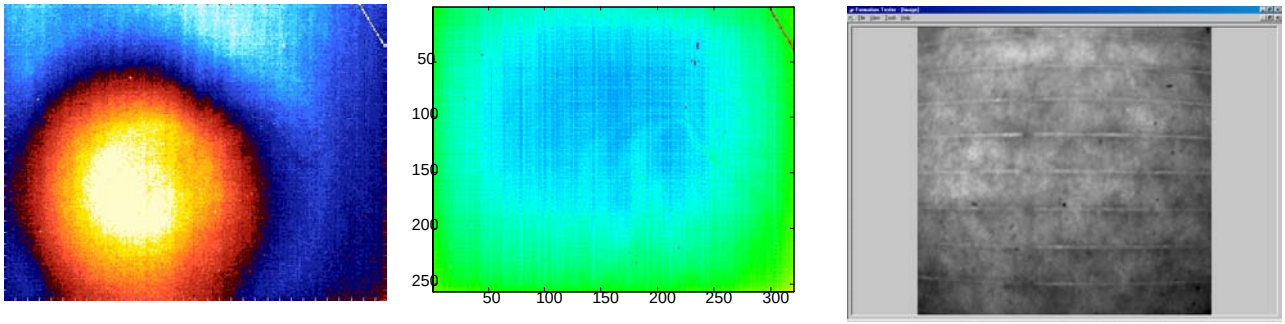

(a) Deltavision DC integration (b) Matlab DC integration (c) NIR transmission optical filters

Figure 3.3 NIR transmitted light image, single face side of commercial corrugated board facing the camera

Differential thermography systems are capable of producing differential (AC) and static (DC) thermal images. The DC images show absolute temperatures spatially, while AC images show thermal changes of thermal data spatially over time. The DC images in this case require some integration over time and require computational processing. The images can be processed with the software that is provided with the Deltavision camera or with software such as Matlab. Figure 3.3 (a) and (b) show a DC image processed with Deltavision and Matlab software respectively. Differential thermography may not be desirable method of viewing IR transmission because of the computational processing of thermal data.

The IR camera setup can also used to qualitatively assess and investigate the linerboard and gluelines in corrugated board. A voltage controller is used to change the intensity of light from an incandescent, 60 watt bulb. Long pass filters are used in conjunction with the camera to observe E–flute and C–flute corrugated structures. The gluelines can be observed with a 1 micron long pass filter at around 80 volts. The heat source behind the board was visible in the DC subtractions.

3.4. IR–TSA General Test Setups

Figure 3.4 shows a schematic representation of the two main non–destructive testing methods developed in this project. The sensitivity of the IR–technique is investigated with

different geometries of corrugated boards, and various excitation sources are examined as portable materials testing systems (PMTS). The technique equipped with PMTS can be applied for quality control of corrugated boards to improve the manufacturing process. The quality of corrugated boards can be monitored during the manufacturing process using the method developed in this research.

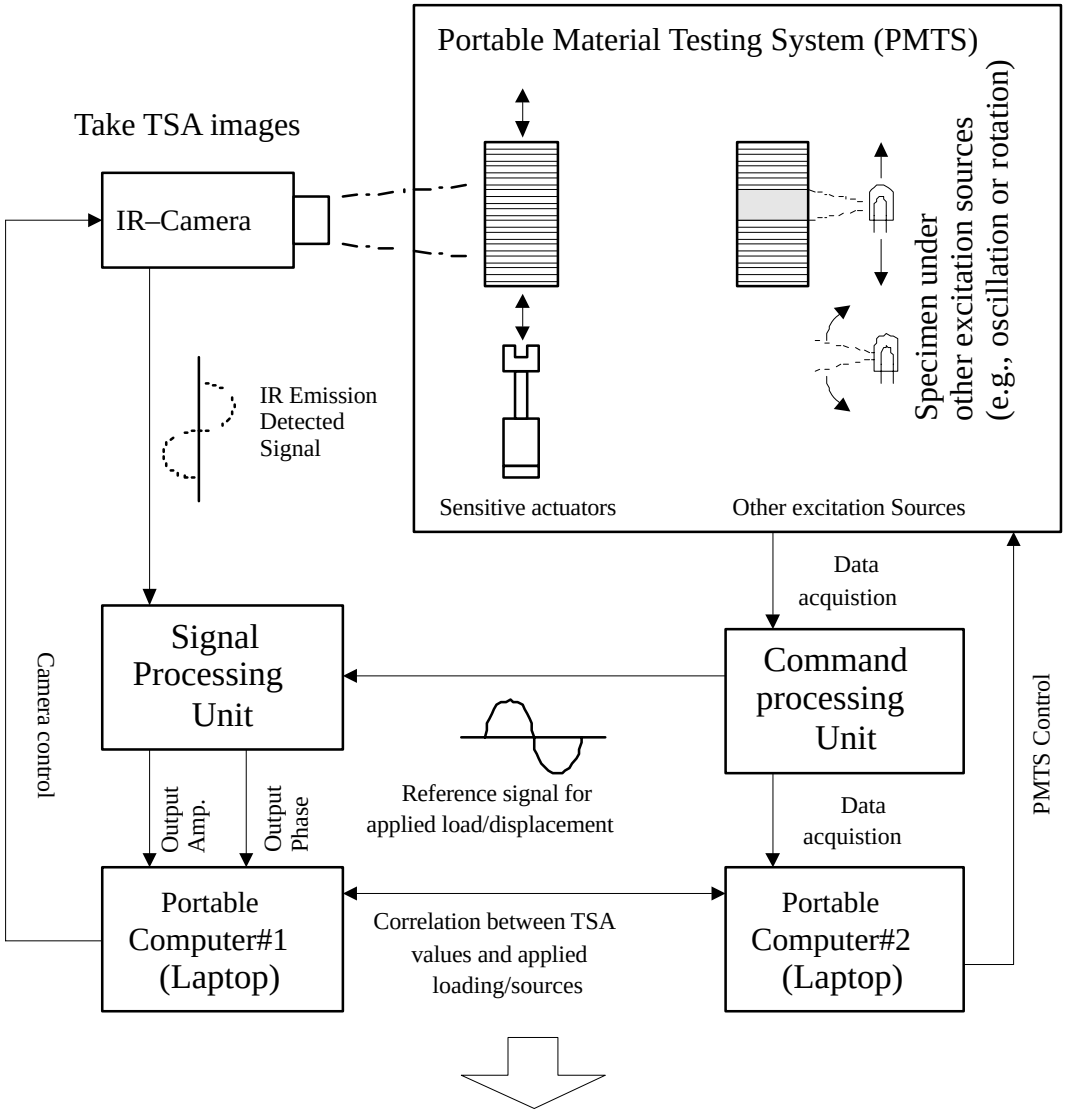

Figure 3.4 Schematic representation of the TSA−IR testing method as a non−destructive testing method developed in this project during/after manufacturing process

3.5. IR–TSA Tests with Fiberboard Systems and Corrugated Boxes

As an initial proof of concept, several box structures were tested with varying degrees of damage. These tests included IR–TSA of boxes in cyclic compression in a similar test setup to

the standard Box Compression Tests (BCT). Selected results presented in this section include IR–TSA from a pre–buckled corrugated box, from an undamaged box, from a box with debonded glueline at the box joint, and from a box with creaseline damage. This testing demonstrated the proposed combined IR and mechanical testing capability and motivated further investigations on corrugated board, and fiberboard components.

IR–TSA from Pre–buckled Corrugated Box

The intent is to see if under an extreme case of loading, stressed/unstressed areas are easily distinguishable. It is also interesting to view stress concentrations at box joints and at discontinuities due to damage. An IR–TSA image of pre–collapsed open top tray box measured under cyclic displacements showing the stress concentration at the corners and at the creased region is shown in Figure 3.5

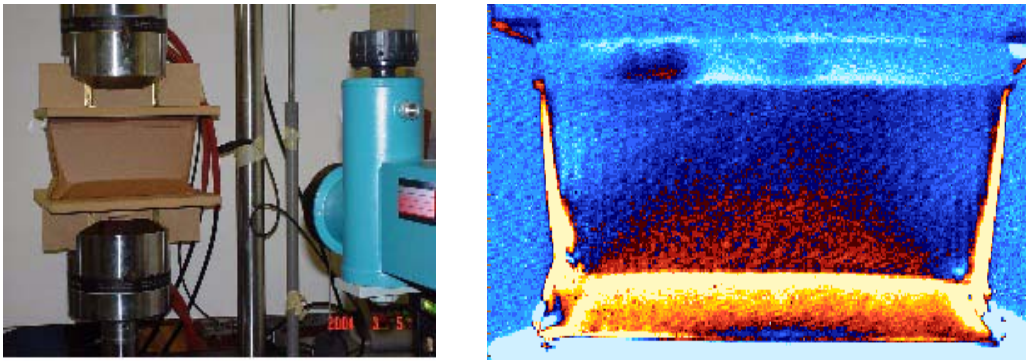

Figure 3.5 Infrared system examining the radiation emitted from a crushed corrugated box and the corresponding IR–TSA image

The IR–T setup is applied on a crushed corrugated box, which has collapsed due to prior testing at IPST. The goal is to use the IR–T method to detect the damaged creased area and examine the characteristics of the IR radiation emitted from the box when it is subject to repeated cyclic displacements. Unstressed regions show up as blue. The red area shows the excessive material stresses and concentrations, including creased areas due to buckling.

IR–TSA on an Undamaged Box for Comparison

Another test setup is conducted on an undamaged and recently manufactured box. Figure 3.6 shows the IR–TSA image of the box when subject to small cyclic loading in the form of axial displacements in the CD direction along the flutes. It is clear from the image that the box is not loaded uniformly due to spatial differences in the mechanical properties and due to edge effects at the corners and contact areas with the top and bottom plates. Geometry variations may lead to non–uniform load distributions and probide another reason for the lack of uniformity in the IR signal.

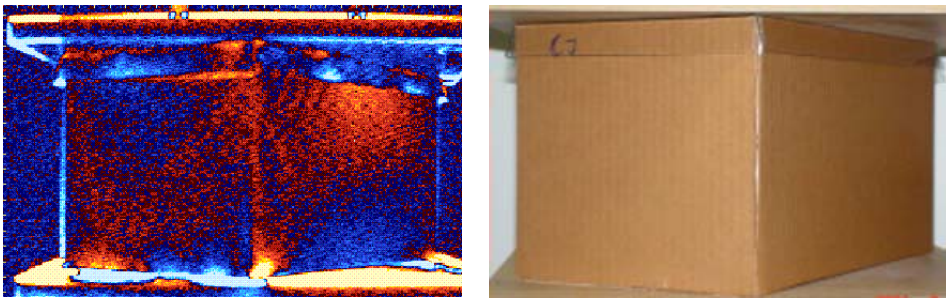

Figure 3.6 IR–TSA image of undamaged box under axial cyclic loading

IR–TSA with Debonded Glue Lines

In this example, the thermoplastic resin in the box edge (the manufacturer's joint glue lap) is cut to allow separation between the two adjacent sides. Figure 3.7 (b) shows the separated edge and the glue that is cut. Figure 3.7 (a) shows the IR–TSA image with a very different pattern at the damaged edge than that shown in Figure 3.6 Clearly, by subtracting these two images, one can detect this abnormality and associate it with the damaged edge.

(a) 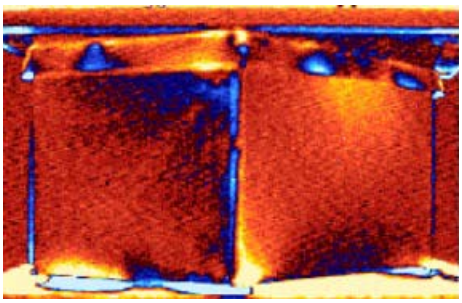 (b) 

Figure 3.7 IR–TSA of a box with debonded glue line (a) and the damaged box (b)

IR–TSA with Box with Crease Damage

The test approach was used to identify a crushed flute damage mode. Towards that goal, two flutes of a side panel of a box are crushed along the CD by pressing a smooth blunt plastic rod along the lengths of the flute tips. The box is tested with the IR–TSA setup and subjected to minimal cyclic compressive loads. Figure 3.8 illustrates the IR measurement at a closer distance relative to the other reported measurements. The two damage lines are clearly detected by the IR–TSA method. In addition, having the camera at a closer distance allowed a more sensitive measurement. Additional experiments are needed for specific box material and structural systems to quantify the IR signal dependence on frequency, amplitude and other parameters. This will optimize and tailor the proposed setup for a specific material and structural system. The measurement could detect the corrugated pattern of the box since the flute lines do not assume the stresses as much as the liner panels between the glue lines. Notice that the inter–flute buckling pattern of the liner facing is evident.

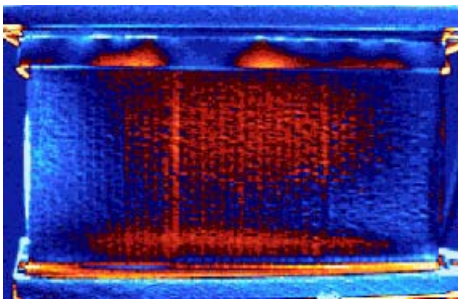

Figure 3.8 IR–TSA image of a box with induced two vertical crease lines

IR–TSA of Various Fiberboard Specimen Geometries

Several specimen geometries are investigated using IR–Technique such as the slotted board specimen shown in Figure 3.9 The IR–Technique may be used to qualify the quality of a board manufactured for a specific purpose such as box joints or handling areas in box products. The test is performed in tension–tension displacement control with consistent amplitude of 0.007 inches and a frequency of 3 Hz.

Tested Specimen Before Fracture Tesed Specimen After Fracture

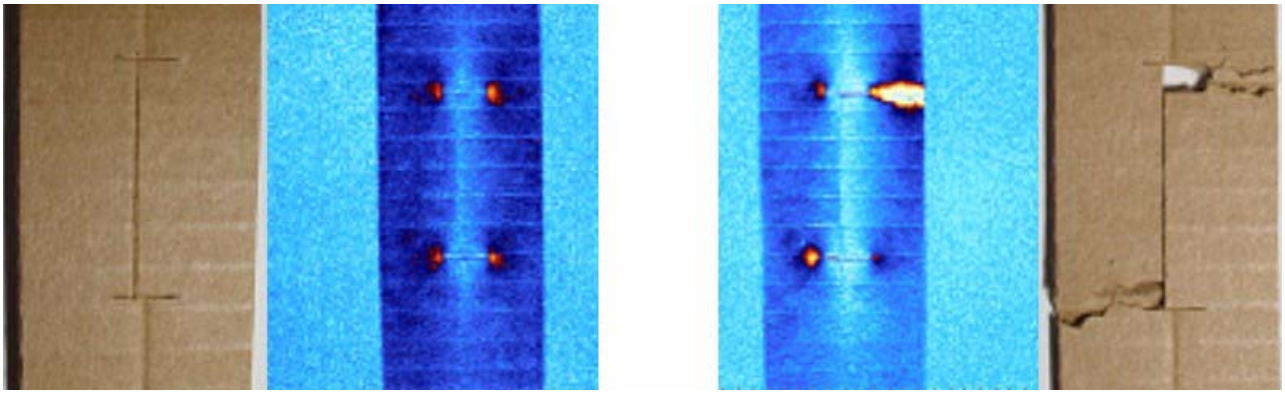

Figure 3.9 Progressive damage of fiberboards with manufacturing slitting and scoring damage

The TSA response of a slotted corrugated board is shown in Figure 3.10 This illustrates that the proposed method can be used to assess stress concentration and damage of a slotted board. The potential for quality inspection of fiberboard production is demonstrated in these tests.

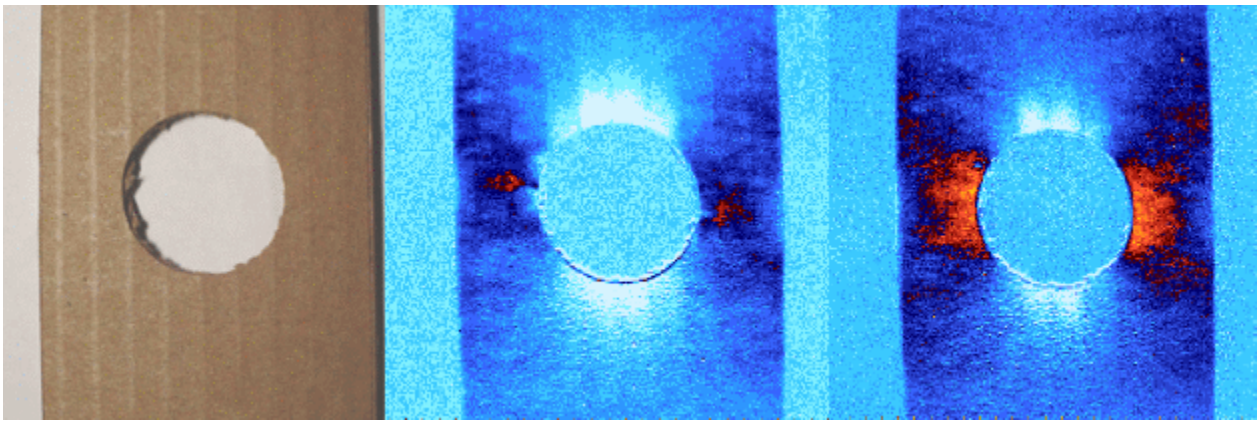

Sample with Cutout Compression Tension

Figure 3.10 Tension/compression IR–TSA tests of a notched coupon

The TSA responses of corrugated board under tensile and compressive cyclic loads and presents a potential for quality control in different fiberboard production processes. The specimen geometries and the loading type may be varied to better investigate flaws or anomalies. Stress concentrations and damage applied by the manufacturing of different specimen geometries can also be investigated using this method.

3.6. IR–TSA of a Fiberboard with Hidden Damage

Different new mechanical test set–ups and their parameters, such as geometry, grips, and loading, were investigated to optimize the measurement and minimize artifacts. For corrugated panels, stabilizing the samples and concentrating the stresses in the middle imaged section is achieved by using skewers through the flutings where the board is clamped in the grips of the MTS as shown in Figure 3.11 Experience later allowed a modification of the grip section replacing these skewers with steel pins.

To establish sensitivity of the method, board samples are cut in an “I” shape to concentrate the stress in the middles of the sample where a central 2.5 inch square area is imaged. Samples are 12 inches by 8 inched wide at the base and 2.5” wide at the middle ”neck.” Skewer rods are

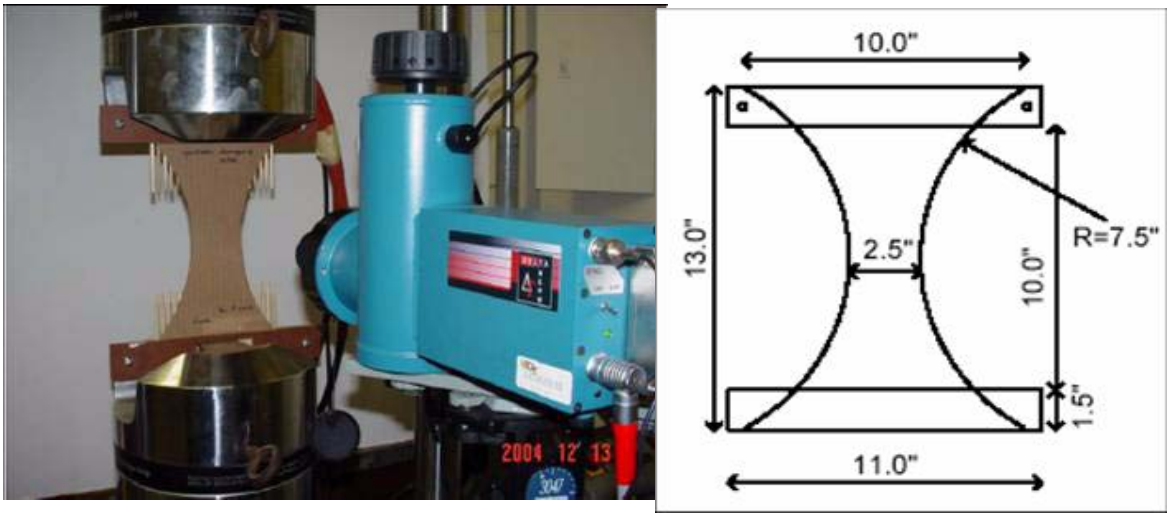

Figure 3.11 Photograph of the IR camera and specimen in−situ set−up

inserted into the flutes to allow support in a programmable MTS test frame without crushing the board. The MTS frame is set to oscillate with displacement control to have an initial displacement of 0.01 inches and a peak to peak amplitude oscillation of 0.014 inches at a frequency of 3 Hz.

IR−TSA of Creasing Damage Visible Through Single Back Liner

In the following example, a crease is made on the double back facing liner. This damage is shown in Figure 3.12 As the test progresses, the crease also becomes more prominent and so does the contrast in the resulting subtracted IR image. This shows that the proposed setup can detect hidden board creases inside of a box where the product has come into contact with the inside liner from rough handling. This is significant because it allows inspecting closed boxes while they are shipped or in service rather than as a quality product immediately after the boards have been manufactured.

Creased Double Back Liner, Back–View TSA image Single Back Liner Loaded in CD

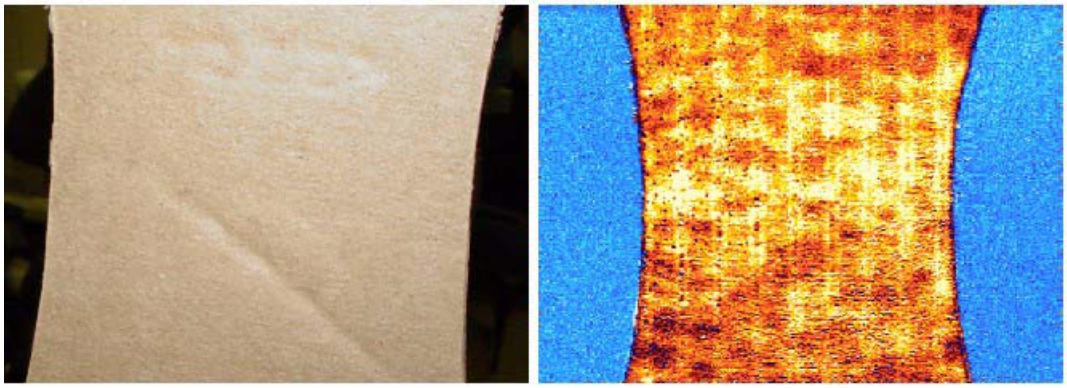

Creased Double Back Liner, Back–View TSA image Single Back Liner Loaded in CD

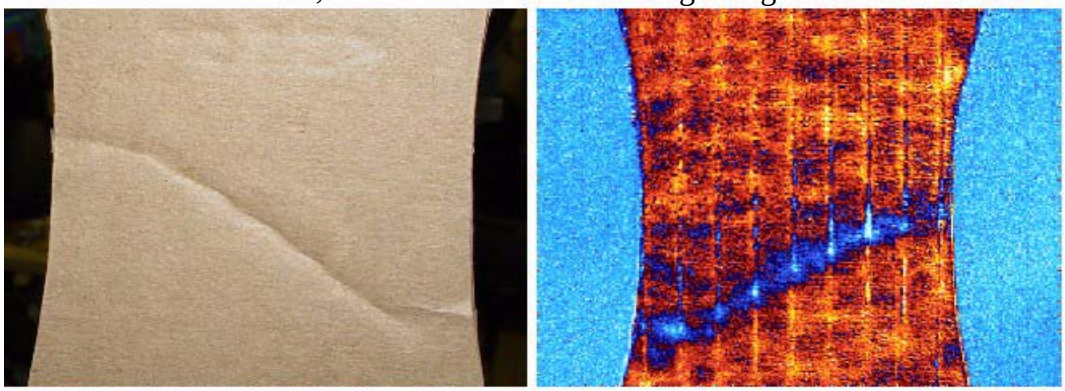

Figure 3.12 Detecting hidden crease line damage

IR–TSA of Flute Damage Visible Through Single Back Liner

In the next example, the flutes are punctured in the middle of the corrugated board specimen while the liners are left intact as shown in Figure 3.13 This method shows potential to detect unbonded areas which can occur in corrugating operations. Both, damaged and undamaged samples are subject to tensile loading with a mean displacement load of 0.007 inches.

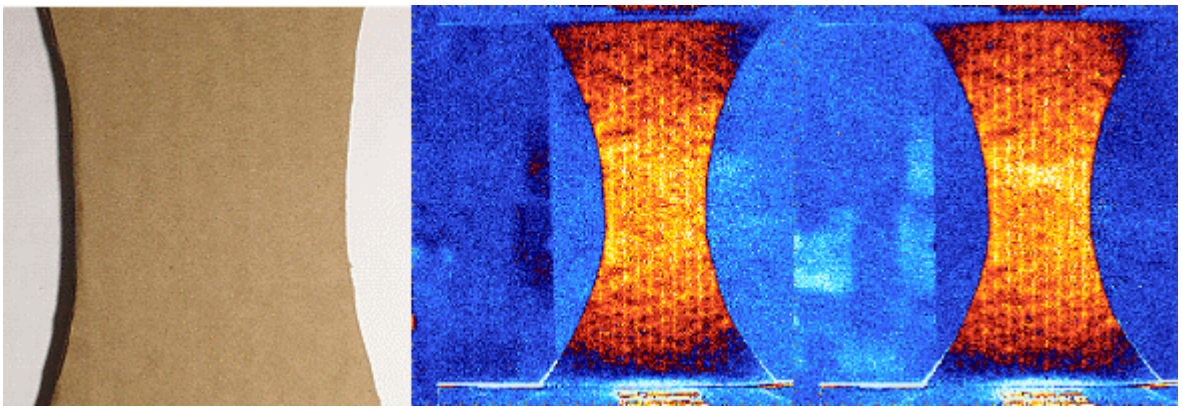

Damaged Coupon | Undamaged IR–TSA Measurement | Damaged IR–TSA Measurement

Figure 3.13 Hidden flute damage

IR–TSA for Detecting Board Cuts and Discontinuities

In the next example, the single back liner is cut while the double back liner and medium are left intact. Figure 3.14 shows the potential of the method to detect various damage effects such as board cuts and discontinuities that can occur in corrugating operations.

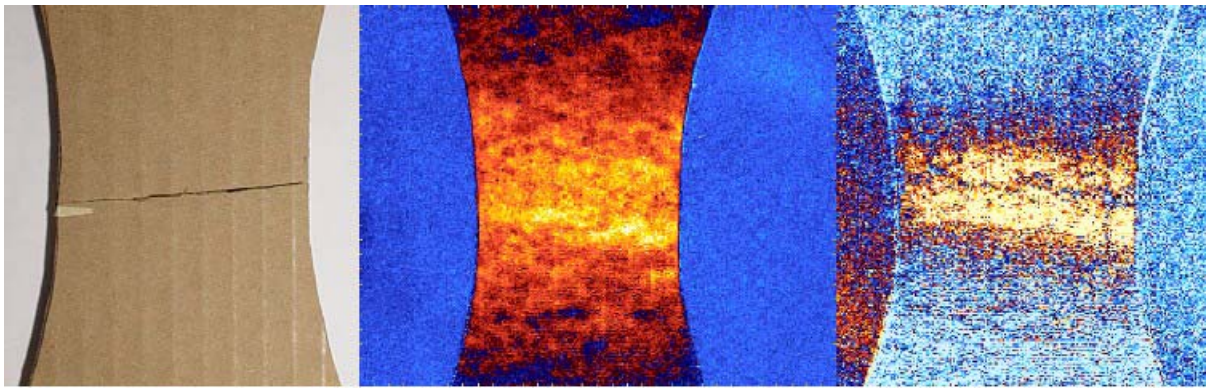

Back View Damaged Coupon | Front View | Front–View (IR) – Differential

Figure 3.14 Detecting board cuts and discontinuities

IR–TSA for Edge Compression Tests

Compression testing of corrugated board such as edge compression tests is also investigated. Compression tests of this specimen geometry may buckle the specimen with small

displacements, but this example shows that mechanical effects can be described qualitatively for tension or compression testing as shown in Figure 3.15

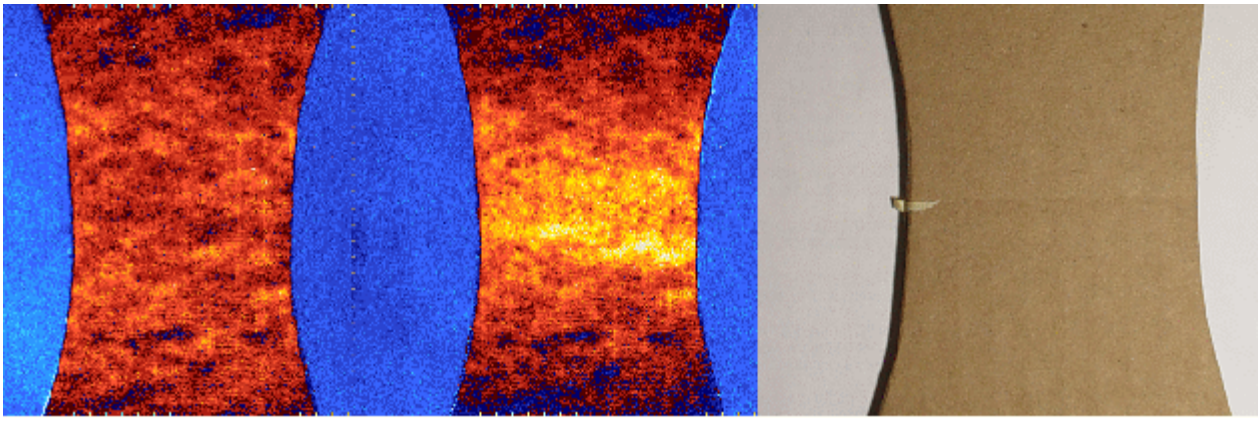

Undamaged IR–TSA Damaged IR–TSA Damaged Coupon Visible Crease Line

Figure 3.15 IR–TSA for ECT–compression test

IR–TSA for testing in the Machine Direction (MD)

This example shows the TSA response of a damaged transverse specimen and illustrates that the proposed method can be used to assess the effective bond in the glue–lines and thus can have a potential for quality inspection of fiberboard production.

Undamaged Damaged

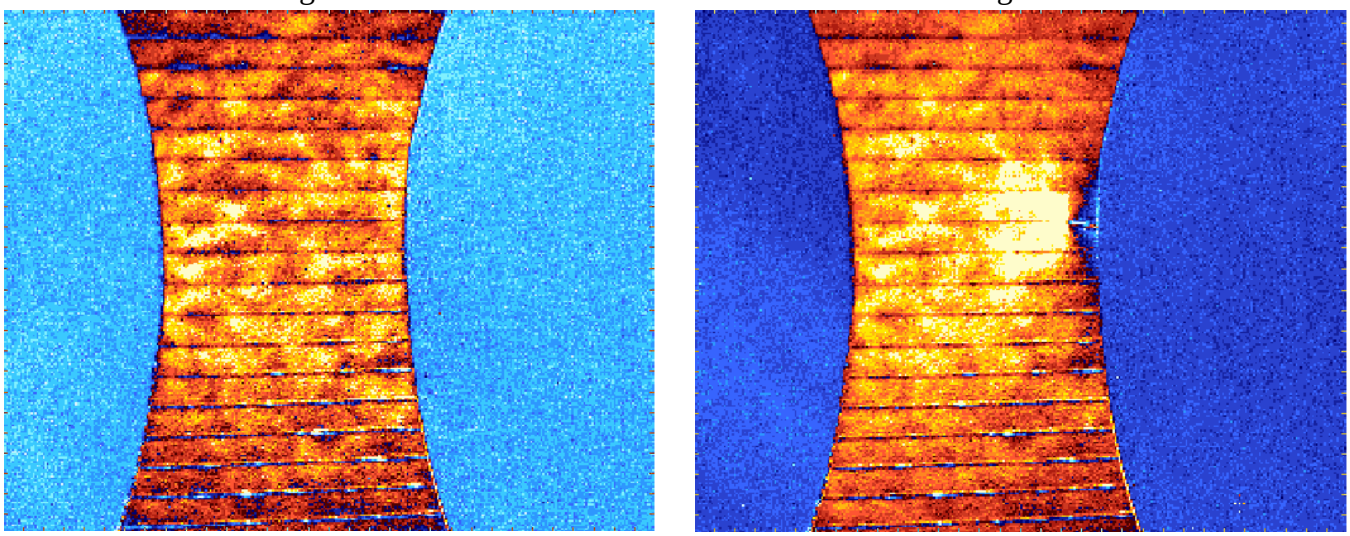

Figure 3.16 Undamaged/damaged response in the MD direction

3.7. Crushing Damage and Observed Anomalies

Crushed damage is applied to the front side of different specimen by rolling the specimen through a specified gap width. The specimens are investigated by looking at both the back side and the front side with an IR–camera to see the IR–TSA sensitivity. This test is performed under tension–tension displacement control with a frequency of 3 Hz. To show the effect that the amplitude of displacement has on the IR–TSA, the amplitude will be increased during the test. The shaded areas in Figure 3.17 indicate the imposed crushed area.

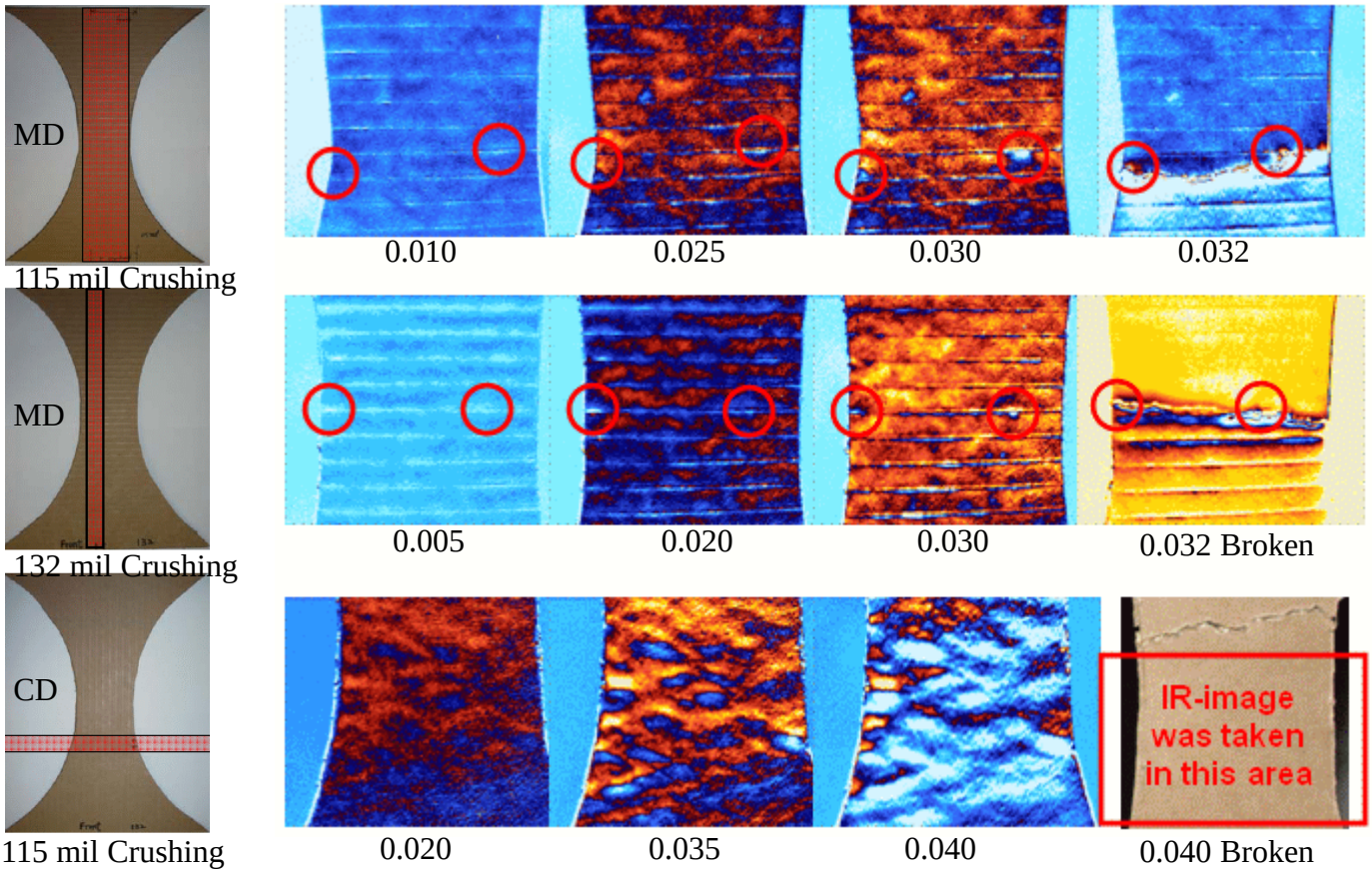

Figure 3.18 IR–TSA for different crushing damage levels

As a result of this test we have found that the sensitivity of the IR–Camera to detect crushing damage alone using this particular procedure may not be the best however mainly because the added damage modes that are accompanied with this type of imposed damage (stress

concentrations at the edges, glue line interactions and other inhomogeneities). However, this may be a preferred procedure for detecting tearing damage propagation of the corrugated paper as shown in the progressive damage measurements above. In addition, flaws or anomalies that may occur during manufacturing of the material and specimen are detected. This method shows promise for detecting some manufacturing flaws, but the sensitivity to different types of damage must be further investigated and tailored to specific fibrous materials, board, box systems.

Conclusions:

- Initial damage and progression are more visible in the MD coupons than CD's; Crushing levels of 115 and 132 (MD coupons) show similar amount of damage. Also, their ultimate failure is similar (0.032in amplitude).
- Damage can be detected qualitatively and with limited quantitative measures are also demonstrated for select damage systems and geometries
- Additional testing is needed in order to fully quantify the sensitivity of the proposed test and tailor it to specific fibrous materials, board, and box systems
- The current testing procedure can be used for detecting damage propagation tearing in paper and corrugated fiberboards.
- Initial manufacturing flaws or anomalies are qualitatively detected

3.8. Detecting Manufactured Anomalies in Fibrous Materials

Runnability of paper and paperboard is strongly affected by the appearance of defects in the material. Holes and spots may also act as crack–like defects. Wood shives and edge folds may introduce sharp defects on passage of roll nips. When designing a structure against fracture, three critical factors must be considered, i.e. the loading situation, the flaw size and the fracture toughness, which expresses the capability of the material to sustain stress concentrations without propagating a crack. Measuring fracture resistance as an overall average may not provide the most accurate characterization of the fracture toughness of fiberboard structures since toughness can be a function of the crack size. Methods capable of detecting and analyzing stress concentrations from inclusions, such as shives or other defects may provide a more accurate description of the material property. The proposed IR–TSA analytical–experimental approach

provides an additional method that can take this stress concentration into account when measuring the fracture properties of paper. Wood shives are one example of a defect that can be detected with the TSA coupled with FE analysis, and the induced stress concentration can be taken into account in characterizing the paper material properties. Figures 3.19, 3.20, and 3.21 illustrate the proposed approach for paper and wood products, respectively.

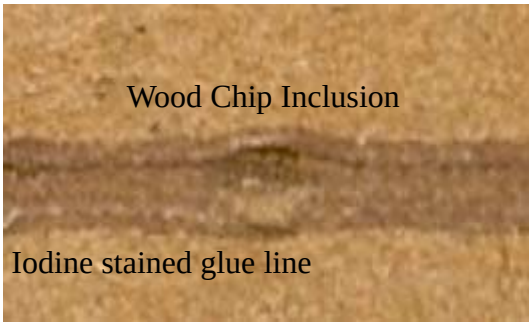

(a) Inside face of single back liner showing glue line

(b) Outside face of single back liner

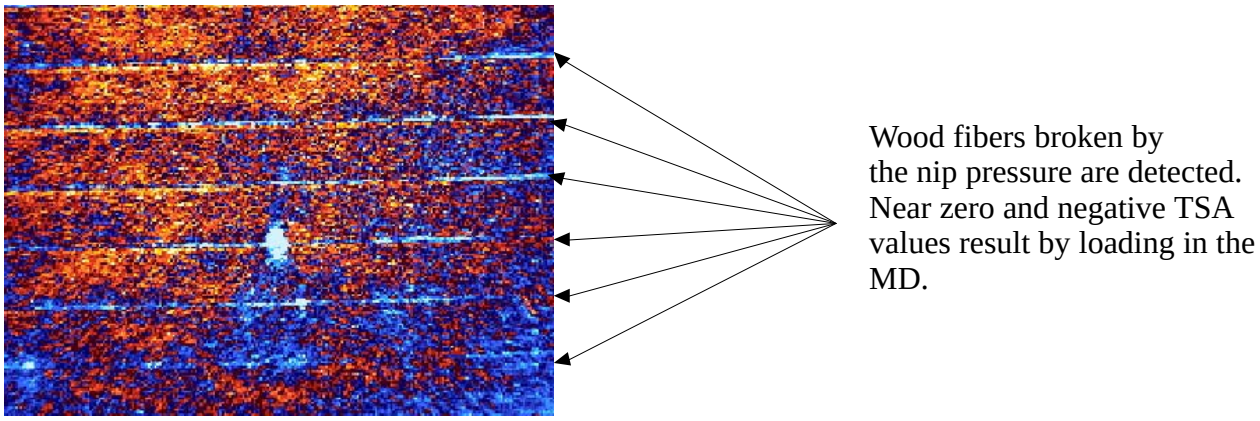

(c) TSA image of corrugated board with wood chip inclusion

Figure 3.19 IR–TSA for investigation and detection of wood chip inclusions

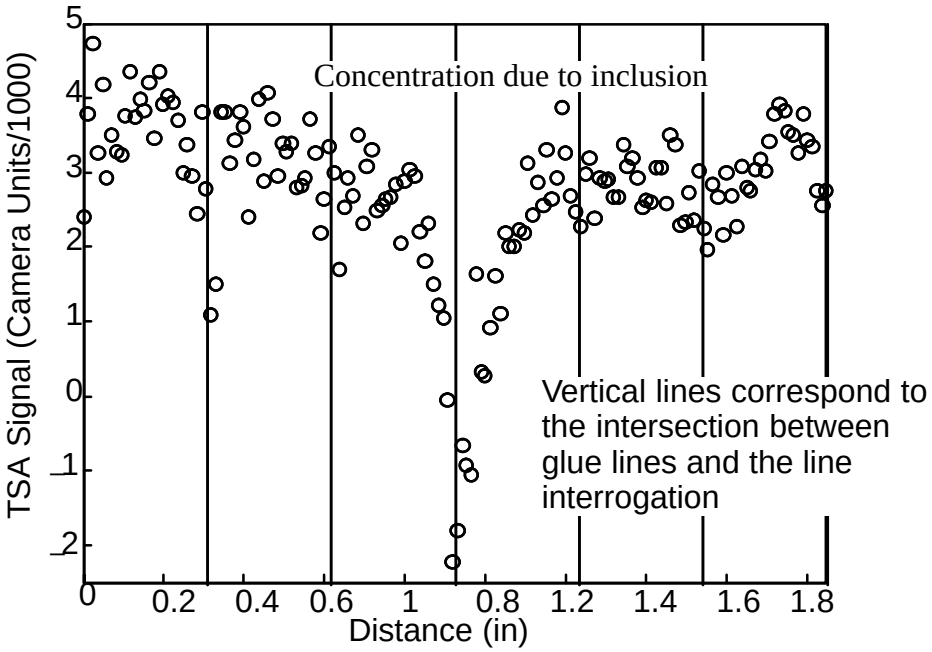

Figure 3.20 IR–TSA line interrogation though wood chip inclusion

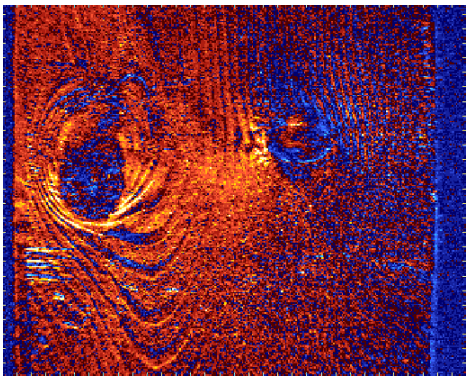

(a) IR–TSA image of 2” x 4”

(b) Photo of Corresponding 2” x 4”

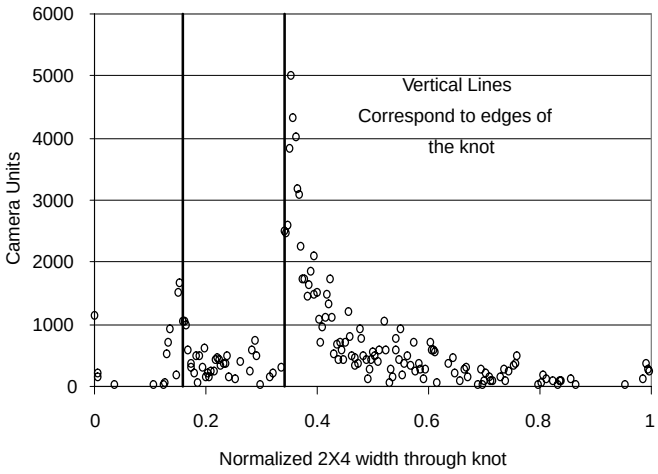

(c) Stress concentrations around wood knot

Figure 3.21 IR–TSA for investigation and detection of anomalies in structural wood products

3.9. IR–TSA Investigation of Glue–Line Bonding in Corrugated Structures

In this section, the proposed IR–TSA method is used to investigate the effect/quality of the glue on the health of the fiberboard structure utilizing infrared thermography. One important goal is to find an optimum method of exciting the glue lines by mechanical loading to increase the contrast for infrared thermography and allow interrogating the glue line mechanical property while under loading. We begin with a discussion of the structure of the corrugated board.

The corrugating medium is commonly attached to the facings using a starch adhesive due to its low cost. This adhesive is pressed between the corrugated medium and the single back liner with a nip pressure that is not present in the process of attaching the double back liner. The glue line on the single back side is therefore thinner and wider while the glue line on the double back side is thicker and narrower. The starch can be stained by spraying the inner side of the liner with Potassium Iodide.

The effect of the adhesive on the liner can be shown in a non–destructive test using Thermoelastic Stress Analysis (TSA). Figure 3.22 shows a schematic of the process to test the bond quality in corrugated structures. The IR–TSA produces crisp images due to a filtering process that correlates the material response recorded by the infrared with the peaks of the cyclic loading excitation source. The proposed method can expose the glue lines as they engage in the loading resistance (effective response) measuring the quality of the manufactured corrugated systems. The double back side shows more uniform patterns of stresses when compared to the single back side due to the low stress concentration in the glue–line areas. This is due to the relatively thick material of the glue–lines in the double–back. This is confirmed from both FEA and IR–TSA results provided in this section. The TSA is a preferred method for detecting bond quality. Iodine stains may show starch geometry on the liner, but the starch picture (geometry) alone will not indicate the quality of the “mechanical” bond with the liner. This is a major drawback of conducting iodine stains. The proposed IR–TSA method can be linked to quantitative quality control. It shows a good potential to describe the spatial coupling between the liner and flutes at various stress states providing a more coherent quantitative and qualitative bond quality assessment methodology.

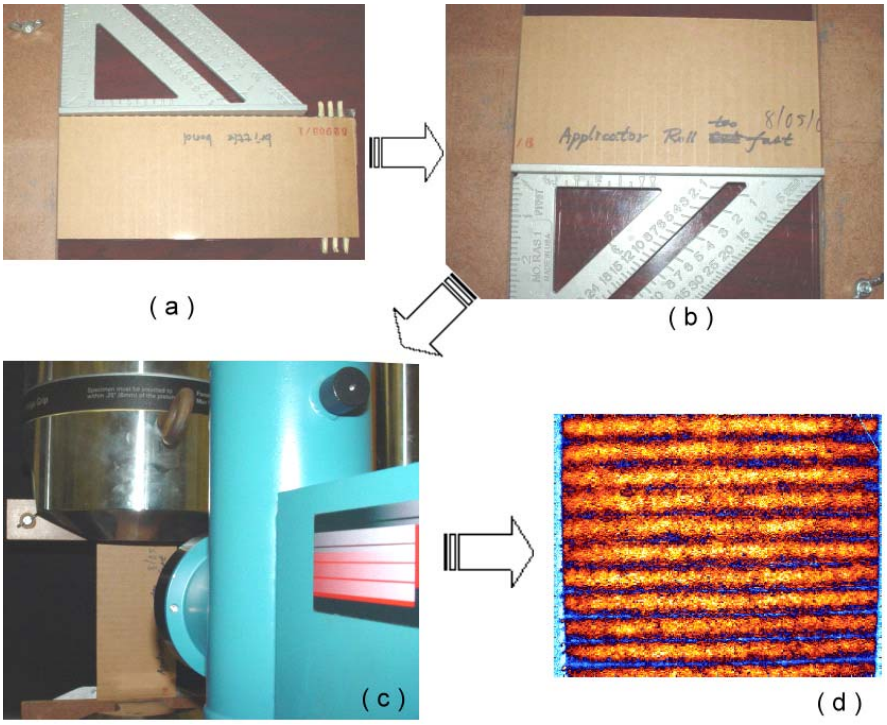

Figure 3.22 Designing a test setup for uniform corrugated coupons

The specimen in Figure 3.23 corresponds to a 4” by 10” specimen cyclicly loaded in tension–tension mode in the MD direction. The blue lines in this picture correspond to the glue lines in the single back liner of a corrugated board specimen. The yellow to red areas correspond to the liner between the glue lines. TSA images of the single back show orderly glue line patterns. TSA images of the double back single back show stress concentrations that are more spread out and not as ordered as the single back side. This effect may be due to the manufacturing process because the adhesive is pressed between the corrugated medium and the single back liner with a nip pressure that is not present in the process or attaching the double back liner.

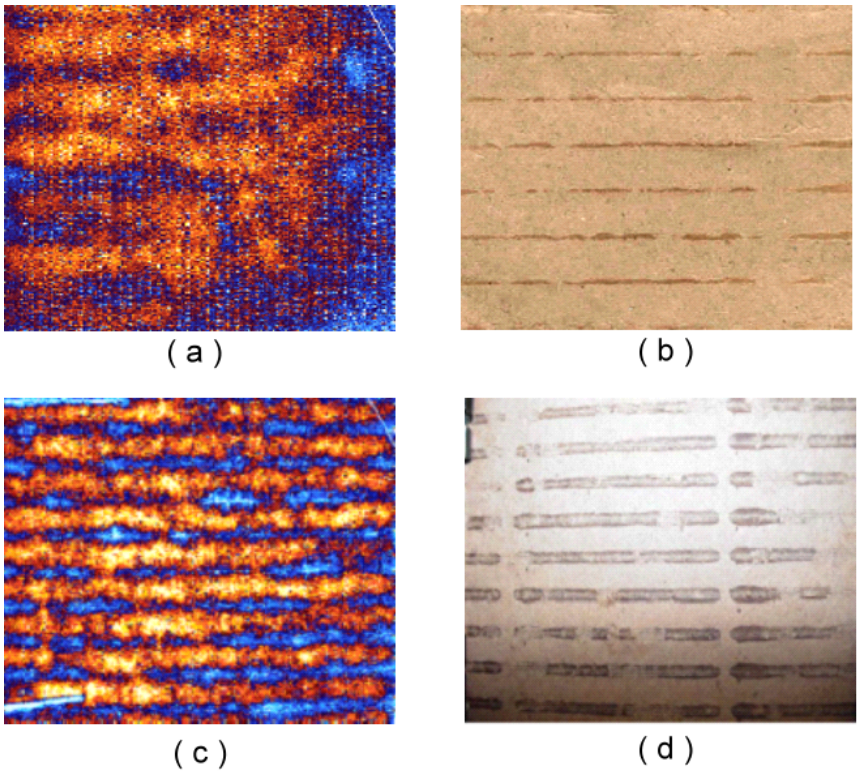

Figure 3.23 Infrared investigation of glue lines on the single back and double back liners (a) TSA image of double back liner, (b) Potassium Iodide stains of a double back liner, (c) TSA image of single back liner, (d) Potassium Iodide stains of the single back liner.

Several common bonding defects may be identified and detected using the IR–TSA method. Here we discuss the TSA signatures resulting from several common types of glue defects: brittle bond, white glue lines, excessive glue application, applicator roll gap excessive, clean–out finger too far out, applicator roll too fast, and applicator roll too slow.

Bond quality in industry is typically inspected by the use of iodine staining of the starch adhesive that connects the liners to the medium. This process involves carefully separating the liners from the medium, spraying potassium iodine on the liners, and investigating the patterns to qualitatively deduct bond quality or manufacturing problems. Figure 3.24 shows a schematic of the process used in this study to obtain iodine stains that correlate to Thermoelastic Stress Analysis images.

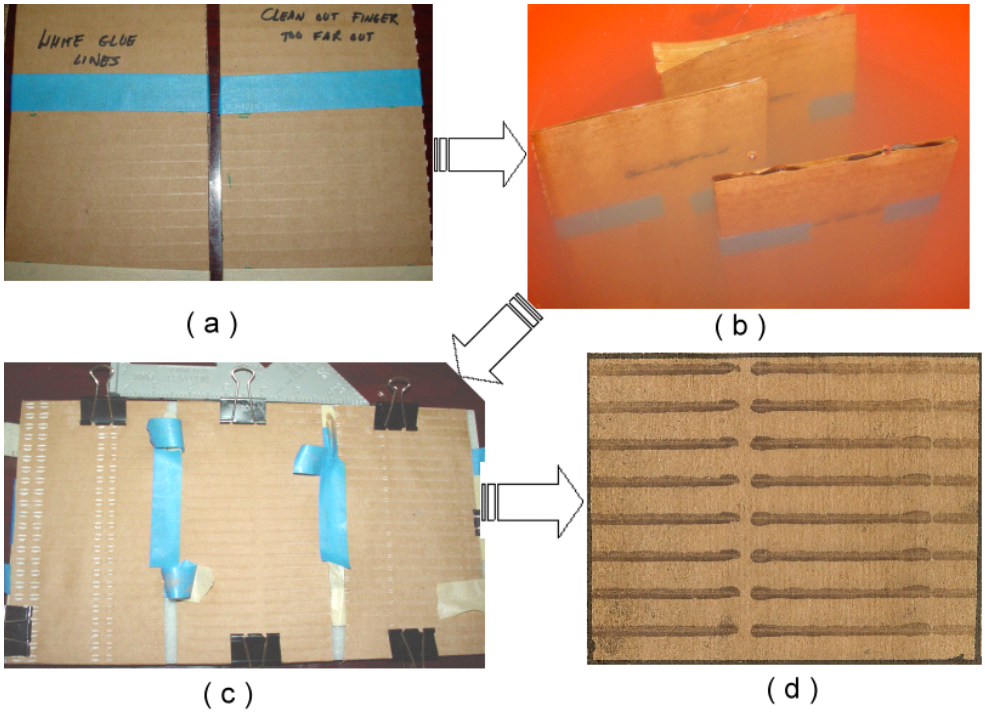

Figure 3.24 Coupling iodine stains with TSA for bond assessment: (a) Mark the imaged area (masking tape). (b) Soak the corrugated board. (c) Dry the corrugated board and pin down to prevent shrinkage. (d) Spray the board with potassium iodide and let dry.

Defects include brittle bond, white glue lines, and excessive glue application. Here we discuss the common types of glue defects: brittle bond, white glue lines, excessive glue application, applicator roll gap excessive, clean–out finger too far out, applicator roll too fast, and applicator roll too slow. A brittle bond may be caused by operating the corrugator at excessive temperatures for the paper. Temperatures are in excess of 220° F which may cause the bond to be brittle. While excessive heat may cause brittle bonds, insufficient heat may not fully gelatinize the startch adhesive resulting in poor bonding and white glue lines. Paper may run too quickly through the corrugator for example, resulting in insufficient paper preheating. Excessive adhesive application may be caused by the metering roll or doctor blade gap being too great. This may cause white glue lines and low pin adhesion strength.

Figure 3.25 shows the IR–TSA response due to white glue lines. Insufficient heat may not fully gelatinize the starch adhesive resulting in poor bonding and white glue lines. The paper may run too quickly through the corrugator, resulting in insufficient paper preheating.

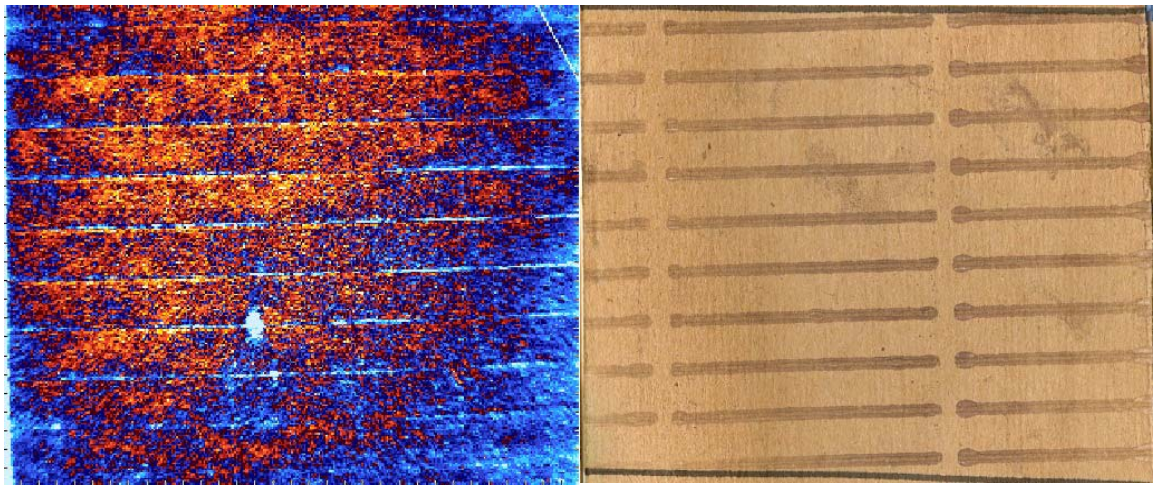

Figure 3.25 White glue lines

Figure 3.26 shows the IR–TSA response due to a brittle bond. A brittle bond may be caused by operating the corrugator at excessive temperatures for the paper. Temperatures in excess of 200º F may cause the bond to be brittle.

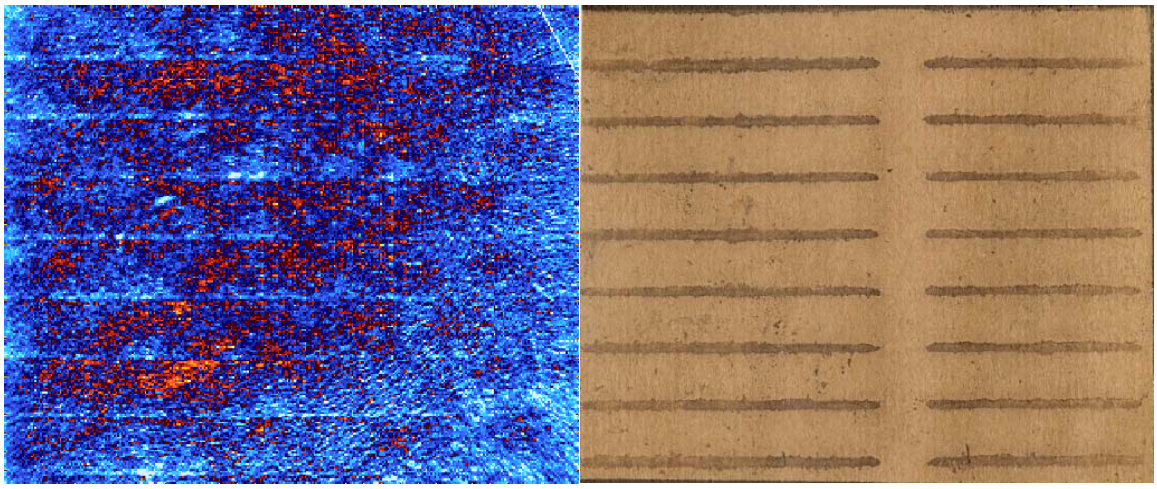

Figure 3.26 Brittle bond

Figure 3.27 shows the IR–TSA response due to non–uniform glue lines. Glue bonding defects in the form of low, uneven, or spotty adhesive application may be a result of the glue applicator roll when it is set too far from the corrugator roll

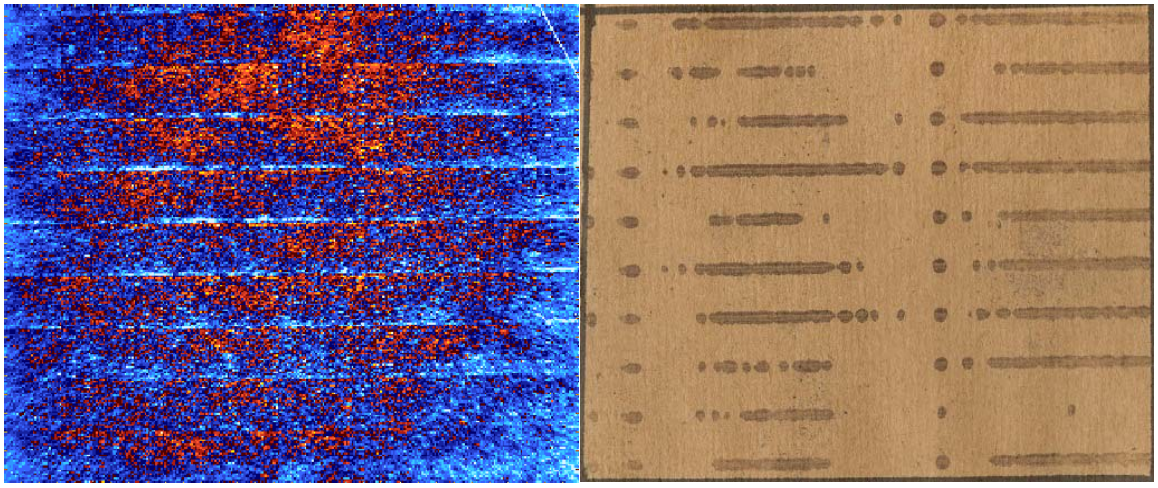

Figure 3.27 Glue roll gap too large

Figure 3.28 shows the IR–TSA response due to excessive glue lines. If the applicator roll's speed is to fast more adhesive can be deposited on one side of the flute than the other causing directional bond strength.

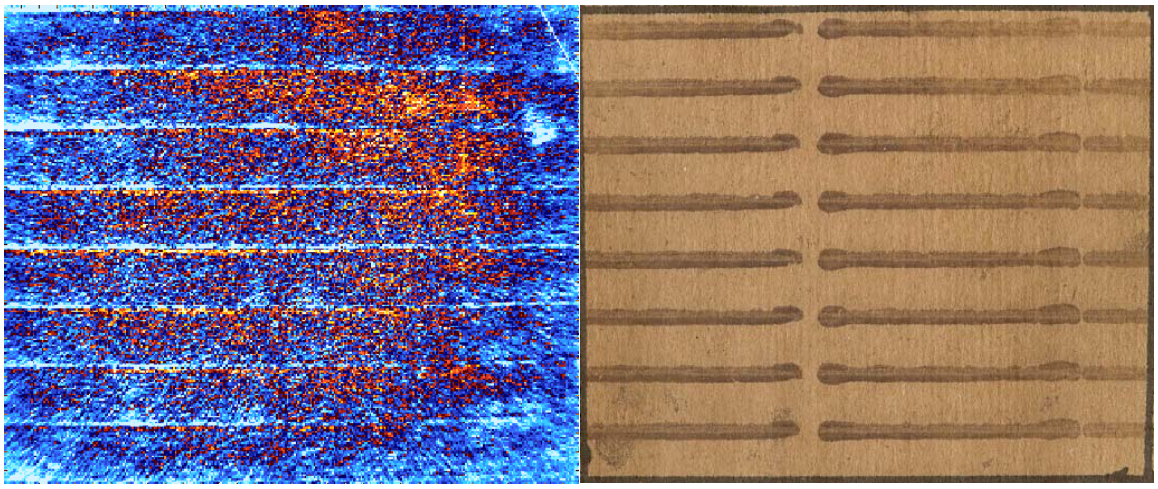

Figure 3.28 Applicator roll too fast

Figure 3.29 shows the IR–TSA response due to excessive adhesive. Excessive adhesive application may be caused by the metering roll or doctor blade gap being too great. This may cause white glue lines and low pin adhesion strength.

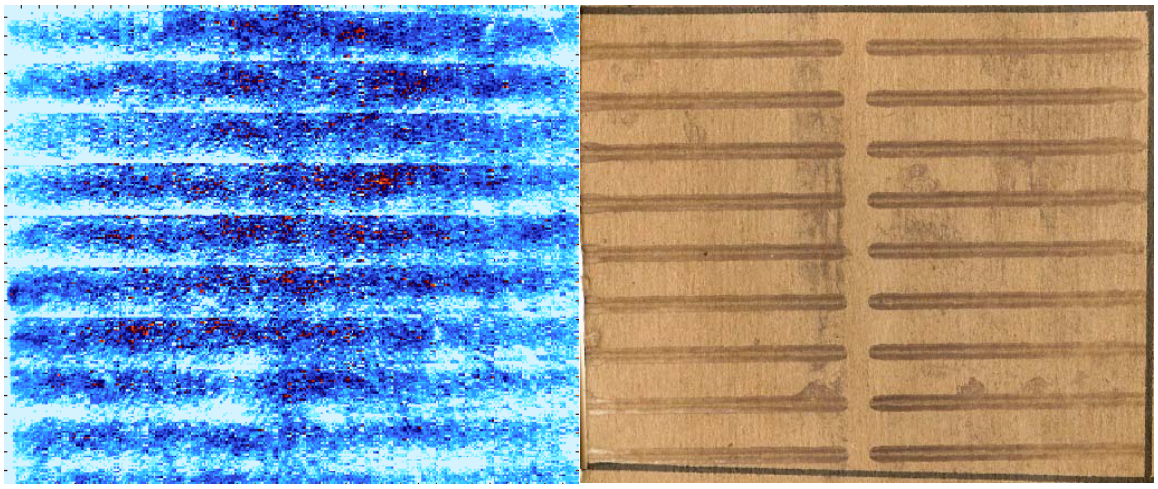

Figure 3.29 Excessive glue lines

Figure 3.30 shows the IR–TSA response due to excessive adhesive. If the clean–out finger recess is too great excessive adhesive can be deposited at the finger lines.

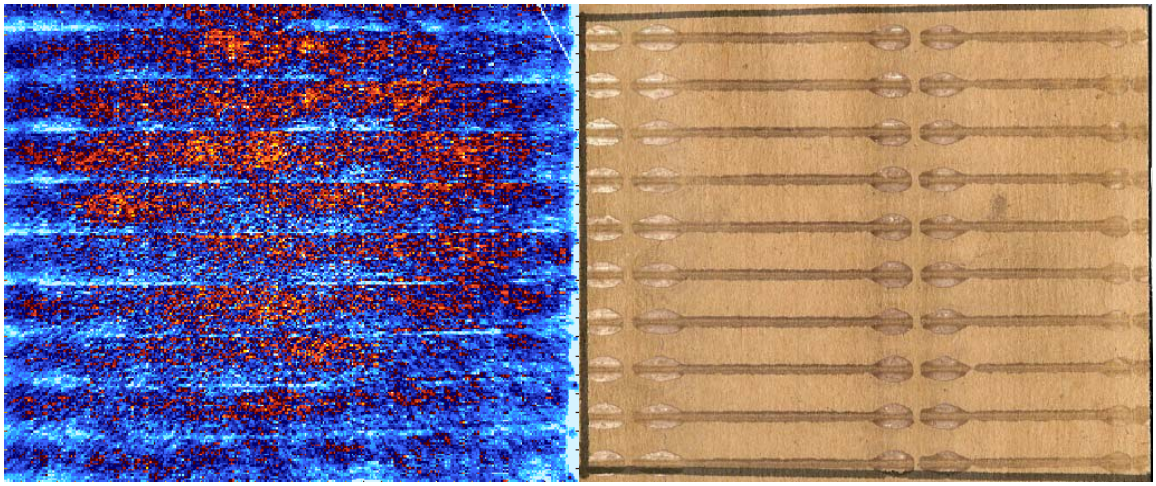

Figure 3.30 Clean out finger too far out

Previous specimens are tested by loading cyclically in the MD or CD directions. A new off–axis testing setup was also built and tested in this study. The corrugated materials are loaded at an angled orientation (off–axis) as shown in Figure 3.31 in order to enhance contrast in the

glue lines. The stress that will exist in the glue lines is a combined plane stress state including two normal stresses and shear.

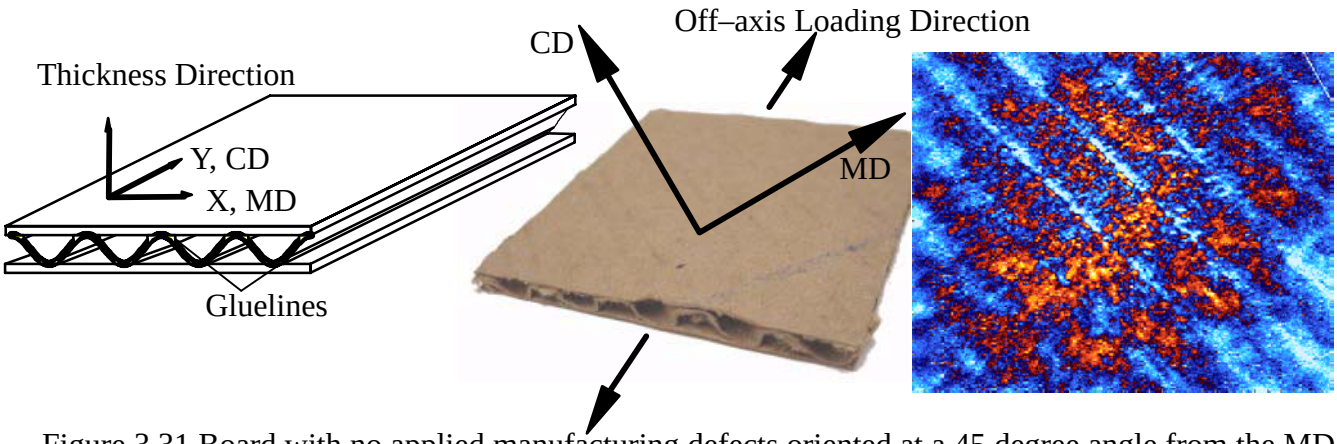

Figure 3.31 Board with no applied manufacturing defects oriented at a 45 degree angle from the MD

Stress concentrations due to the board geometry are undesirable, and it is necessary that the effect of the board geometry is analyzed. Towards that goal, an I shaped specimen is selected to prevent failure a the grip section of the board, however, it is desirable to obtain a specimen with a uniformly stressed area to analyze the effect of anomalies, on the other hand. A 13" by 10" board with circular cuts to reduce the net section to 2.5" is selected for various studies. To analyze the effect of stress concentrations of this board geometry finite element models are created and analyzed using Abaqus general purpose FE code. The material properties of the specimen are calculated from FE–simulations for the equivalent medium.

Table 3.1 Corrugated Board Material Properties

Thickness	0.16 in
E11	117.4608 ksi
E22	73.71 ksi
G12	18.476 ksi
ν_{12}	0.14428

The model consisted of 100 general purpose plane–stress elements, CPS4R. For the loading, a one percent displacement (0.13 in) is applied to the model (1 percent of the total length, 13

inches). The FE–simulation is performed under displacement control and one percent nominal strain was applied to the model. Stress/strain results due to a unit tension displacement applied in the MD direction are not uniform. While the stress and strain fields in the CD direction are relatively uniform, loading in the CD does not highlight bond quality issues when compared to loading in the MD. Straight coupon geometries of specimens loaded in the MD are needed for consistent measurements of bond quality in corrugated board.

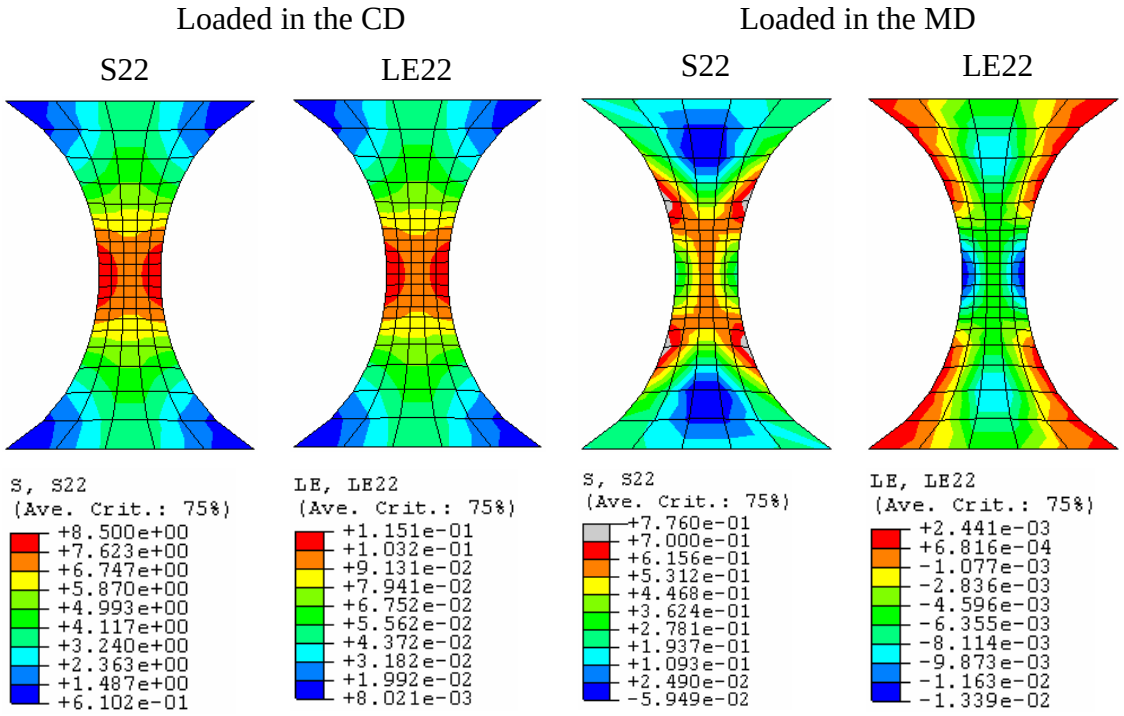

Figure 3.32 Finite Element Analysis results under unit displacement

As you can see from the finite element results, the geometry effects are important. Alternate geometries must be investigated to obtain a more uniform stress condition. A geometry that shows a more uniform state of stress where the IR images are taken is the preferred testing setup.

3D Finite Element modeling of glue lines

Our effort is to investigate the glue quality using infrared thermography and to correlate these effects with potassium iodide stains, finite element analysis, and known manufacturing

defects. Specimen geometry is one question of particular interest in this study because orientation of the specimen to loading has shown varying levels of contrast in the glue lines. The objective of this section is to create finite element models of different geometries to show the effect of the gluelines on the geometry of the fiberboard structure and to correlate the stresses in the corrugated structure experiment. Figure 3.33 shows the nonlinear load/deformation response of corrugated board with various glue line geometries.

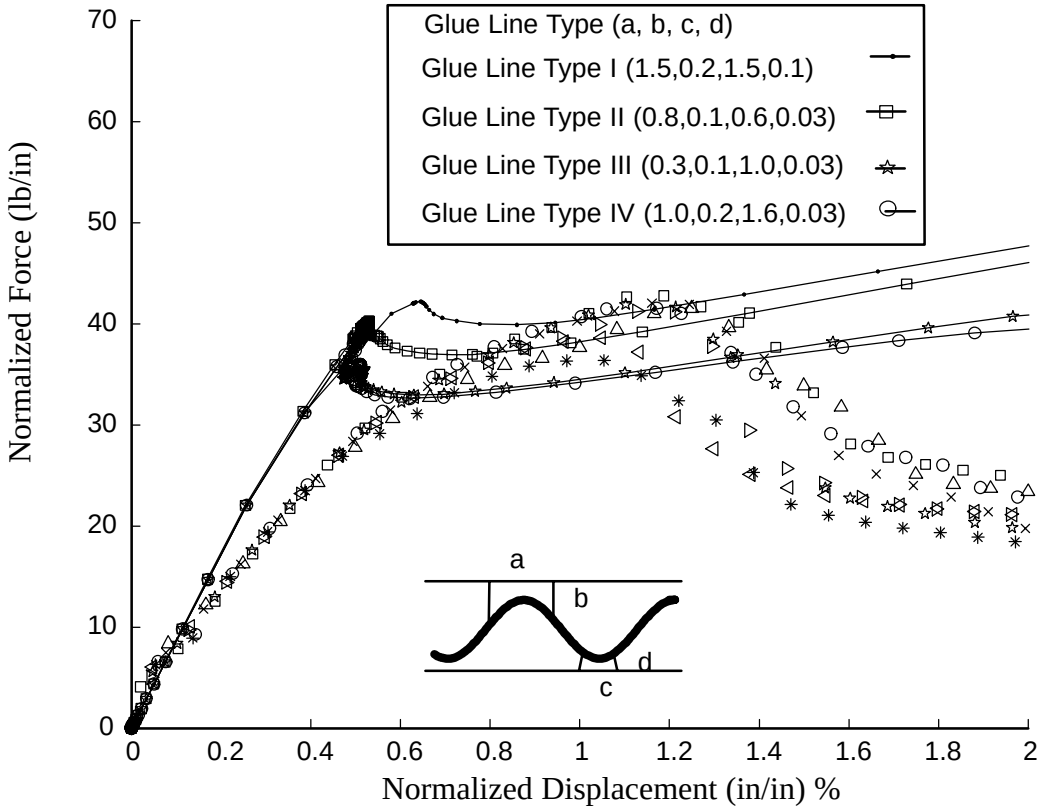

Figure 3.33 Nonlinear three–dimensional (3D) FEA

The FE models included at 2” X 10” and 4” X 10” 3D corrugated structures for both the MD and CD directions. These models have thin and wide glue lines on the single back side of the structure and slightly thicker and narrower glue lines on the double back side. The geometry of the glue lines corresponded to the measured glueline geometry using a caliper. From these

measured values a non–linear analysis shows reasonable correlation with experimental load/displacement relationships.

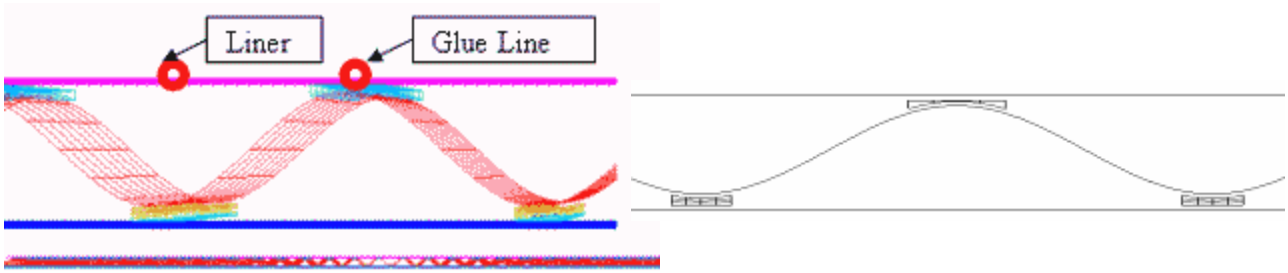

Figure 3.34 Finite Element Model geometry showing 3D single and double back glue–lines

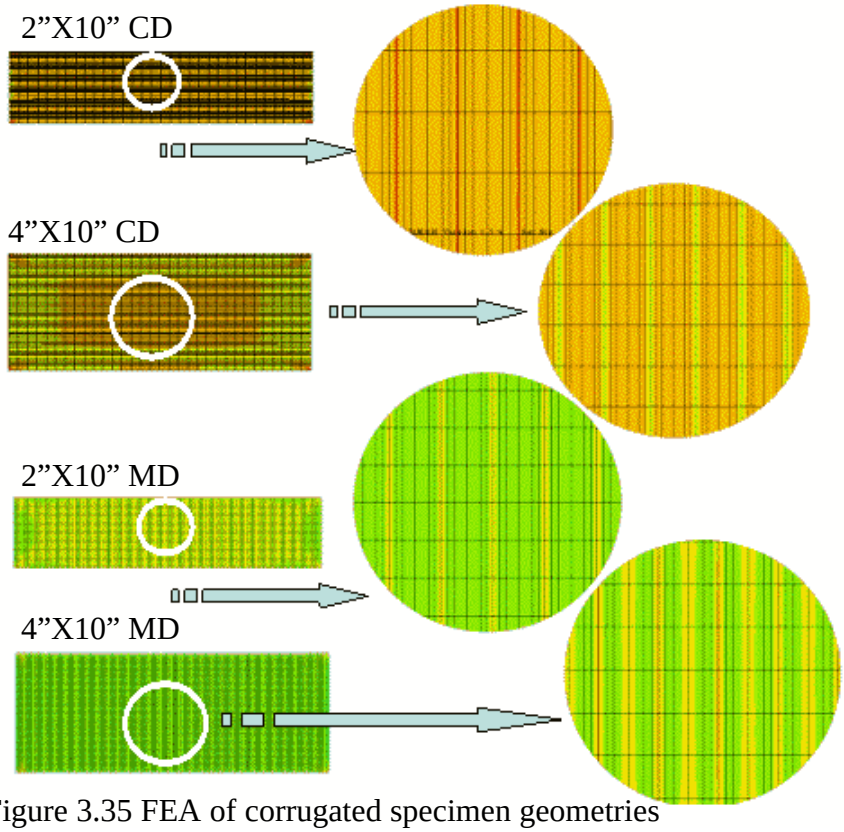

Figure 3.35 FEA of corrugated specimen geometries

The following tables (Table 3.2 to Table 3.5) show the linear analysis performed with the previously mentioned four different corrugated specimen geometries. Boundary conditions are applied to the structure by fixing the short side of a 2”X10” or 4”X10”. One percent strain is applied to the fiberboard structure in either the MD or CD directions.

The stress and strain values at nodes at the glue lines and between them were compared at the mid width of the specimen. Specific strain values and their invariants are investigated. The results are used to focus the testing on the coupon geometries/loading schemes that help produce the greatest contrast in the thermoelastic effect between the liner and gluelines.

Table 3.2 FEA results for 2” by 10” fiberboard specimen loaded in MD

	Double Back	Double Back	Single Back	Single Back
	Liner	Glueline	Liner	Glueline
Strain in MD	1.01E–2	8.40E–3	1.02E–2	1.17E–2
Strain in CD	–1.33E–3	–1.31E–3	–1.29E–3	–1.29E–3
Sum of Strain	8.77E–3	7.09E–3	8.91E–3	1.04E–2
% Difference Liner/Glue-line		19.16		16.84

Table 3.3 FEA results for 4” X 10” fiberboard specimen loaded in MD

	Double Back	Double Back	Single Back	Single Back
	Liner	Glueline	Liner	Glueline
Strain in MD	1.02E–2	8.07E–3	9.69E–3	1.23E–2
Strain in CD	–1.34E–3	–1.34E–3	–1.32E–3	–1.32E–3
Sum of Strain	8.86E–3	6.73E–3	8.37E–3	1.10E–2
% Difference Liner/Glue-line		24.0		31.2

Table 3.4 FEA results for 2” by 10” fiberboard specimen loaded in CD

	Double Back	Double Back	Single Back	Single Back
	Liner	Glueline	Liner	Glueline
Strain in MD	–7.69E–4	–1.00E–3	–8.03E–4	–7.34E–4
Strain in CD	1.00E–2	1.00E–2	1.00E–2	1.00E–2
Sum of Strain	9.23E–3	9.00E–3	9.20E–3	9.27E–3
% Difference Liner/Glue-line		2.5		0.75

Table 3.5 FEA results for 4” X 10” fiberboard specimen loaded in CD

	Double Back	Double Back	Single Back	Single Back
	Liner	Glueline	Liner	Glueline
Strain in MD	–7.81E–4	–1.01E–3	–8.14E–4	–7.48E–4
Strain in CD	1.01E–2	1.01E–2	1.01E–2	1.01E–2
Sum of Strain	9.32E–3	9.09E–3	9.29E–3	9.35E–3
% Difference Liner/Glue-line		2.46		0..71

The 4” X10” specimen loaded in the MD direction showed the greatest glue line effect on the single back and double back side of the structure because the difference in the sum of the in plane stresses or strains are greatest in this loading direction. Both FE specimens in the CD direction showed the greatest glue line effect on the double back side of the structure, but the effect of loading in the CD direction on the TSA response is approximately 4 times less significant than loading in the MD direction shown from the FE results. The stiffness in the CD direction for a tension loading case is much greater than the stiffness in the MD direction because the flutes and the liner are acting together along the length of the specimen. Loading in the MD direction produced discontinuities in the stress values at the glue lines. From these results we expected for a uniaxial loading on the structure that the greatest % difference in the TSA values between the liner and glue line to be approximately 20% to 30%. If the selection of the corrugated board specimen is between 4”X10” and 2”X10” fiberboard specimen loaded in the MD and CD, the greatest effect is in a 4”X10” specimen loaded in the MD direction. Note that an increase in contrast in the TSA response is expected due to doubling the width of the specimen from 2” to 4”.

3.10. Developed Software for Detecting Anomalies and Properteies of Corrugated Boards

Matlab code was developed in this study in order to process the IR images using Matlab's image analysis toolbox and its flexible programming capabilities. A description of various aspects of the software are described in this section. The input to the program is an infrared image where each pixel is in camera units. The final output of this program is a ".jpg" or similar image file. The step by step objectives of this software are to filter the specimen from its surroundings, locate and encapsulate stress concentrations, and finally analyze the output to better understand the spatial sensitivity of TSA for use with corrugated board.

To begin, edge command is used to create a matrix of binary values later used to filter the specimen from its surroundings. Different metrics may be acquired from the the tsa values in order to obtain results that may be helpful once the background noise is filtered out. For this project we will choose to encapsulate thermoelastic stress concentrations. A concentration in the infrared image can be spatially distributed, so a threshold can be defined to filter the extreme values from the boundary image. Then the edge command can be used again to encapsulate the distribution values that remain in the mask image. The edge command first captures small pockets of TSA values spatially. The edges can be made thicker to produce the dilated gradient image. The space between the thicker lines is filled as long as they are connected to create the binary image with filled holes. The edges of the encapsulated values are smoothed over with a diamond structuring element twice to create a segmented image. The final step is to filter out small outlying pockets of TSA concentrations from the segmented image.

Intermediate image processing steps were used to obtain encapsulated TSA stress concentrations. The final image takes the segmented image and filters out concentrations less than an area of 30 pixels.

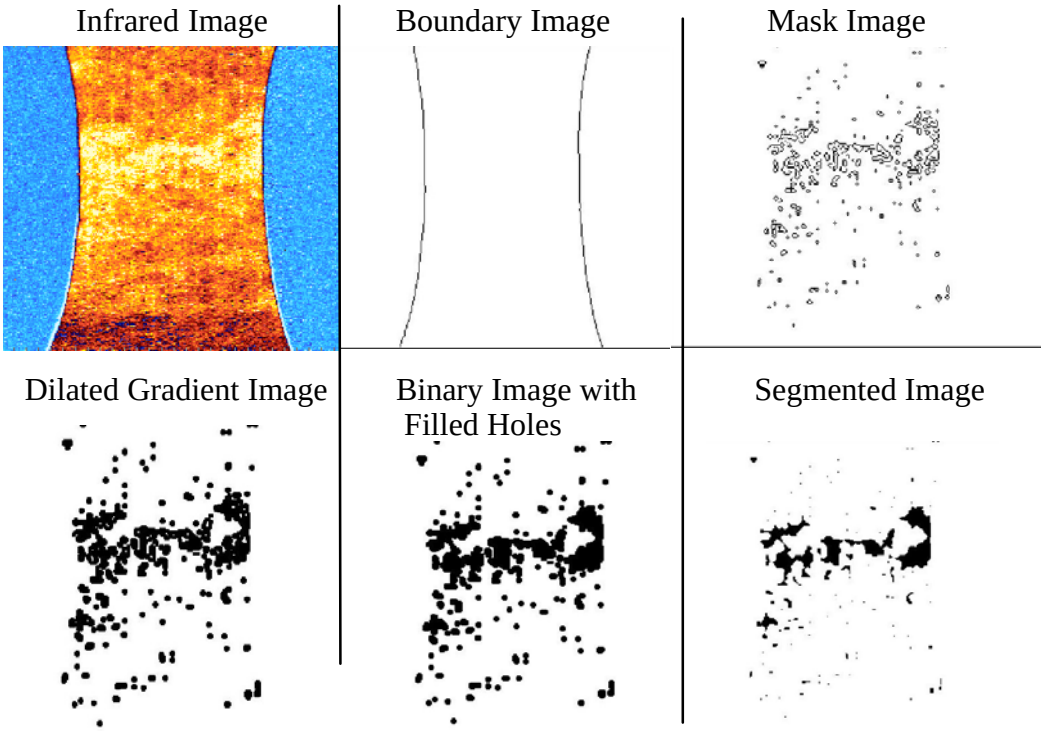

Figure 3.36 Selected intermediate images processed to obtain encapsulated TSA stress concentrations

The ability of the developed software to detect anomalies is demonstrated in the case of wood shives in paperboard. The detected wood shive is shown in the fiberboard in Figure 3.19 The images leading to automatically detecting the wood shives from stress concentrations are shown as an example in Figure 3.37 The Figure shows the ability of the software to filter anomalies from the data, and various damaged areas noticed due to the nip pressure applied by the pressure roll during manufacturing.

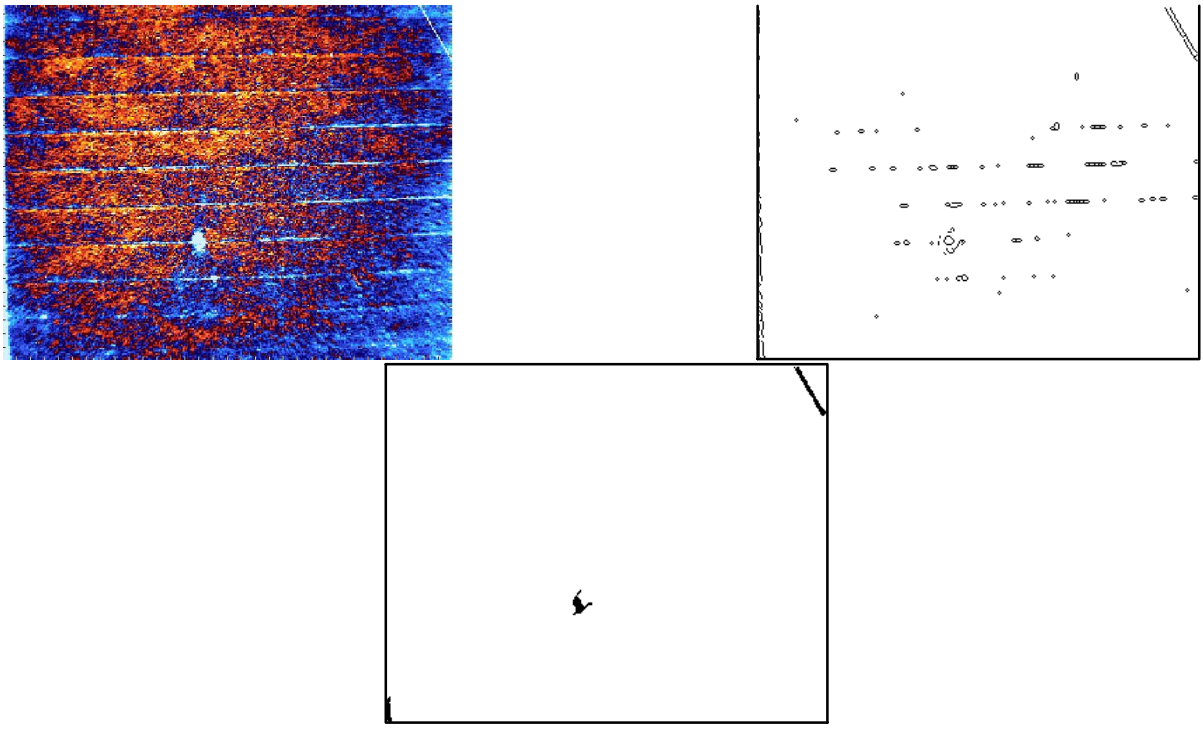

Figure 3.37 Software for detection of manufacturing anomalies

3.11. Differential Infrared Thermography for Cumulative Damage

The objective of this section is to correlate damage in the flutes with IR. One method for detecting damage is subtraction of TSA images of the specimen with a reference image from a non–damaged specimen. This section will describe in details the experimental steps used and show how damage can be detected in the medium of corrugated board without any visible damage to the liner. The following are the experimental steps:

Step 1: Cut a uniform corrugated specimen. The specimen chosen as an example was arbitrarily selected as 4” X 10”.

Step 2: Coat the liner viewing area with flat black paint for emissivity. This is only done in the case that the surface of the board is shiny due to a wax coating or similar reflective coat. In addition, the paint can increase the TSA effect.

Step 3: Load the specimen, and take infrared pictures.

Step 4: Test the specimen under tension–tension displacement control (0.014 in amplitude) at a frequency of 3Hz. A combination of frequency and displacement may be altered to increase infrared sensitivity (contrast between liner and glue lines).

Step 5: Damage the medium (In Figure 3.39 A thin metal rod is inserted into the flutes and two of the glue lines are damaged to remove the connection between the flutes and the liner.)

Step 6: Now process the images. Blue colors correspond to glue lines. Red/yellow colors correspond to bare portion of liner.

Step 7: Subtract damage state images from initial undamaged image.

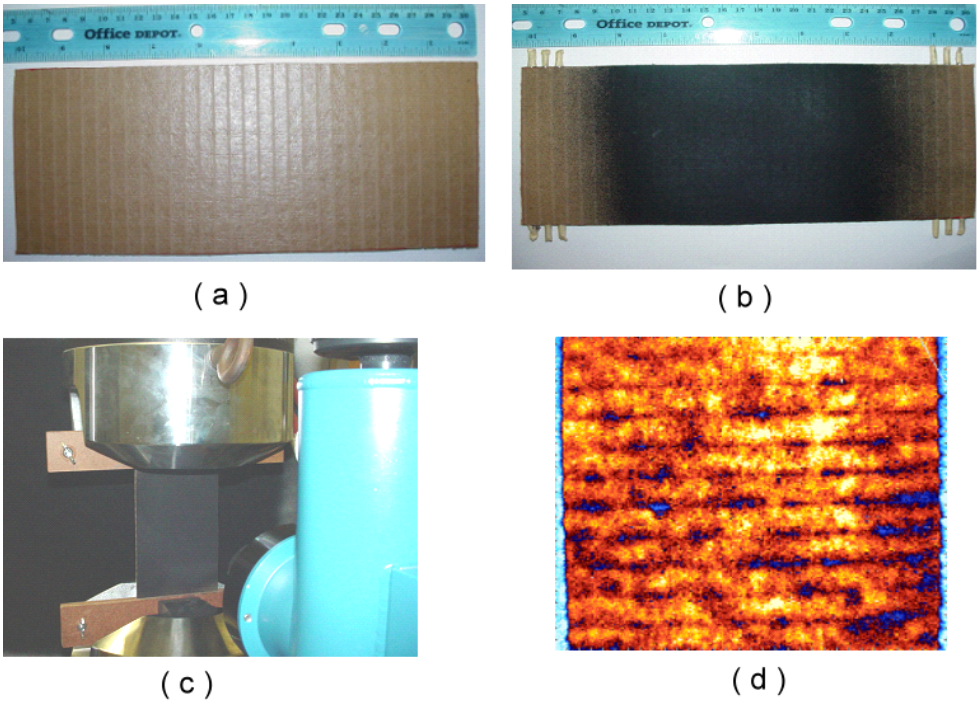

Figure 3.38 Designed test setup for uniform corrugated boards

Figure 3.38 describes (a) a 4” X 10” transverse specimen, (b) a specimen painted with flat black paint, and steel pins are inserted into the grip section of the board to increase stiffness of gripped area and allow for a uniform applied load, (c) the IR–TSA setup, and (d) the corresponding TSA image.

A series of subtracted TSA images in Figure 3.39 to 3.41 show clearly the effect of progressive debonding of the flutes from the single face liner. The subtracted images in Figure 3.41 correspond to the TSA images shown previously.

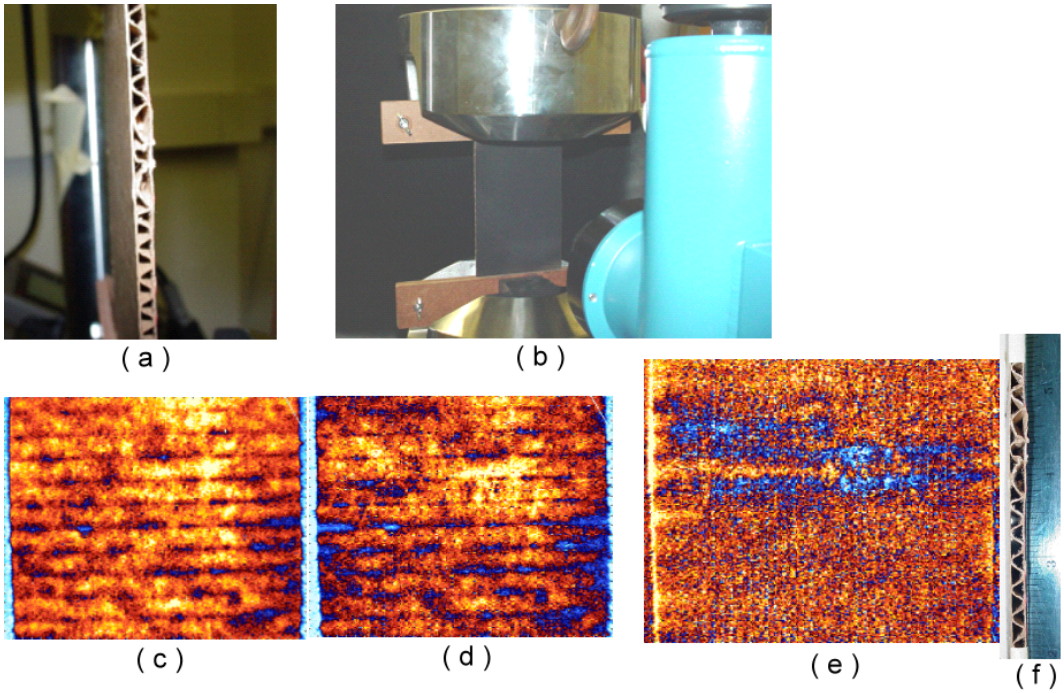

Figure 3.39 Infrared investigation of gluelines on the single back and dobule back liners: (a) Final applied damage state of the corrugated specimen, (b) IR–TSA setup,
(c) TSA image of undamaged specimen, (d) TSA image of damaged specimen, (e) subtraction of undamaged specimen from damaged specimen, (f) Final applied damage state of the corrugated specimen.

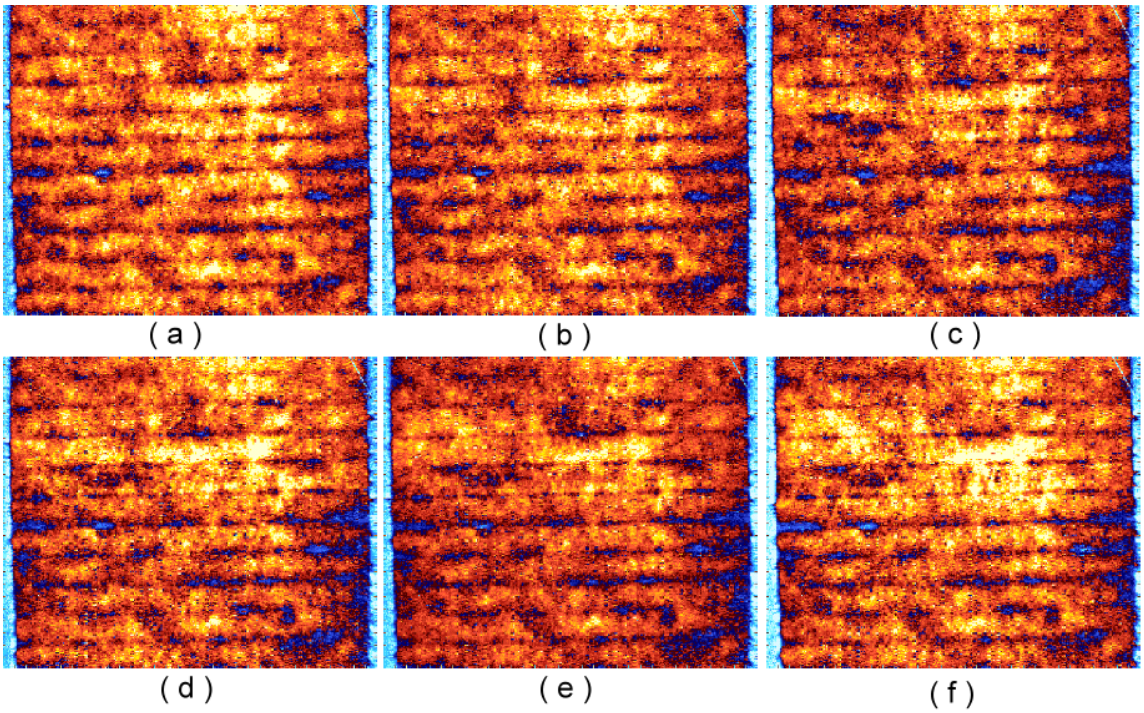

Figure 3.40 TSA images showing little contrast between final and initial damage states.

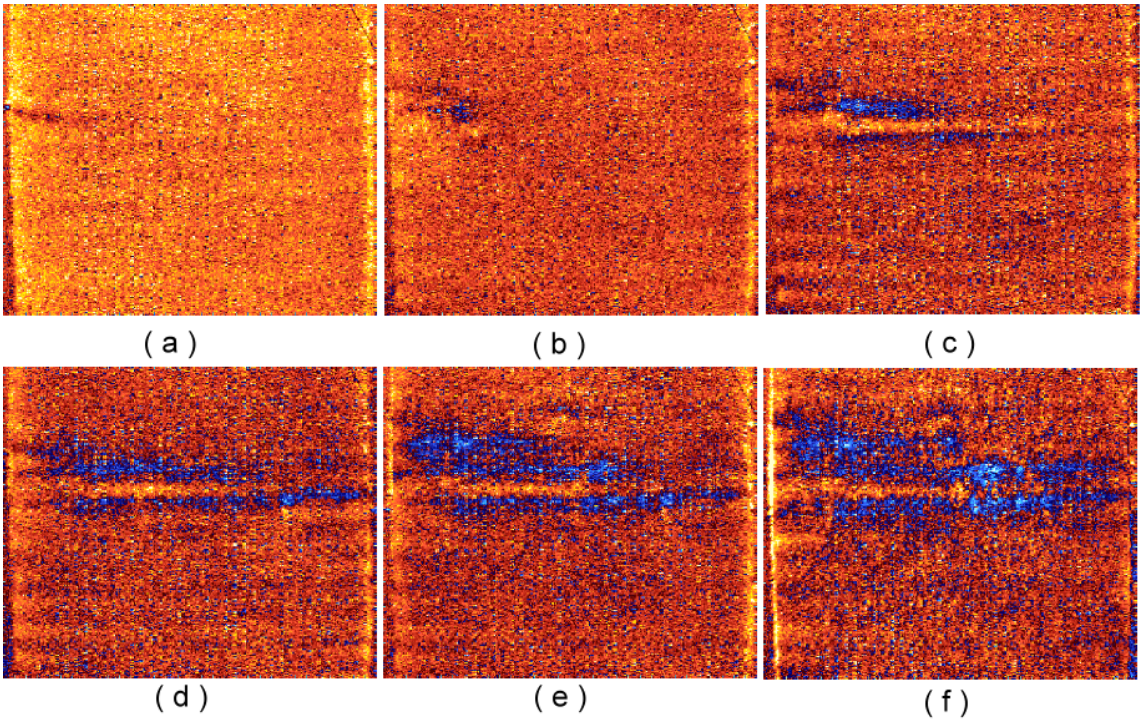

Figure 3.41 TSA image subtractions showing progressive debonding of flutes from single back liner

Several possible improvements can be applied to the previously developed processing method. For example, a thin allen wrench was used to apply the damage to the glue line. A sharp thin metal string may be used to cut the glue from the liner for a less crude method for damage application to the medium of the corrugated board. In addition, a parametric study analyzing the relationship between TSA sensitivity and frequency, amplitude, and geometry is needed for several classes of fiberboard materials to determine ways to maximize the contrast between the overall material and the damaged areas. These tests may provide insight on boards of varying glue line quality and anomalies can be generated to create a reference library of anomalies that can be used in a manufacturing environment.

3.12. Summary of Key Conclusions

Thermoelastic stress analysis is shown to be an effective means of non–destructive testing of fiberboard systems for hidden damage and defects that can easily escape visual inspection. Several general and easily implemented methodologies are presented along with setups, sensitivity enhancement guides, and detection tools provide industry with a toolbox of examples to investigate various product enhancement interests. General setups and methodologies are developed with the intent of saving industry valuable time and capital for implementation of infrared thermography in a manufacturing environment. Combinations of mechanical and thermal excitation sources have been investigated not only to show the possibilities of defect detection using infrared thermography, but various setups have also been presented to encourage the use of infrared thermography by providing a helpful guide for what works and what doesn't work with current infrared technologies. General conclusions from this study are:

Damage and anomalies can be detected in corrugated board with TSA–IR and other IR– techniques.

Several Major Mechanical IR–TSA Testing Setups are designed

Different damage systems can be detected, such as hidden crease lines, discontinuous and crushed flutes, and hidden cutouts and cracks.

Active glue lines can be assessed and a proposed quality technique is proposed

Differential damage detection is shown to increase damage sensitivity

A portable material testing system (PMTS) using other excitation sources is conceptually developed, and it can be used to investigate the quality of the corrugated board during/after the manufacturing process.

Laboratory experiments lead to the design of a portable system for routine inspections in production environments. The development of specimen geometries for mechanical loading and loading fixtures has allowed us to better characterize the sensitivity of the IR–TSA method for corrugated board. Mechanical testing has shown the greatest promise for detecting damage, and certain anomalies can be investigated using this method including some damage induced may manufacturing.

3.13. Future Experimental Studies, Fracture Mechanics Analysis and Measurement Techniques for the Design of Wood and Fibrous Materials and Structures

One outcome of the previoius IR–TSA study for damage and property detection is to use IR in the study of fracture and tearing of paper and fiberboards. An innovative experimental and analytical study is proposed for the assessment and modeling of the fracture toughness and tearing resistance properties of fiberboard structures. A new technique is proposed in this section to determine mixed mode stress intensity factors, KI and KII, for anisotropic materials using Thermoelastic Stress Analysis (TSA) coupled with a theoretical fracture solution of the mixed–mode stress singularity around crack tips. A numerical method is proposed to use the mixed–mode solution and correlate it with the TSA measurements to obtain accurate stress fields around the measured crack tip. The proposed measurement technique coupled with fast CCD, IR or optical, cameras can instantaneously (Live) capture or acquire the full stress or displacement fields around cracks and inclusions and thus report fracture and toughness measures of the paper materials and structures.

Methods for testing fracture resistance are used to evaluate the runnability of fiberboard or to characterize the toughness and tearing resistance of packaging papers where the ability to absorb shocks is important. Traditional methods of measuring the fracture mechanics properties of paper may include testing with the Elmendorf tear tester or in plane testing of single edge notched specimens to obtain overall averages of fracture resistance. Traditional testing methods show a wide range of experimental behavior, and one must decide on how the experimental results relate to the specific application. Limited research has been done on the fracture mechanics of wood that takes into account the heterogeneity of wood such as the spatial variability of stiffness due to annual rings. The research has been limited to studies on cell–wall substances or stress concentrations around knots.

Yamauchi et al. (2000, 2003) studied the fracture properties of paper using infrared thermography. They tracked the distance between maximum temperatures as indicators of the crack tip locations in a double edged notched tension specimen while simultaneously measuring crack opening displacement with a CCD camera. They are able to detect differences in the temperature distribution due to a transition between stable and unstable crack growth. Temperature changes are closely related to crack opening displacement. Yamauchi et al. investigated alternative testing methods to the Elmendorf tearing test for use with imaging techniques and thermography. They showed that a tensile tester based on the trouser tearing test can be employed as a substitute for the Elmendorf tearing test. They investigated the effect of varying testing rates and the number of plies to find no practical difference between the two methods. Ando et al. (1999) used Finite Element Analysis (FEA) and experimental techniques to evaluate the effect of the heterogeneity of the elastic modulus and strength within an annual ring and changes in the degree of stress concentration at the crack tips on the variability of KIC. Fracture toughness KIC is measured using a clip gage and calculated using isotropic equations.

Stress concentrations are found to increase with relative position of the crack tip within an annual ring, and Finite Element modeling shows relatively similar trends with experimental results.

A new method can be proposed that couples the relation between the first strain invariant and thermoelastic stress analysis (TSA) with numerical methods to determine stress intensity factors (SIFs), KI and KII, under mixed–mode loading conditions. The method employs Lekhnitskii's (1963) solution together with the least square method to investigate notched anisotropic material systems similar to Mushkelishvili's approach for isotropic materials. An infrared camera is used to provide the full–field thermoelastic data. The method requires a map of the thermoelastic data at specific locations around the crack tip to determine stress intensity factors. Traditionally, the thermoelastic data could be directly related to the first stress invariant by calibrating two thermal coefficients. El–Hajjar and Haj–Ali (2003) used an approach which related the thermoelastic data to the first strain invariant by a constant. Figure 3.42 shows the TSA response of tearing and fracture of fiberboards.

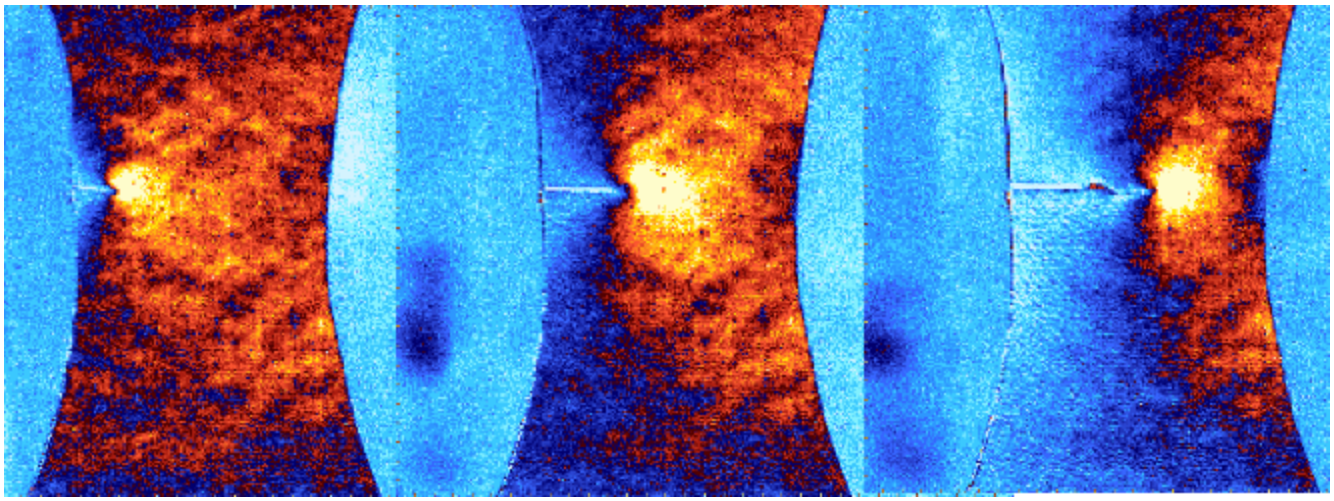

Figure 3.42 Fracture of fiberboards

The infrared signal, S, can be related to the first invariant of strain by a constant.

$$I^{IR} = k_{\epsilon} S \tag{3.1}$$

Therefore, the least squares method can be applied to minimize the sum of squares error of the first strain invariant measured by IR. The residual of the error is defined as

$$R = \sum_{i=1}^{m} \left(I^{(LK)} - I^{(IR)} \right)^2 \tag{3.2}$$

Minimizing the residual yields:

$$\frac{\delta R}{\delta \beta} = 0 \tag{3.3}$$

The infrared signal can be related to the first strain invariant, and the stress intensity factors near the crack tip can be evaluated by

$$K_I = -\sqrt{(2\pi)} \left[\left(1 - \frac{\beta_1^*}{\beta_2^*} \right) \beta_1 + \frac{\left(\alpha_2^* - \alpha_1^* \right) \beta_{n+1}}{\beta_2^*} \right] \tag{3.4}$$

$$K_{II} = -\sqrt{(2\pi)} \left\{ \left(\alpha_1^* - \alpha_2^* \frac{\beta_1^*}{\beta_2^*} \right) \beta_1 + \left[\beta_2^* - \beta_1^* + \alpha_2^* \frac{\left(\alpha_2^* - \alpha_1^* \right)}{\beta_2^*} \right] \beta_{n+1} \right\} \tag{3.5}$$

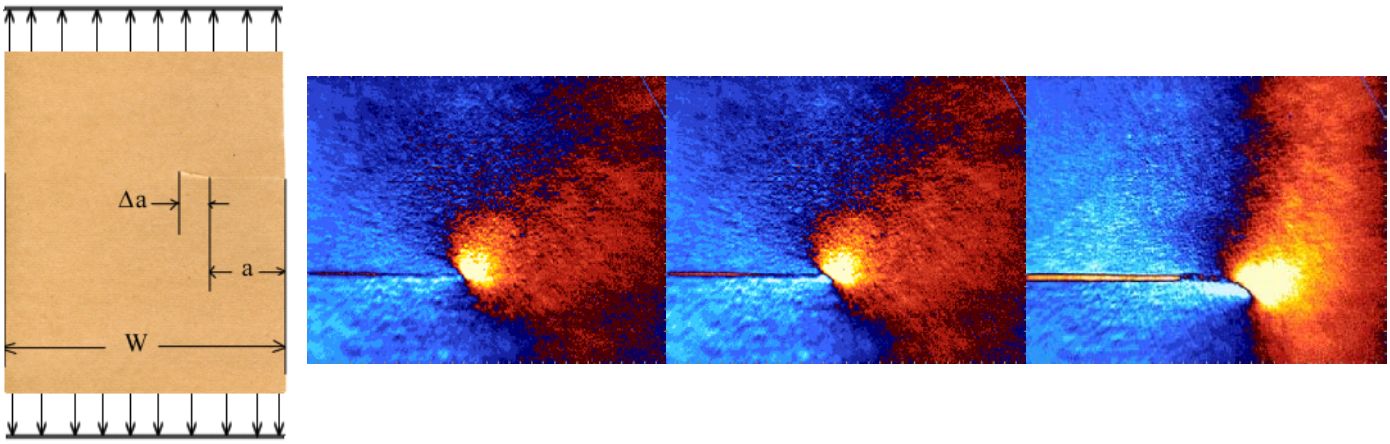

Figure 3.43 Single edge notched fiberboard specimen and corresponding TSA images during crack extension.

Figure 3.43 illustrates the proposed approach for toughness measure applied to a single edge notched fiberboard specimen and shows the corresponding TSA images during crack extension. The proposed method employs the first strain invariant, and derived the strain expansions from Lekhnitskii's solution, in which the full–field thermoelastic data optimized by least square method is used. This method has not been fully developed and further studies are needed. It

is merely proposed as a direct outcome of the previous quantitative and qualitative NDE IR–TSA studies in the previous sections.

CHAPTER 4

Infrared Thermography for Fatigue Damage Detection in FRP Composites

4.1. Methodology

The fatigue part of this study explores the use of quantitative infrared (IR) thermography measurements to describe the fatigue damage process in multi–layered glass–fiber reinforced polymer (FRP) composites. The temperature changes on the surface of an FRP composite caused by damage during fatigue are tracked and thermoelastic stress analysis (TSA) technique is developed to relate the surface deformation to the IR emission. Under adiabatic and reversible conditions (fatigue), the application of a small load will induce small and repeated variations in temperature that are proportional to the first stress invariant (for isotropic materials) and to the sum of the in–plane strains (for orthotropic layered medium). Live monitoring of the damage process is performed for a S2–glass/epoxy prepreg and thick–section E–glass/polyester FRP composites. Different statistical methodologies can be utilized to analyze the rich full–field IR–TSA measurements, to determine different distributions, parameters, and their evolution up to ultimate failure. The damage evolution is characterized using the proposed IR–TSA method along with a full–field data reduction approach. The fatigue and damage behavior of different fracture and notched specimen are examined in this study. The proposed testing approach shows increased sensitivity than the classical fatigue tests using coupon compliance degradation measures.

4.2. Experiments with S2–glass/Epoxy

Open–hole specimens were cut with a diamond abrasive wet saw from a quasi–isotropic S2–glass/epoxy panel (See Table 2.1) and drilled with a brad point drill bit. A 12” by 16” panel was manufactured using an autoclave using the manufacturer’s specifications to achieve a

uniform thickness of 1.78 mm (0.070 in) for the quasi–isotropic system. The specimen was sprayed with flat black paint and cyclically loaded in tension–tension control with a maximum load of $0.5\,\sigma_{ult}$ where $\sigma_{ult} = 322\,MPa\ (46.7\,ksi)$ with R = 0.1 and a frequency of 5 Hz. The test was stopped randomly at intervals between 10–40 minutes to take stiffness measurements with a 2 in gage length extensometer centered over the open–hole specimen. The TSA images of the specimen were obtained using automatic acquisition every minute during the loading. The effective initial elastic properties of the un–notched laminate are given in Table 4.1

Table 4.1 Effective properties of Quasi–isotropic S2–glass/Epoxy

System	Unit	E_{11}	E_{22}	G_{12}	v_{12}
S2–Glass/ Epoxy $[-45/0/45/90]_s$	GPa (Msi)	26.7 (3.879)	26.7 (3.879)	17.5 (2.536)	0.307

4.3. Results of Fatigue Testing with S2–glass/Epoxy

The remote stress–strain and ultimate tensile strength for the open–hole tension specimen are shown in figure 4.1 where the stress has been computed over the remote gross (un–notched) cross–sectional area and strain has been measured with an extensometer mounted over the notch.

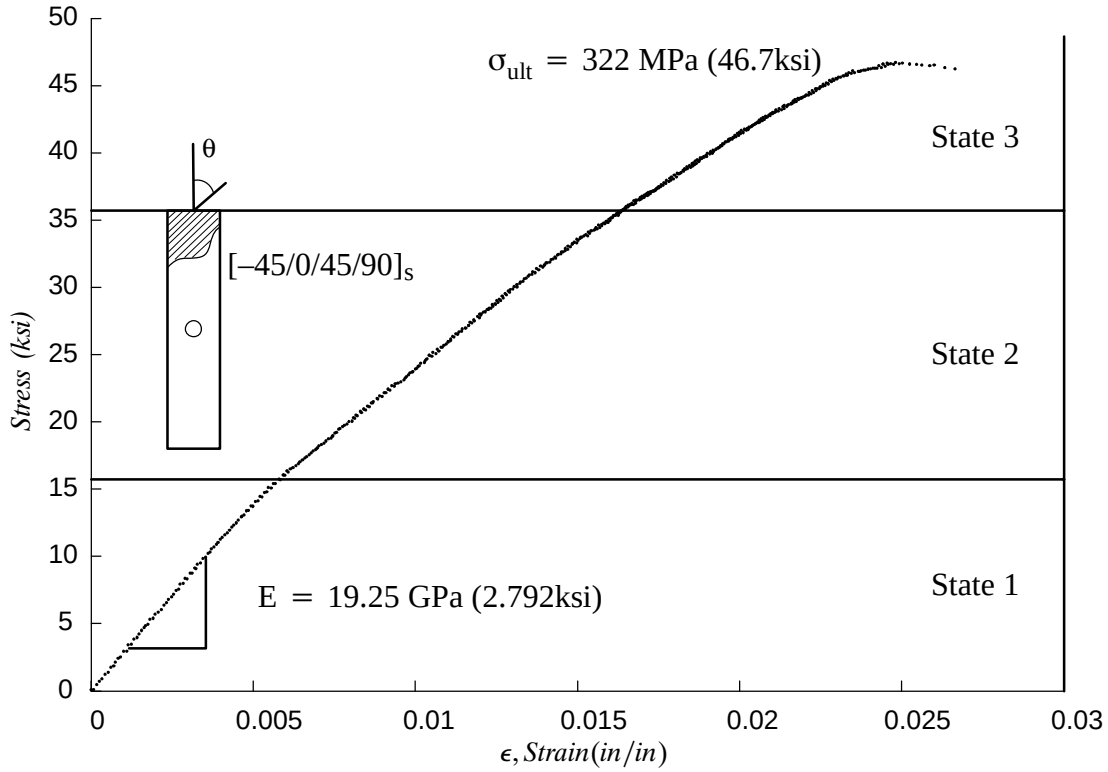

Figure 4.1 Notched stress/strain response for quasi–isotropic $[-45/0/45/90]_s$ S2–glass/epoxy lay–up

A "knee" in the stress/strain curve just above 15 ksi may be due to excessive hole deformations, and added nonlinear material behavior. This knee defines a transition from State 1 and State 2. Another transition is defined just above 35 ksi where delaminations are noted in this static loading case. A fatigue investigation of the S2–glass/epoxy open–hole specimen at load levels within State 2 follows.

To achieve fatigue lives on the order of 200,000 cycles a stress level of $0.5\sigma_{ult} = 322\ MPa\ (46.7\ ksi)$ was chosen for the quasi–isotropic laminate. Final failure occurs with progressive fracture of the 0 degree fibers after the laminate has lost much of its initial stiffness due to matrix cracking and delaminations. A typical normalized stiffness degradation response during the fatigue lifetime is shown in Figure 4.2. There is a uniform rate of degradation throughout the fatigue life of the specimen, and at the end of the fatigue life the specimen retains less than 20% of its original stiffness.

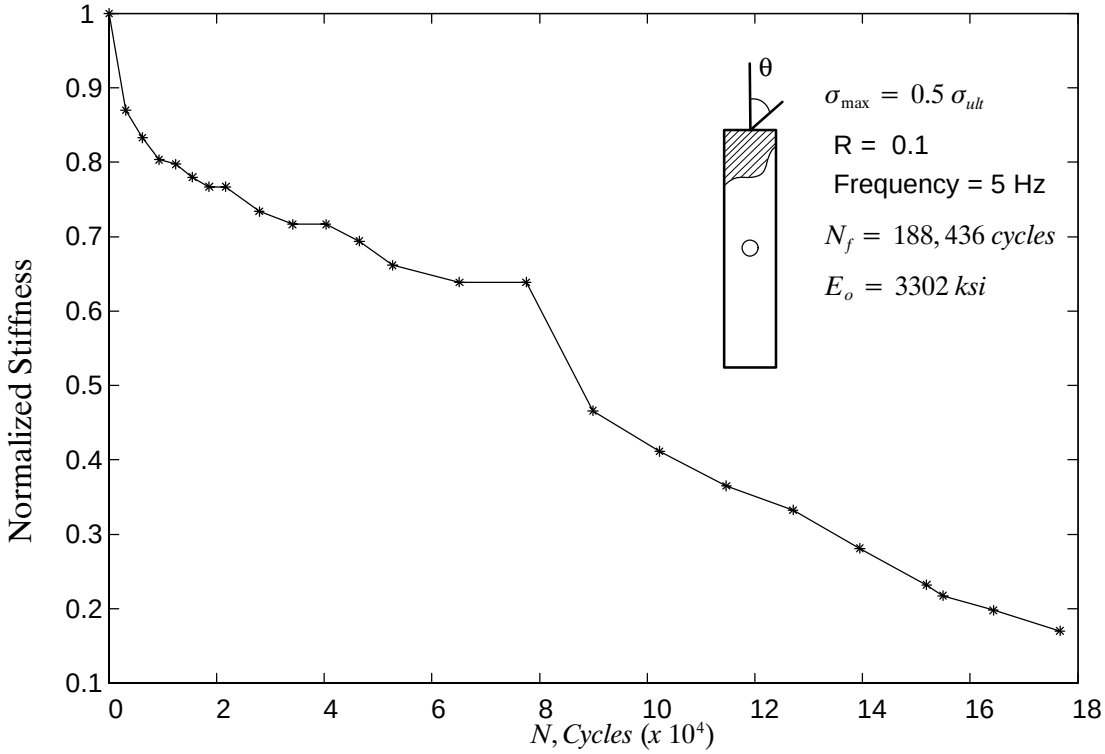

Figure 4.2 Normalized stiffness vs. cycles for tension–tension fatigue testing of quasi–isotropic S2–glass/epoxy open–hole specimen

Fatigue damage in the $[-45/0/45/90]_s$ laminate initiates at the notch with matrix cracking in all plies and matrix cracking in the surface ply at the straight edge. Delaminations at the –45/0 interface form early in the first load cycle due to the relatively large maximum load ($0.5\sigma_{ult} = 322\,MPa\ (46.7\,ksi)$), and these delaminations grow the fastest. Figure 4.2 shows a large drop in stiffness from approximately $0.64E_o$ to $0.47E_o$ ($E_o = 3302\,ksi$) at approximately 80,000 cycles. This event is due to in part to delaminations in the surface ply growing outside the 2 inch gauge length of the extensometer centered over the notch. Part of this stiffness drop may also be due to a strip of 0 degree fibers above and below the notch pulled from the laminate by the growth of delaminations in the surface ply. Delaminations extend across the width of the specimen in the surface ply as early as 20,000 to 30,000 cycles. The delamination of the surface ply is followed by matrix cracks in the 90 plies. Once the cracking in the 90 degree plies has

moved from the center of the specimen to the grips, fiber fracture in the 0 degree plies further reduces the stiffness of the specimen and leads to final rupture.

Full field thermal emission of the front surface of the specimen was recorded during every minute of the fatigue test. The selected 4 images shown in figures 4.3 and 4.4 will be discussed here. Each image will be referred to by the number of cycles after it was taken (shown below each image). These images highlight different stages in the fatigue life of the notched quasi–isotropic specimen. The image at 300 cycles shows a relatively healthy specimen with matrix cracks immediately forming at the notch in all of the plies and damage in the surface ply at the straight edge. Between 300 and 3400 cycles damage due to matrix cracking and delaminations in the surface ply progresses quickly at various locations, and the growth of these damage effects follows the fiber's orientation on the surface to both straight edges.

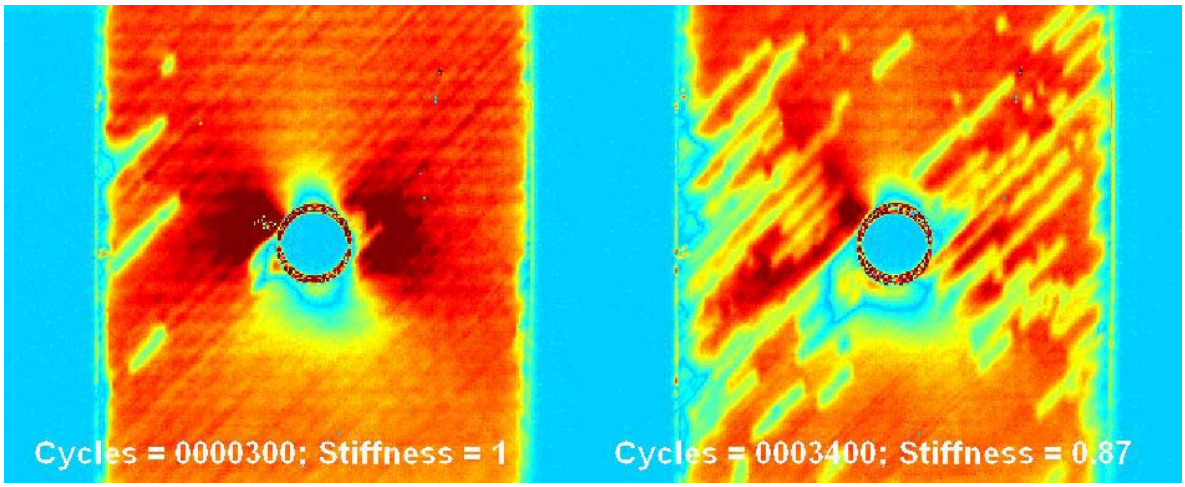

TSA after 300 cycles, Stiffness = 1

TSA after 3,400 cycles, Stiffness = 0.87

Figure 4.3 TSA images of quasi–isotropic S2–glass/epoxy open–hole specimen during initial stages of tension–tension fatigue

Between 18,240 and 80,000 cycles, the surface ply is effectively delaminated from the surface of the specimen with a host of non–adiabatic effects degrading the TSA signal at approximately 60,000 cycles. At 90,505 cycles the thermal emission shows some stress

concentrations as the 0 degree fiber strip below the notch. This fiber strip is being pulled from the laminate with the surface ply. Quantitative TSA measures are not meaningful after approximately 60,000 to 80,000 cycles due to saturation of the camera sensors even at a low electronic shutter due to both the internal heating of the material and the coupled non–adiabatic effects that also emanate from the edges.

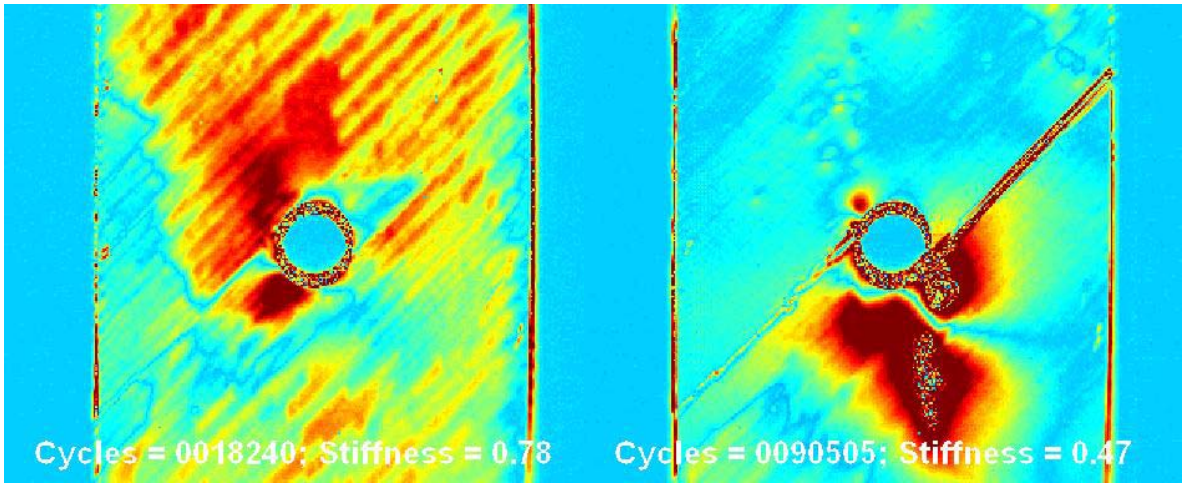

TSA after 18,240 cycles, Stiffness = 0.78 TSA after 90,505 cycles, Stiffness = 0.47

Figure 4.4 TSA images of quasi–isotropic S2–glass/epoxy open–hole specimen during progressive stages of tension–tension fatigue

Some interesting correlations can be made with the TSA to the damage state of the system. First the degradation and of the surface ply and growth of delamination fronts can be characterized in part by the measured TSA contour areas. Friction at the –45/0 interface and various non–adiabatic effects are noted after 60,000 cycles. Thermoelastic stress analysis even as a qualitative measure becomes ineffective for this specimen at a range between 60,000 and 80,000 cycles because the delamination of the surface ply masks meaningful thermal emissions. Excessive hole deformations due to the stiffness reduction during fatigue also reduce the amount of meaningful data within a small area at the hole edge.

Figure 4.5 shows the average TSA measurements after eliminating edge effects normalized at 60,000 cycles versus the number of cycles for the notched quasi–isotropic laminate. It can be seen from the figure some fluctuations in the TSA signal are present after 60,000 cycles, and the in–phase TSA data is not an accurate quantitative measure after this point. The various drops in the TSA signal during the test shown in Figure 4.5 are due to stopping the fatigue loading to measure the stiffness with the extensometer. These drops in signal are a measure of how much time is required for the specimen to achieve relatively steady state values again.

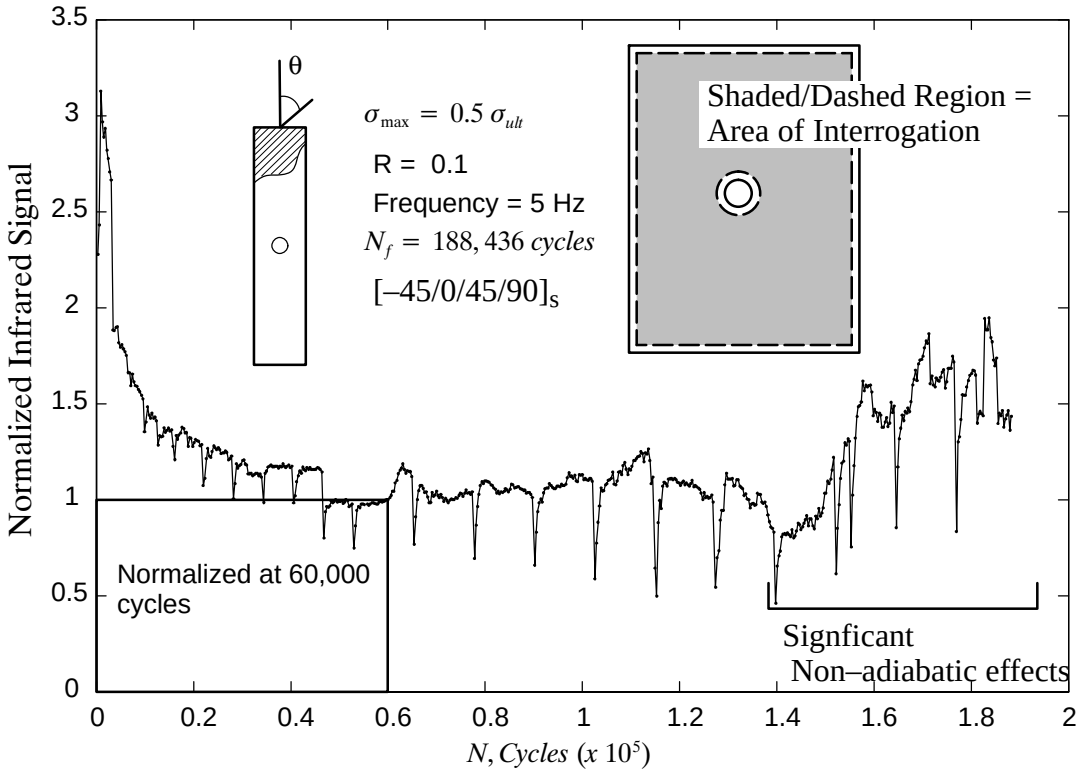

Figure 4.5 Averaged overall TSA response of the notched laminate

To represent the effects of delaminations and matrix cracking in the surface ply other metrics may be applied to the TSA data. In addition to overall average measures of the TSA response, the spatial data can be reduced by measurements of areas of the TSA contour with specified threshold or within critical ranges. Figure 4.6 shows a schematic representation of how the TSA contour is measured and is evolved/increased based on load levels and fatigue cycles.

Specifically a threshold is defined for a measured TSA value of 5,000 camera units, and the number of pixels below this threshold is taken to define the area which will be used as a metric for damage. The proposed TSA data for the sample is 1 inch above and below the notch were used for this calculation for better comparison with stiffness data measurements.

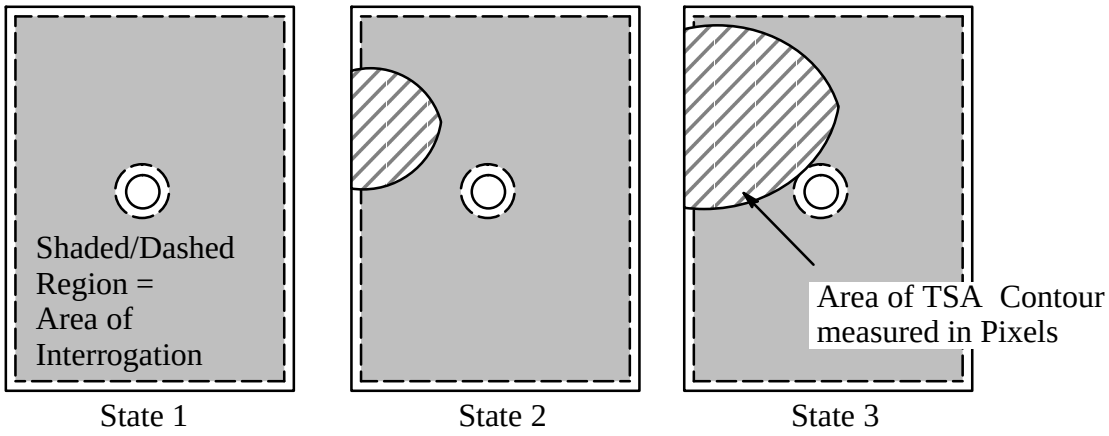

Figure 4.6 Schematic drawing showing growth of TSA contour and method of contour area calculations

Figure 4.7 shows the effect of reducing the data by the contour area calculation. This measure is accurate until 60,000 cycles when the signal becomes relatively erratic. Before 60,000 cycles this data can be related to stiffness, and it can be helpful in describing the spatial effect of damage in the notched laminate. Again, the various spikes in the area calculation during the test shown in Figure 4.7 are due to stopping the fatigue loading to measure the stiffness with the extensometer.

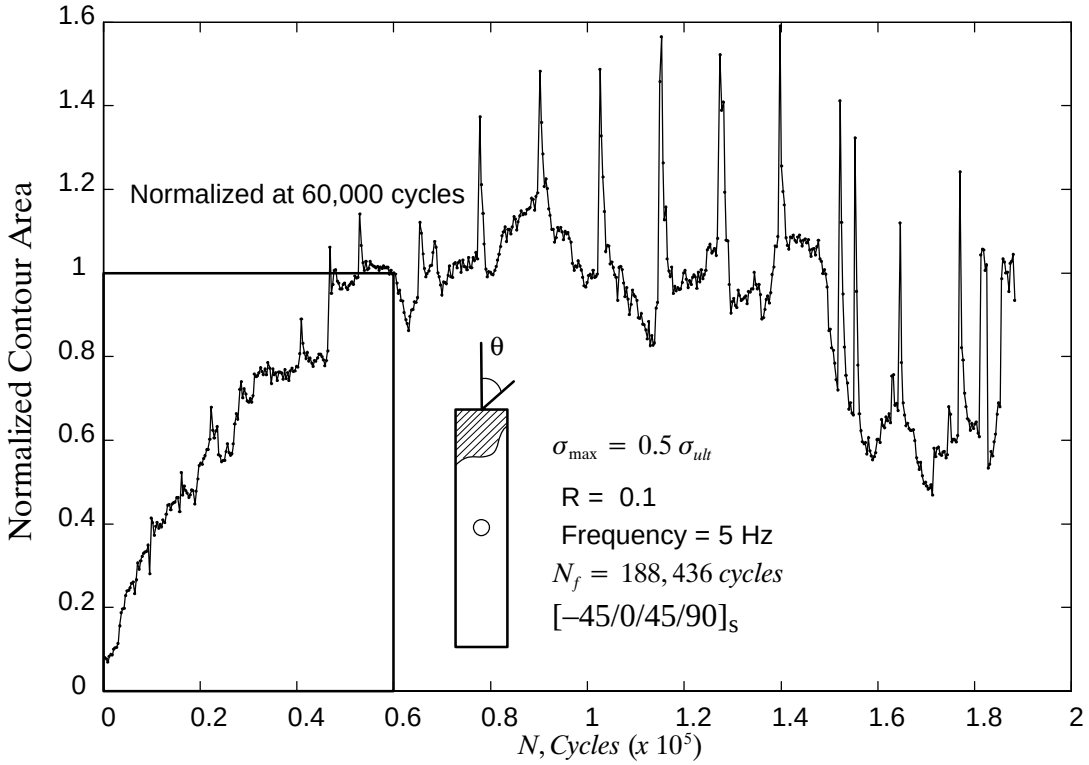

Figure 4.7 Growth of TSA contour area

The area of the TSA contour before each measure of stiffness is linearly related to the following stiffness measure in the test as shown in figure 4.8. This shows the effectiveness of TSA as a measure of in–situ fatigue damage progression. The proposed TSA metric for fatigue shows promise and can be used in the future to construct fatigue S–N curves.

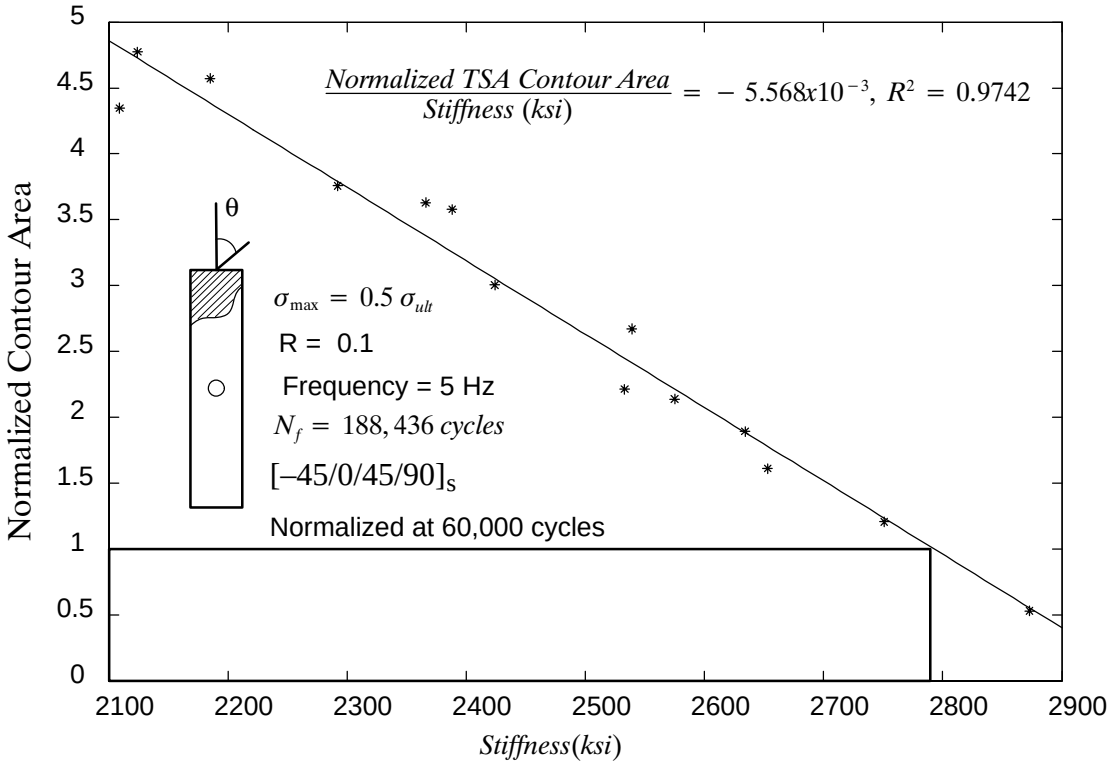

Figure 4.8 Normalized contour area vs notched specimen stiffness

4.4. Experiments with Thick–section E–glass/Epoxy

Thick–section composites, made by the pultrusion process, are generally greater than 6.4 mm (0.25 in). These heterogeneous material systems may combine different reinforcements repeated through the thickness of the member, such as roving, continuous filament mats (CFM), woven fabrics, and braided preforms. Common pultruded composites have roving layers as the primary reinforcement. The CFM layer consists of relatively long and swirled filaments that are randomly dispersed in the plane of the layer. The CFM layers are usually used for multi–directional reinforcement. Weight and corrosion resistance are some properties that make pultruded composites the material of choice in a variety of structural applications. Pultruded composites are manufactured in various shapes e.g. I–shapes, angles, tubes etc. The overall

average fiber volume fraction (FVF) in the thick–section composites used in this study was 0.34. The effective material properties of the entire FRP composite sections are shown in Table 4.2

Table 4.2 Effective properties (Haj–Ali and El–Hajjar, 2003)

Unit	E_{11}	E_{22}	G_{12}	v_{12}
GPa (Msi)	17.1 (2.484)	9.96 (1.444)	3.5 (0.507)	0.283

The Figure 4.9 shows the geometry of the fatigue specimen. Two FRP specimens will be presented in this study: SP–1 and SP–2. The FRP specimens were fatigued by loading in tension–tension mode at a frequency of 10 Hz using an MTS 810. The tests include an R ratio of 0.5 and a maximum stress of 108 MPa (15.6 ksi). For specimen SP–1, the specimen was unloaded every 18,000 cycles to measure the axial stiffness using an extensometer with a gage length of 51 mm (2 in).

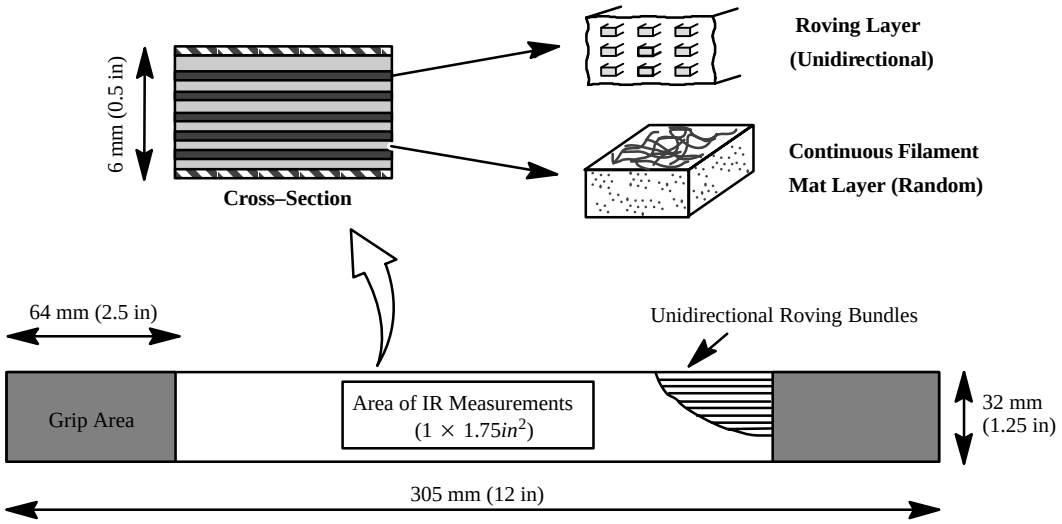

Figure 4.9 Coupon geometry of composite material used in damage characterization fatigu test

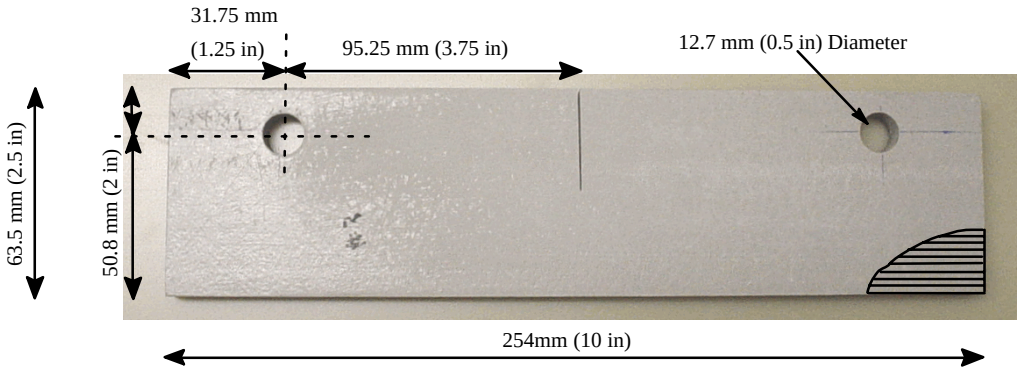

Figure 4.10 Geometry of tested ESE(T) fracture specimen

As shown in Figure 4.10, a pultruded eccentrically loaded single–edge–notch tension, ESE(T), specimen was fatigue loaded in a tension–tension mode at a frequency of 3 Hz with an R ratio of 0.5 and a maximum load of 5.3 MN (1.2 kips). Because the specimen is soft the MTS 810 machine was only able to apply a R ratio of 0.67 and a maximum load of 5.3 MN (1.2 kips) at a frequency of 3Hz. The design for the ESE(T) specimen was specified in ASTM standard (E 1922). The normalized notched size was a/W= 0.5. The ESE(T) experiment provides a means of tracking changes in stress contours and fatigue damage until ultimate failure in the area of the IR measurements during fatigue.

4.5. Results of Fatigue Testing with Thick–Section E–glass/Epoxy

The ultimate mode of failure in specimen, SP–1 is a delamination between the layers of the thick composite. This can be attributed by the gradual softening of the interface between the CFM and unidirectional roving layers and can thus explain why the extensometer was not able to detect a noticeable change in stiffness. Figure 4.11 shows the results of using an extensometer to measure the variation in the axial stiffness in a thick–section FRP composite. There is a difficulty in applying stochastic techinques because data does not have an always increasing/decreasing relationship before failure. There is little indication with traditional tools of fatigue damage progression in FRP composites in tension–tension type testing.

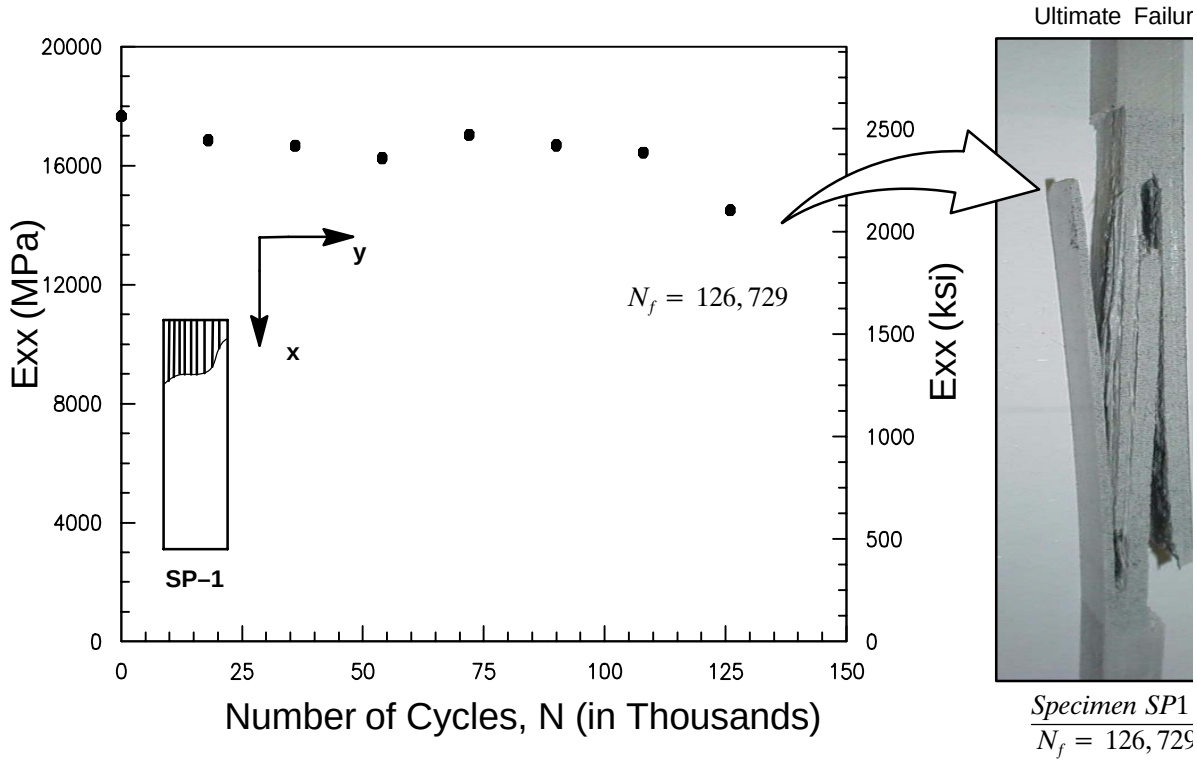

Figure 4.11 Axial stiffness variation during a fatigue test using an extensometer

This lack of fatigue damage indication provides a motivation to develop tools that provide some indication of damage before failure. TSA provides a full–field response where localizations and stress concentrations can be analyzed. The response can be thought of as a large number of strain measures. Instead of using axial stiffness as a measured by an extensometer to to calibrate stochastic models, spatial stochastic parameters using TSA may provide a better description that is more sensitive to the fatigue damage process. Figure 4.12 below shows the average TSA response during fatigue for the selected specimen. The data has been normalized with respect to the TSA Signal at 100k cycles to show that a similar relationship with TSA versus the number of cycles is observed for SP–1 and SP–2.

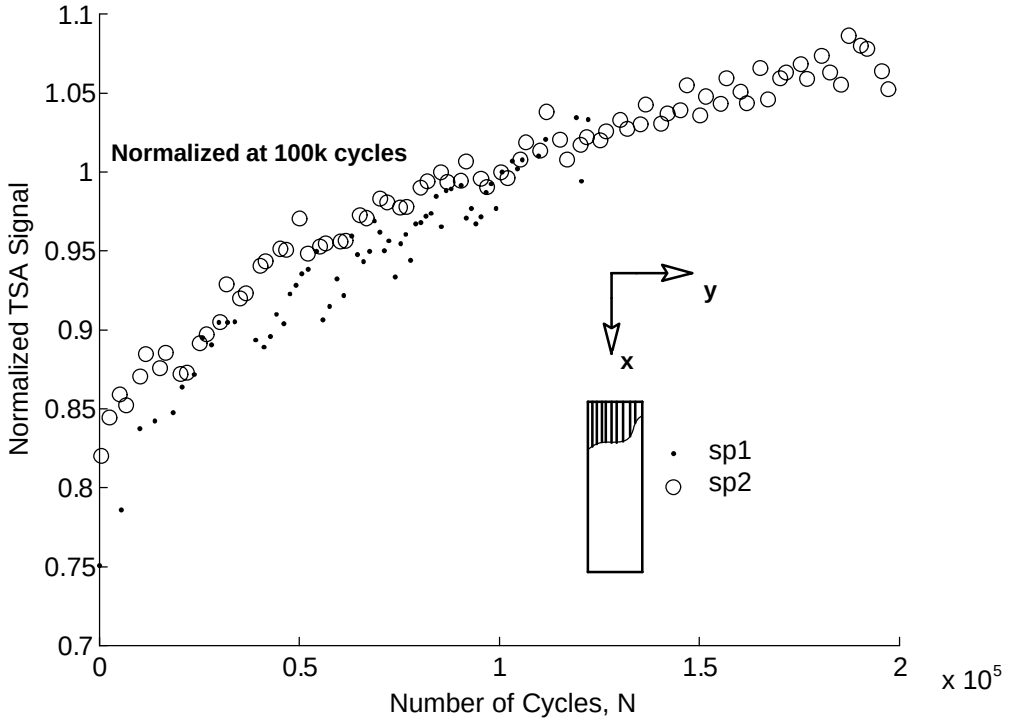

Figure 4.12 TSA area interrogation of pultruded specimen subject to fatigue

The evolution of damage though fatigue life for the two specimens is expected to be very different given the distribution of the initial TSA signal data. In specimen SP–1 and SP–2 the trend of increasing mean and standard deviation over the fatigue life continues throughout the experiment. Figure 4.13 illustrates the variation of the TSA signal in the area that was measured during the fatigue tests. Assuming that the distribution of the TSA signal is normal, an arbitrarily chosen conditional probability was used to set the threshold from the first distribution (TSA values < 99.9 %). This provides a way of tracking areas of higher strain on the surface of the specimen, and relating this distribution of strain across different specimens. Values of high relative strain were plotted in their respective pixel locations to show how the strain distribution progresses though the fatigue life of SP–1 and SP–2.

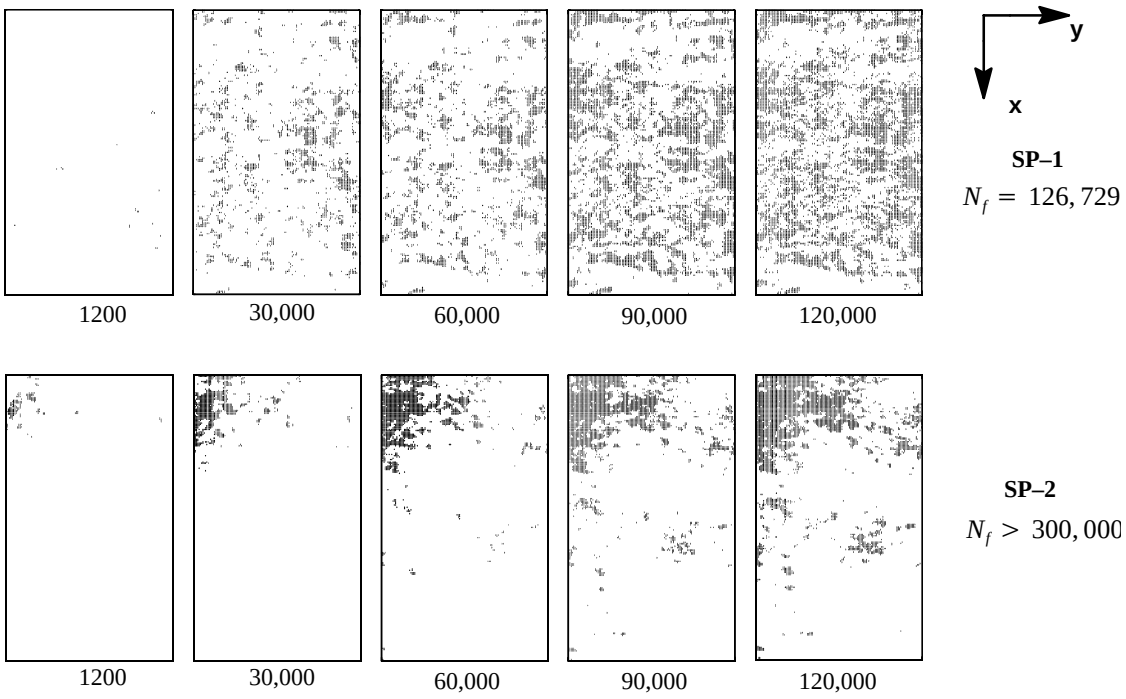

Figure 4.13 Fatigue damage evolution of TSA response in FRP specimens

One might expect a difference in the distribution of strain in a specimen that fails at 126,000 cycles, as seen in SP–1, to be different from one that fails at more than 300,000 cycles, as seen in SP–2. The distribution of strain in SP–1 appears to be homogenously distributed throughout the specimen. This homogenous distribution may be due to a more uniform damage in contrast to the more localized areas of relative high strain in SP–2. The distribution of strain in SP–2 appears to be concentrated in the upper left corner of the specimen with relatively lower signals in the lower area of interrogation.

The unidirectional roving remains the primary load resisting system throughout the test. The out–of–phase response measured (or the TSA response at 90 degree relative to the applied load) was found to be around 6 % of the in–phase response. It is uncertain whether this response can be correlated directly to damage in the FRP specimen. A statistical approach was utilized on the in–phase TSA response to measure the damage during the fatigue tests. A specific area in the

gage section, see Figure 4.9 was interrogated. The TSA signal in this area was plotted on normal probability papers to determine if the distribution is appropriately described as a Gaussian distribution as shown in Figure 4.14 A subset of the sample data is found to be Gaussian as seen by the linear trend when plotted on normal probability paper. The distribution of the TSA signal is assumed to be normal. The mean and standard deviation increased over the fatigue life of the specimen until failure.

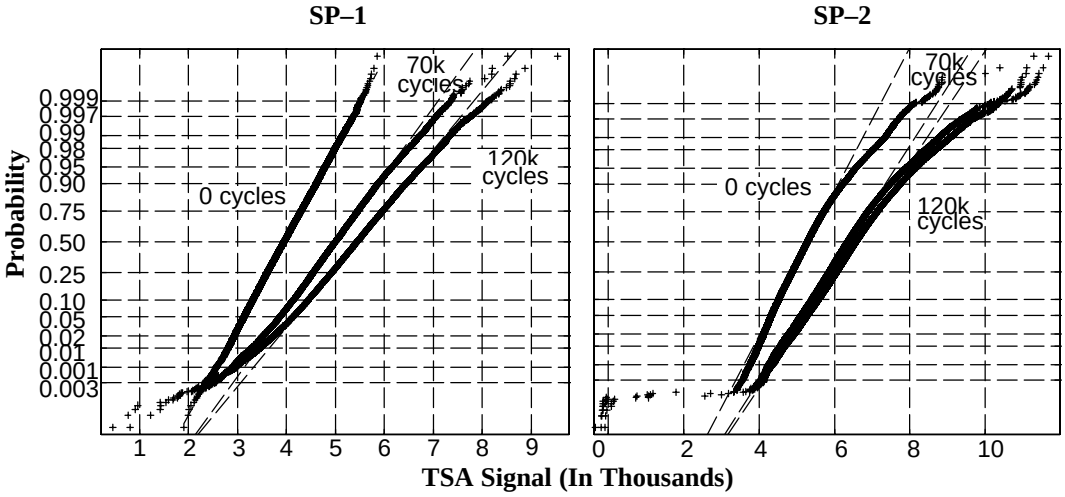

Figure 4.14 Normal probability plots of TSA signal during fatigue

The increasing mean and standard deviation correspond to the distribution of data shifting to the right and decreasing in slope (Figure 4.14). In specimen SP–1 the distribution of the TSA signal at 0 cycles yields a normal distribution with little variance from the theoretical gausian distribution. This may result from the material exhibiting random and homogenous distribution of strain and damage across the surface of the specimen. At 70,000 and 120,000 cycles, the distribution of the TSA signal may still be described by a normal distribution, but deviation from a gaussian distribution is pronounced. The mean of the distribution continues to provide a good description of the overall condition of the specimen thoughout the experiment. Tracking areas that deviate from the theoretical normal distribution may provide a means of locating damage or areas adjacent to damage in the specimen. The TSA signal data for SP–2 can also be described

by a normal distribution; however, deviation from a gaussian distribution is seen immediately in the experiment. The initial deviation may correspond to a localized area of high strain indicating an area of damage or an area adjacent to damage on the surface of the specimen.

Figure 4.15 shows the distribution of the in–phase TSA signal in the area around the crack tip of the pultruded thick–section eccentrically loaded single–edge–notched (Tension), ESE(T), specimen. The contours shown indicate the normal stresses and stress intensities in the material. Areas beyond the crack tip indicate zones of tension. A small but increasing compression zone is observed behind the crack tip as the crack grows due to fatigue. The bright contours that develop behind the crack tip and at the edge of the sample are compression zones resulting from bending (sample edge) or pounding of the crack faces during the fatigue test. This can be seen clearly at the 40K cycle in Figure 4.16 The location of the crack tip and changes in the stress contours in the pultruded specimen can be tracked as the material is damaged until failure. The specimen in Figure 4.16 failed at 40,859 cycles. Future work may include a quantitative description of the ESE(T) fatigue experiment.

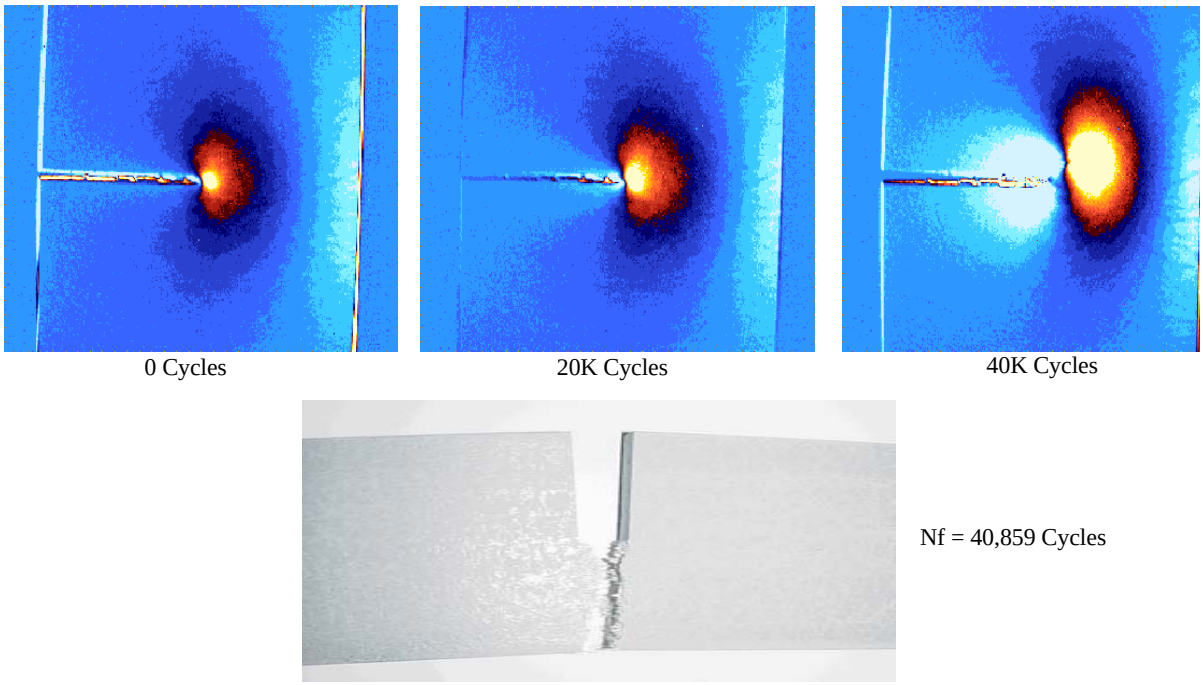

Figure 4.15 IR–image of fatigue damage propagation and tested pultruded ESE(T) specime

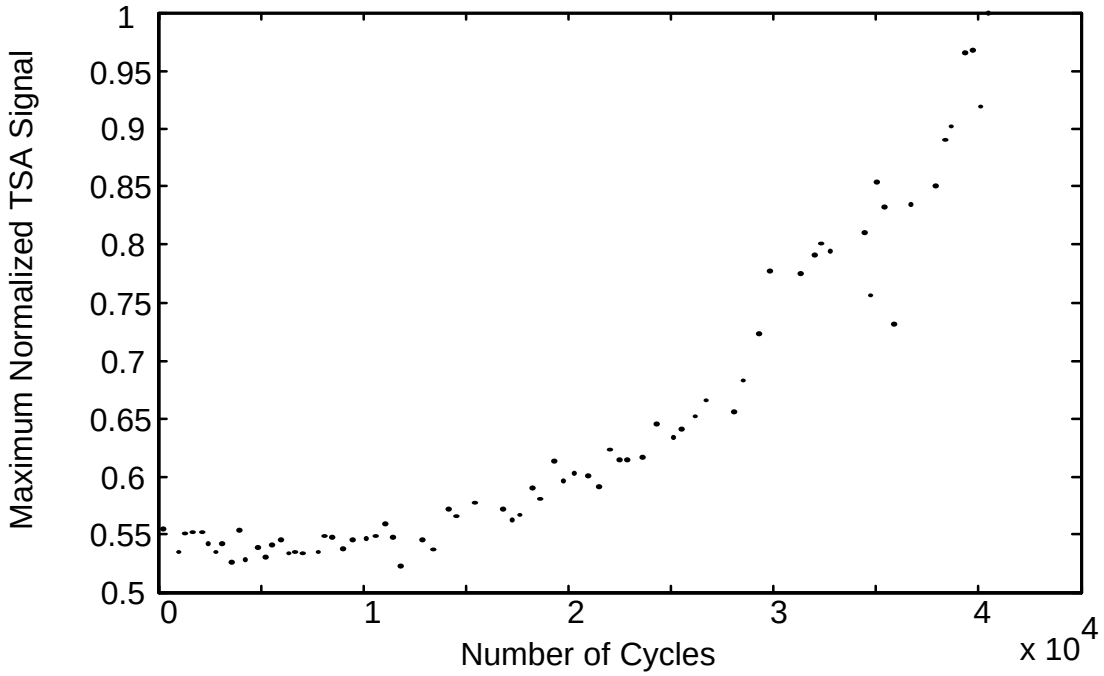

Figure 4.16 Crack tip signal versus number of cycles for a pultdued FRP composite

4.6. Conclusions

This study shows that a proposed full–field IR–TSA technique can be used to detect fatigue damage. Matrix cracking and delamination of surface layers are detected and quantitatively measured. Measures of the TSA signal can be related to the stiffness degredation in notched S2–glass/epoxy laminates during a portion of the fatigue life.

The effect of internal degradation of the material can be reflected in the observed test results. Future work is needed to develop a fatigue failure theory that incorporates the IR measurement of degradation.

CHAPTER 5

INFRARED THERMOGRAPHY FOR FAILURE INITIATION AND PROGRESSION IN COMPOSITE LAP SHEAR JOINTS

5.1 Introduction

This chapter presents an experimental technique using infrared (IR) thermography to characterize the damage initiation and progression in composite lap shear joints. Infrared thermography was used to detect expressions of damage initiation at the surface or the edge of the joint areas. Tests were also conducted with side and direct view IR measurements illustrating the crack tip location and progression with increasing applied mean load. Acoustic emission (AE) was used with the IR measurements in order to quantify events of energy release, give guidance to the consistency of the tests, and allow linking the IR measurements to AE events for quantitative and repeated damage tests. Several samples were removed from loading after initial cracking was detected and underwent micrographic inspection to characterize the nature of the failure initiation. Two composite lap joint systems were tested. The first consists of woven fabric substrates and the second of uni–tape substrates, both using quasi–isotropic carbon reinforcement. The resin layer used for the bonded lap–joints was FM300K adhesive with an approximate thickness of 10 mils. The IR testing schemes are reported and results indicate a good ability to detect expressions of damage initiation in the glue lines near the edge area. Moreover, the location of the crack tip and free surface was also detected as loading progressed. The IR test method was coupled with cyclic applied load and different increasing mean loads. The demonstrated ability of the proposed testing approaches to detect initiation and progression of these lap tests is well suited for future long–term fatigue tests.

5.2 Experimental Procedure

Infrared thermography provides a means of measuring temperature changes on the surface due to applied cyclic loading. In this paper, two composite lap joint systems were tested. The

two joint types include long and short bond geometries made of carbon–reinforced woven fabric and quasi–isotropic uni–tape laminated parts. The overall goal is to characterize damage evolution with an emphasis on detecting failure initiation. Progression of damage is linked to spatial temperature changes in composite single lap shear joints which prompt the use of an IR–TSA technique in combination with Acoustic Emission and clip gauges. The IR–TSA technique shows promise as a refinement over the other testing techniques used in detecting failure initiation and progression in composite single lap shear joints.

The motivation of focusing the IR testing for initiation on the bond line can be explained through the stress analysis of a typical lap joint. We performed FE analysis of a typical lap joint (Figure 5.1) to show that the majority of the shear stress in a single lap shear joint is confined to a relatively small region near the bond line (Figure 5.2) while the interior bond area is relatively unloaded.

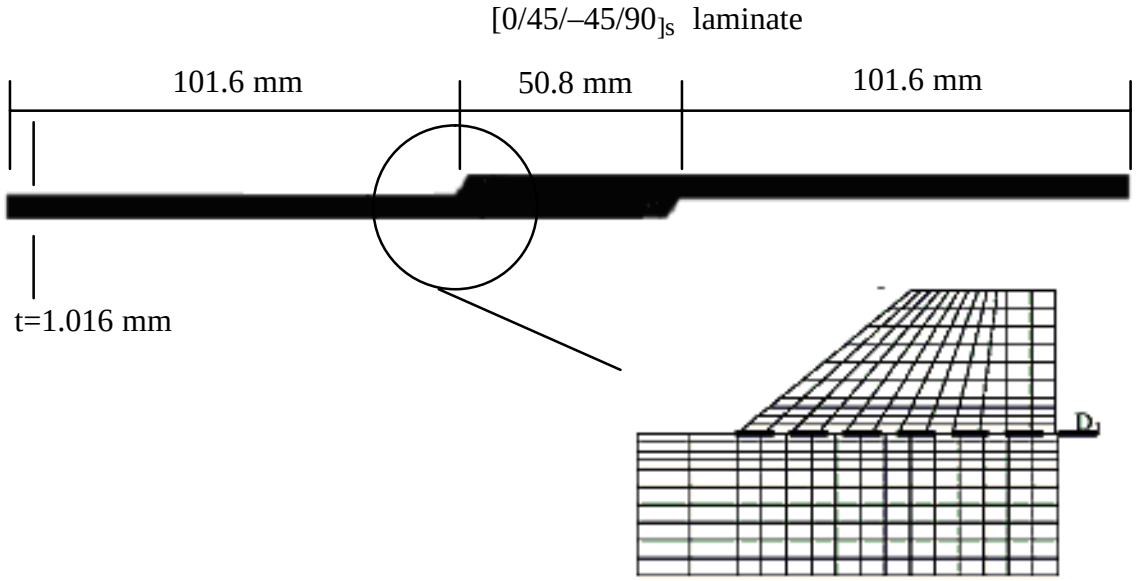

Figure 5.1 Typical geometry and FEM model of a single lap joint

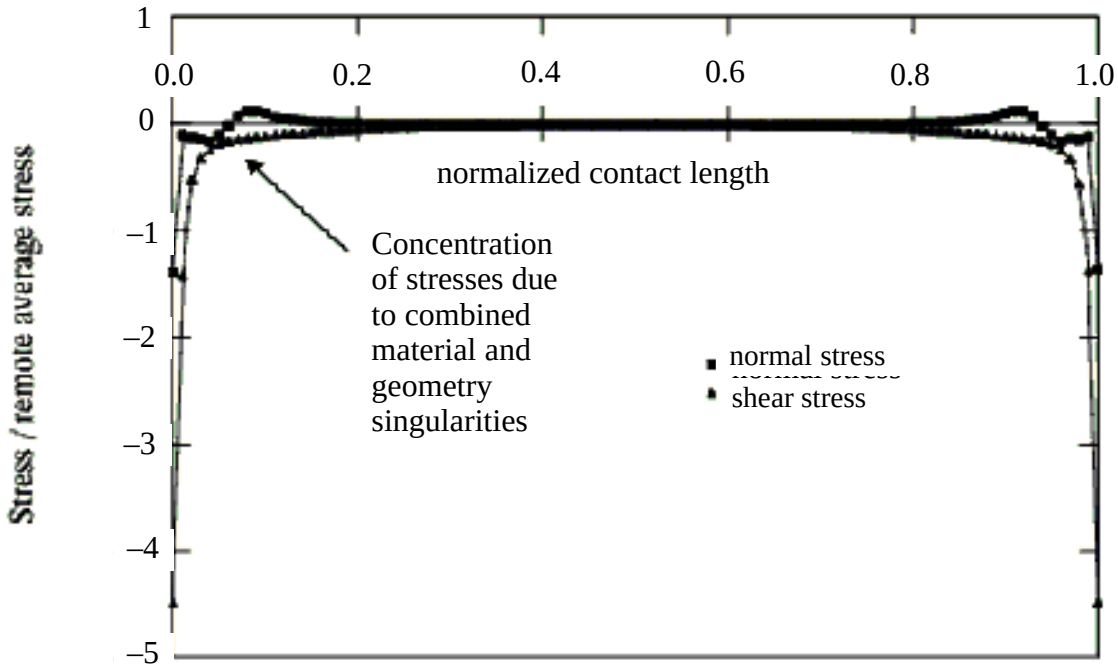

Figure 5.2 Normal and shear stress for the bonded interface in a typical single lap joint

Two IR–Thermography testing methods, termed Method–A and Method–B were applied in this experiment to detect initiation characteristics of lap shear joints. Four main specimens were used with different joint geometry (short/long) and reinforcement materials (uni–tape/woven fabric). Figure 5.3 schematically illustrates these methods. In Method–A, the load is applied monotonically and paused at select levels for short durations. During this time, a small cyclic incremental load is applied and coupled with the IR–TSA measurements (Figure 5.3). In Method–B, once the applied load has reached a desired level the loading is reversed to a small mean load for a short duration, in which a cyclic load is applied to be coupled with the IR–TSA measurement. The process continued on with increasing load magnitudes and applied cyclic loading can be repeated until ultimate failure is reached. In this study Method–A was primarily used for damage progression while Method–B was used to detect initiation. It should be mentioned that the latter method is time consuming and is hard to automate due to the need to process each result to determine that initiation has occurred. Acoustic emission and other

responses are monitored during both types of tests. However, the advantage of Method–B lies in its ability to detect damage at an unloaded state, and the method prevents additional damage to the joint due to the added cyclic loading. In addition, Method–B allows additional testing, e.g. CT–scans, x–ray, and photo–microscope tests. Failure initiation was defined in this experiment as a stress drop at points on the external edge of the bond.

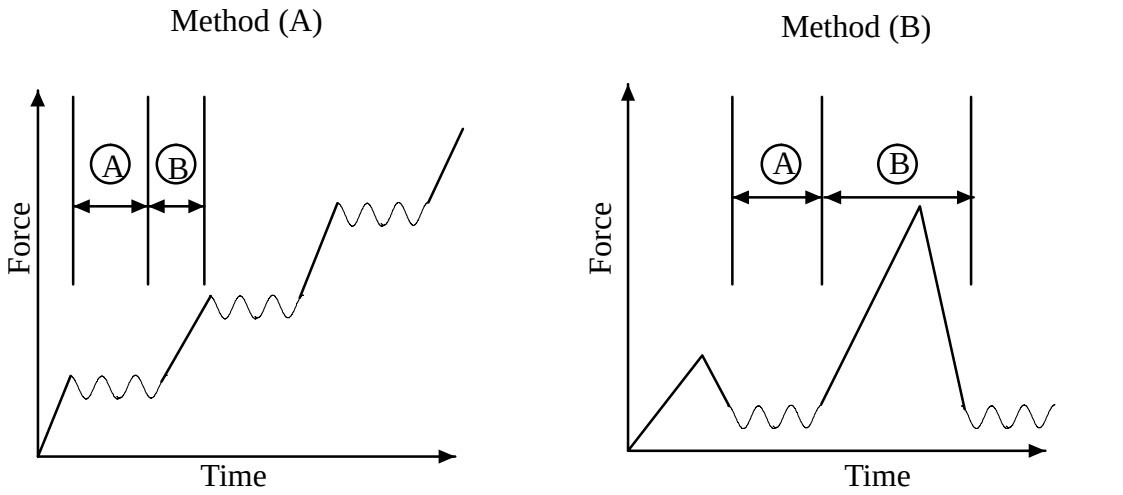

A: Cyclic load was applied in this region for taking IR–images
B: Increments of mean loads were applied statically

A: Cyclic load was applied in this region for taking IR–images
B: Static load and unloading was first applied at different load levels.

Figure 5.3 IR–Thermography load sequences and application of Thermoelastic Stress Analysis

Specimens loaded by Method–B were loaded up to failure using a specially mounted clip gages to detect the change in stiffness while loading and correlating it with the measured AE. In another series of tests AE and clip gauges are applied to the four specimen types, and the specimens are loaded to failure. The clip gauge and acoustic emission results are later correlated to prepare loading increments for Methods A and B. In all testing cases AE was not used to triangulate the location of acoustic events, but it was used to detect damage initiation. The acoustic events are related in most cases to damage occurring in the external bond line of the

single lap shear joint. Figure 5.4 below shows how the clip gauge was mounted to the single lap shear joint to detect displacement in the connection. Figure 5.5 shows a specimen with an AE transducer. Initiation can be defined with acoustic emission as a state described by a saturation of acoustic events as the lap joints approach the ultimate load.

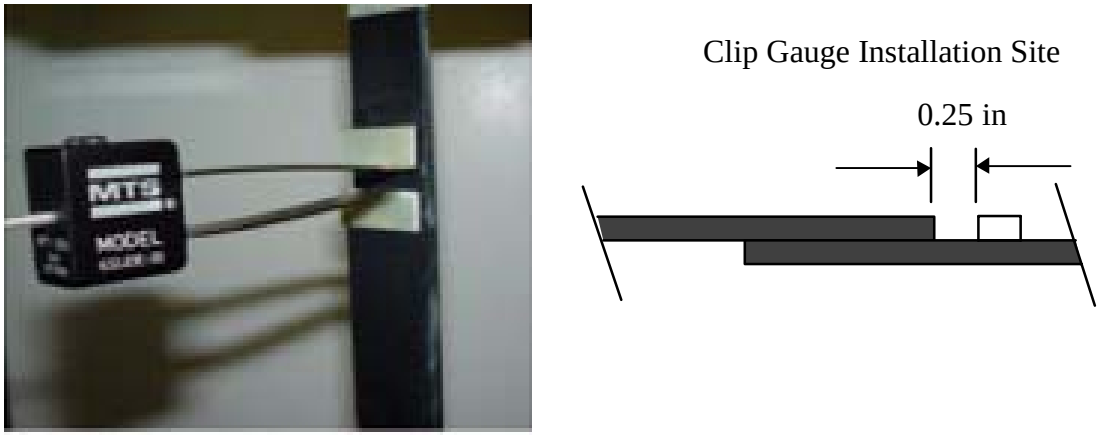

Figure 5.4 Clip gauge application showing the location of the clip gauge and testing configuration

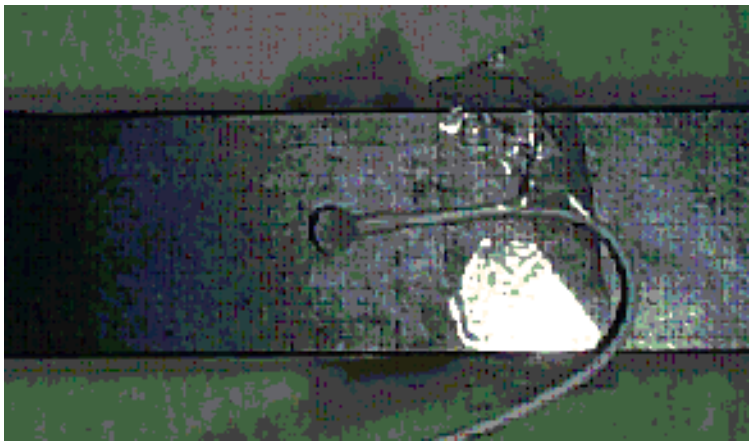

Figure 5.5 Acoustic Emission transducer applied at the edge of the bond line in the single lap shear joint on the backside of the specimen

Specimen Preparation and Test Setup

A DeltaTherm DT1500 thermoelasticity measurement system was used to acquire the thermal measurements. The DeltaTherm's infrared array detector synchronized with the applied

cyclical loading enables the detection of the transient thermoelastic effect. The infrared detector acts as a transducer, which converts the incident radiant energy into electrical signals. A lock–in analyzer (a signal–processing unit) extracts the thermoelastic information from the detector's output signal by using the reference signal from the loading device. The TSA–IR system uses the reference signal to reject any non–stress related thermal emissions. The frequency should be high enough to prevent heat transfer due to stress gradients during the load cycle. The Delta–Therm has a thermal resolution of at least 1 mK for image exposure times of one minute or less. Figure 5.6 shows the testing setup along with a schematic of the TSA data acquisition. The IR camera captures images at rates of more than 400 frames per second. The applied load signal is used to integrate synchronized TSA images that correspond to peak values of loading. The integration of the captured images is a temporal smoothing process performed over a specified period. In this study, a period of 1–2 min was used. The cyclic load was applied using an MTS 810 servo–hydraulic test system with a 22.2 kN(50 kip) capacity. The accuracy of the recorded strains is within 50 microstrain and the load is within 0.22 kN (50lb).

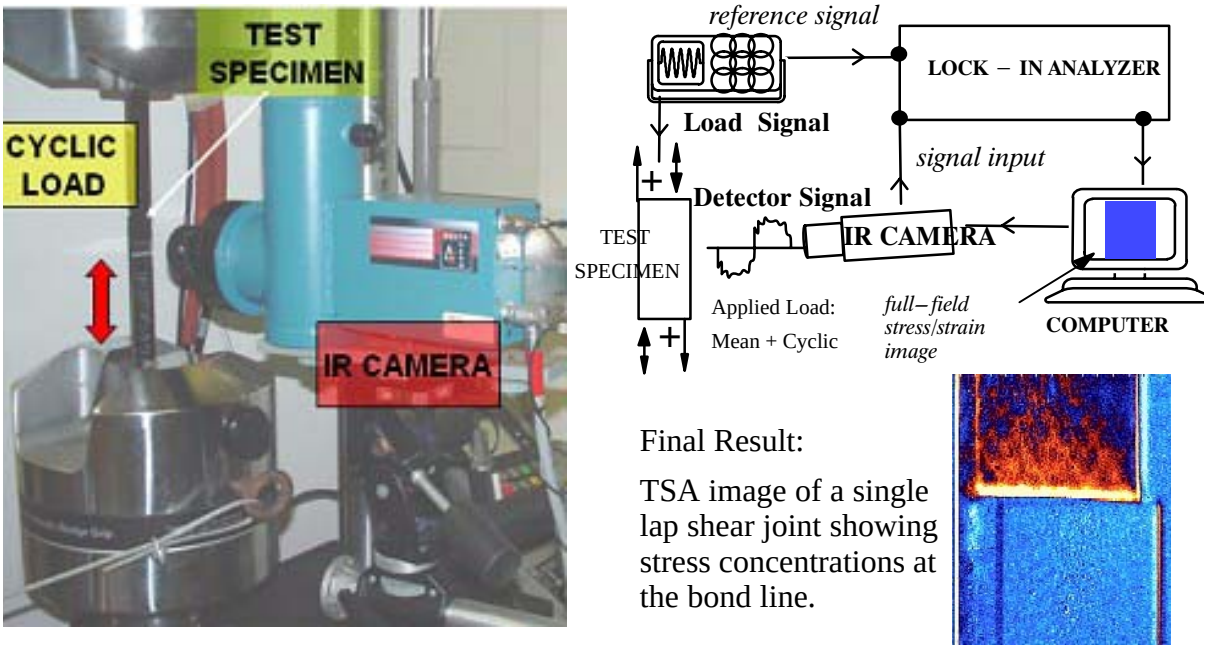

Figure 5.6 Thermoelastic testing set–up

5.3 Results Summary and Discussion

Select results are given in this section to illustrate the proposed IR–TSA method for damage in composite lap joints. Additional complementary results from AE and mechanical responses are also included. Note that in both methods A and B, initiation is defined as a distinct difference in the stress concentration at the joint bond lines. A series of specimens was tested using both Methods. Figure 5.7 shows the measured TSA response to test Method–A with a woven long bond lap shear joint. Notice that the continuous stress concentration in the external bond line present at a mean load of 200 lb (Figure 5.7a) is not present at 4,400 lb (Figure 5.7e). Discontinuities in this continuous stress concentration are present in the woven long bond specimen as early as 1750 lb (Figure 5.7b).

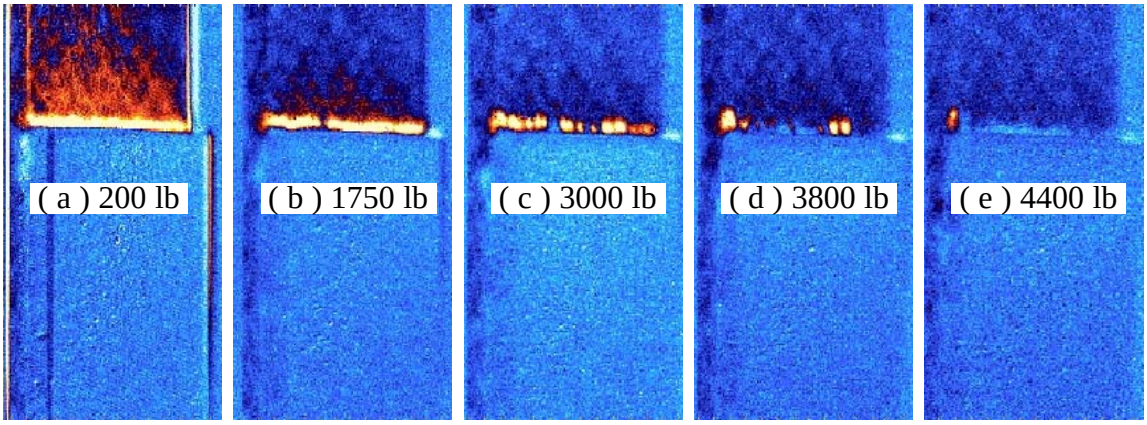

Figure 5.7 Woven long bond single lap shear joint tested with Method–A, ultimate failure occurs immediately following the 4,450 lb load level.

Figures 5.8 and 5.9 show results using Method–B for short bond lap joints made from fabric and uni–tape laminates. Notice the stress concentration seen at the previous bond line (Figure 5.8a) is not always continuous due to differences in the manufacturing and joint finish at the bond line. An attempt was made in each specimen to reach a condition of a discontinuous bond line in order to establish damage initiation well within the joint area and not limited only to bond line, e.g. Fig. 5.8c.

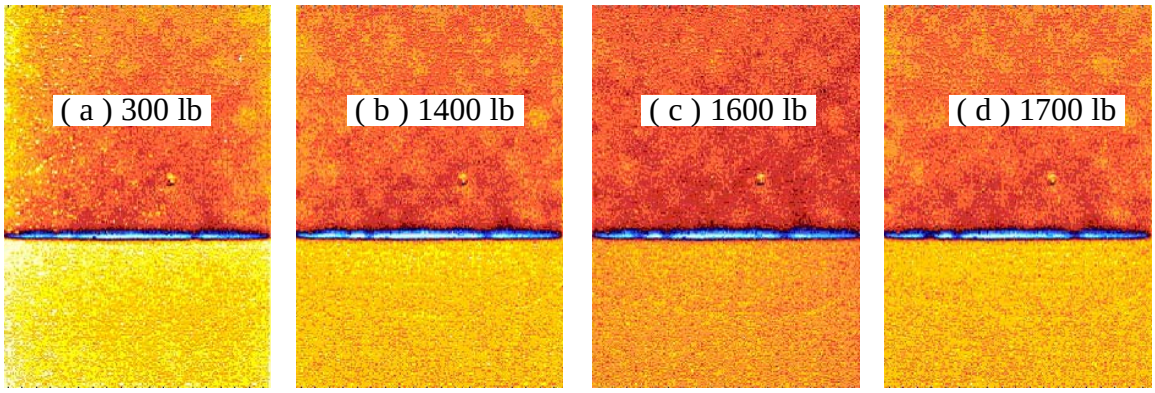

Figure 5.8 Fabric short bond single lap shear joint tested with procedure B preserved after a maximum load level of 1700lb. Noticeable changes in the bond line IR measurement from (c) to (d).

Figure 5.9 below demonstrates the difference between the response of the fabric short bond specimen and the uni–tape short bond specimen. The uni–tape short bond specimens emit relatively very little acoustic or thermal responses due to mechanical loading compared to the woven joint types. Figure 5.9 shows how different failure initiation stages were captured utilizing IR–TSA.

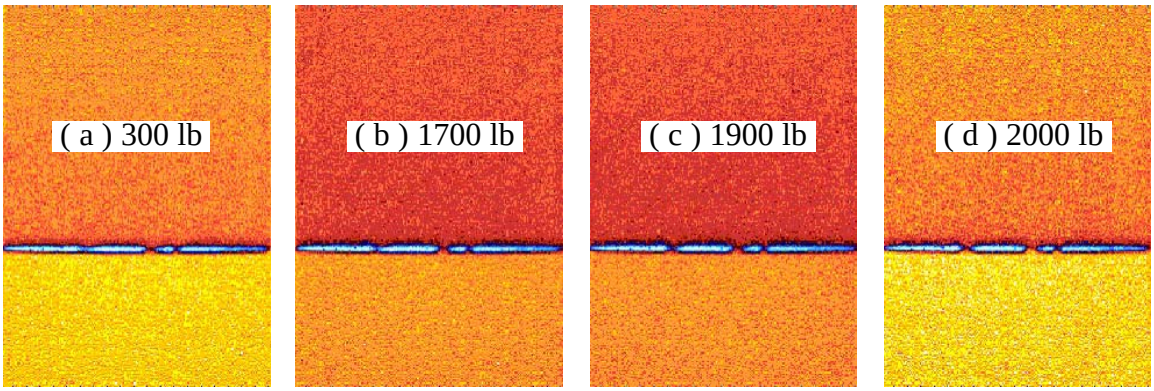

Figure 5.9 Uni–tape short bond single lap shear joint tested with Method–B and preserved after a maximum load level of 2000lb. Increasing changes in bond line IR emission indicating damage progression from (b) to (c) and (c) to (d).

Several specimens were preserved after noticeable bond line damage initiation has occurred and taken for further investigation using destructive sectioning coupled with photo–microscopy. The major assumption is once a noticeable IR–damage detection has occurred in the bond line, damage within the joint area should be visually evident. Specimens were removed from testing prior to ultimate failure once thermography, showed that initial failure may have occurred allowing for marking of the specimens at the locations were the suspected failure initiation occurred. The objective of the failure analysis was to document, if possible, the nature and extent of this initial damage. Prior to sectioning the specimens for micrographic inspection, each specimen was ultrasonically inspected for evidence of macroscopic flaws (e.g. delaminations greater than 1/4" diameter). As expected no evidence of damage could be found at the resolution of the C–scan system used. Each specimen was then sectioned and potted in preparation for micrographic inspection. Potted specimens were ground down to points near the marked initiation flaw points using course grit paper. At this point specimens were polished down to the flaw points while being checked frequently for indications of cracking. In most cases, evidence of micro–cracking was documented at the sites suspected of failure. Several examples of photos taken at 50X and 200 X magnifications are provided. Figure 5.10 through 5.12 shows several photo–microscope images that correlate well with the above assumption and provide a substantial confirmation to the proposed IR damage initiation and progression method.

Figure 5.10 Photograph showing micro–cracking in short bond line uni–tape specimen #5 (50X).

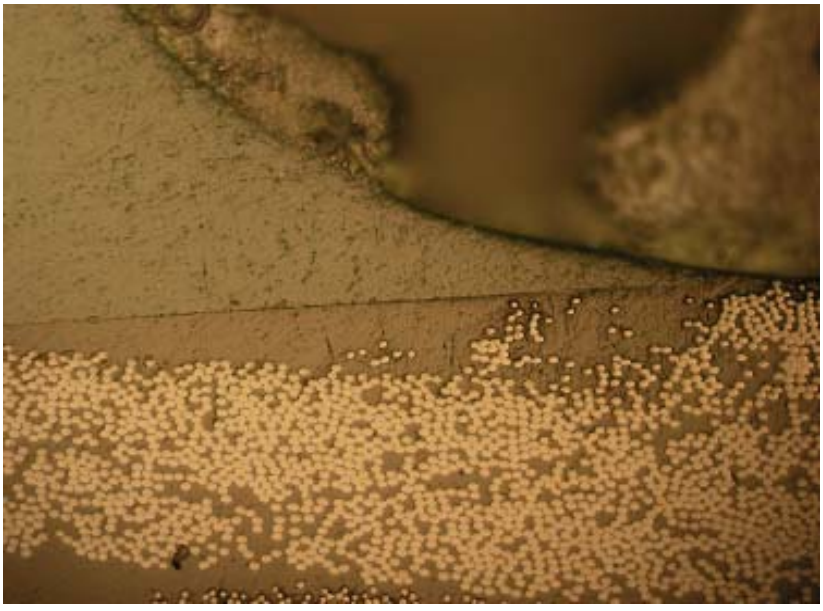

Figure 5.11 Photograph showing disbonding at the adhesive interface in short bond line fabric specimen #4 (200X)

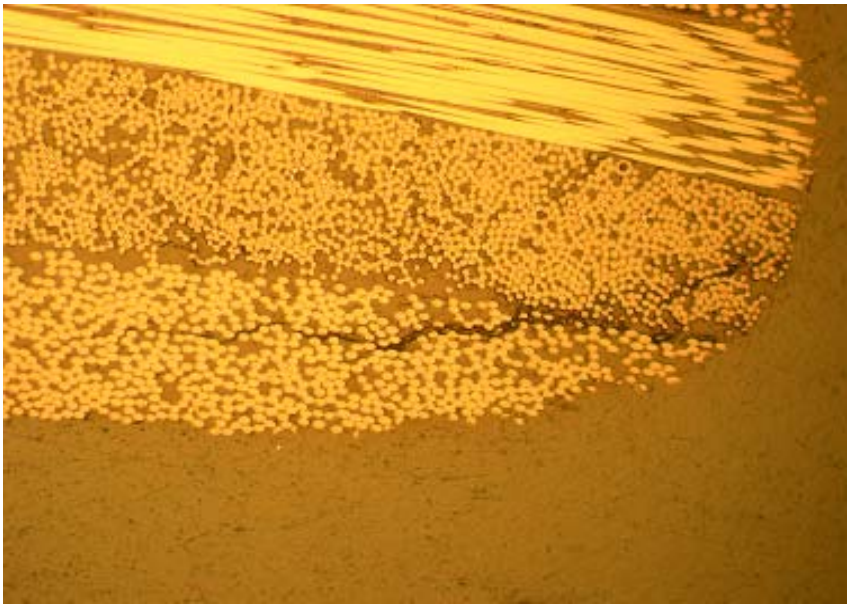

Figure 5.12 Photograph showing micro–cracking in short bond line fabric specimen #1 (200X).

In addition to the results from infrared thermography, it is interesting to show some results from the combined acoustic emission and clip gauges. Figures 5.13, 5.14, 5.15, and 5.16 below show different figures representing AE and clip–gauge opening displacements along with applied loads. The fabric long bond and uni–tape short bond specimens show some events with the clip gauge that can be correlated to acoustic events. The uni–tape short bond specimen shows relatively little acoustic, thermal response, or load/displacement response during loading. The fabric long bond specimen shown in Figure 5.14 emits approximately ten times the number of acoustic events as the uni–tape short bond. In fact, the fabric long bond specimen as well as the uni–tape long bond specimen (Figure 5.13), and the fabric short bond specimen (Figure 5.16) show visible “kinks” in the load vs. displacement curve that correspond to accelerated acoustic events as seen in the load vs. accumulated count of acoustic events. Notice also in Figure 5.13 there are no “kinks” in the load vs. displacement curve for the uni–tape short bond joint.

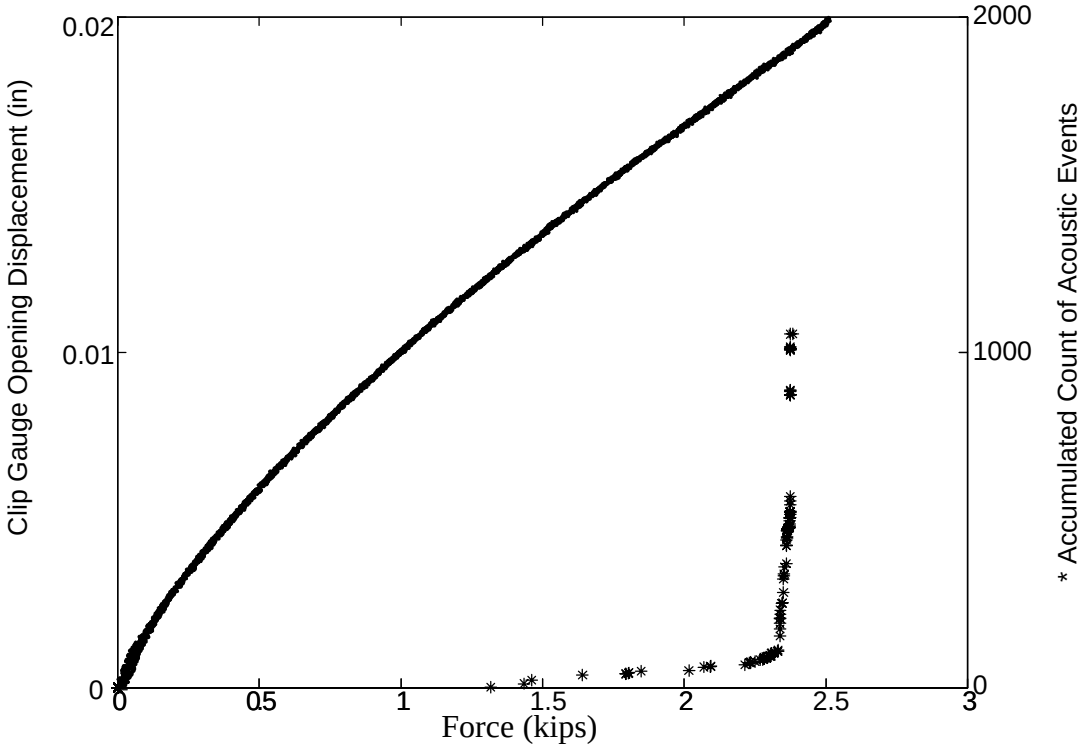

Figure 5.13 Acoustic emission and clip gauge opening displacement as measures of initiation in a uni–tape short bond single lap shear joint

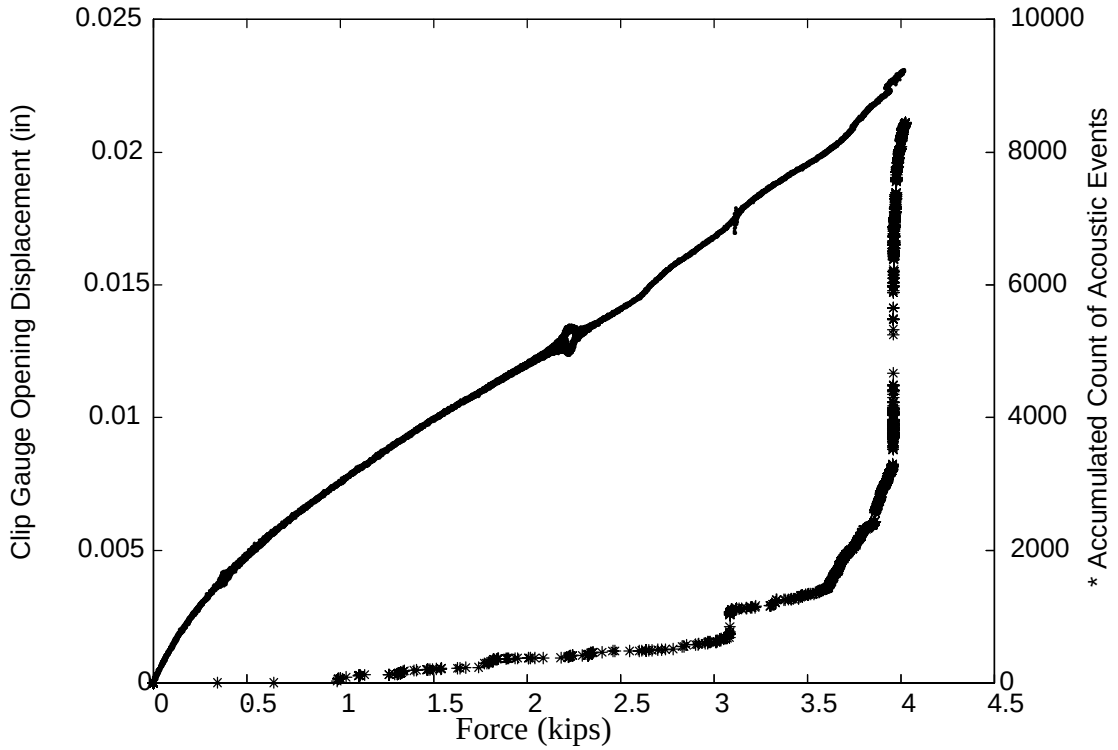

Figure 5.14 Acoustic emission and clip gauge opening displacement as measures of initiation in a woven long bond single lap shear joint

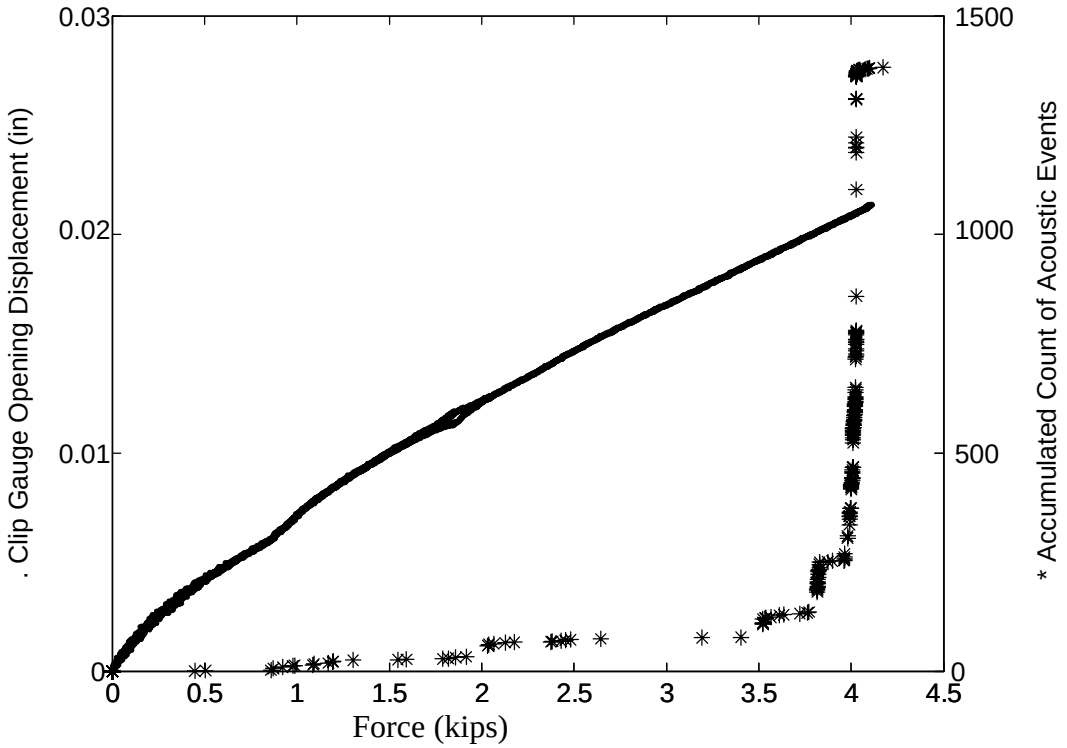

Figure 5.15 Acoustic emission and clip gauge opening displacement as measures of initiation in a uni–tape long bond single lap shear joint

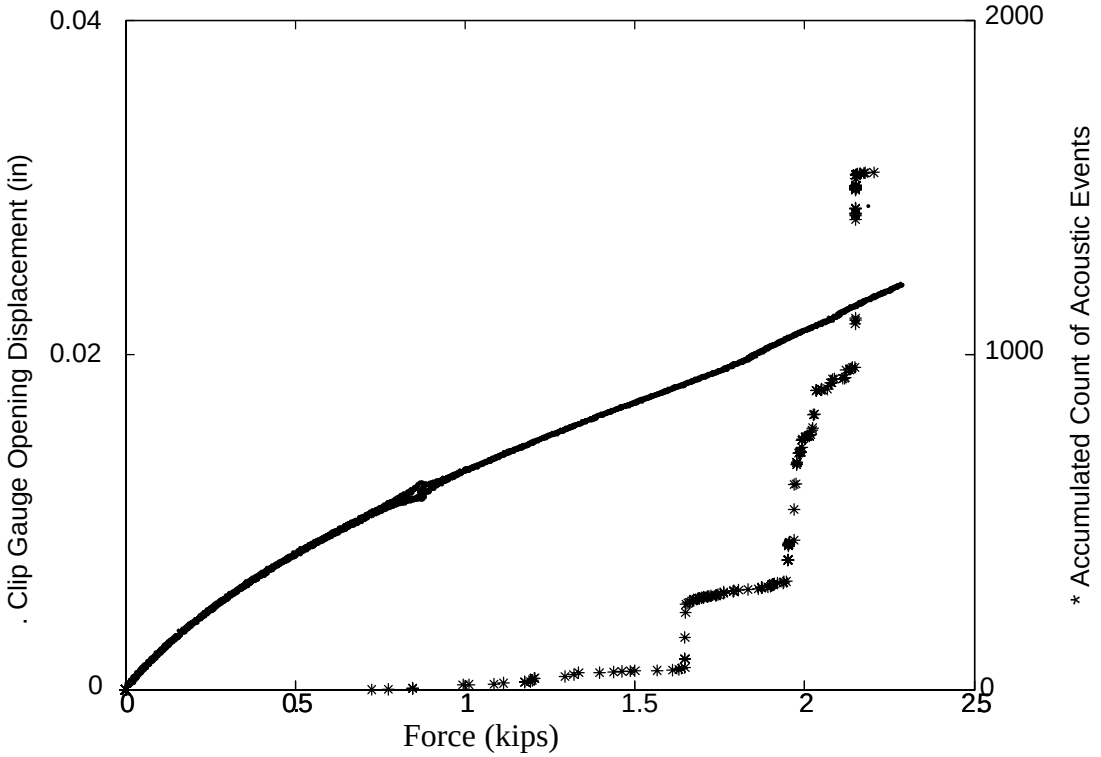

Figure 5.16 Acoustic emission and clip gauge opening displacement as measures of initiation in a woven short bond single lap shear joint

The experimental results using testing Method–B show that the IR–TSA results and AE can be well correlated. The advantage of the IR–TSA is that it provides a full–field map of damage locations. The accumulation of acoustic responses is followed by TSA responses that correlate and verify the changes in the stress concentration at the bond line. This observation correlates well with the finite element results presented earlier showing that the majority of the shear stress in single lap shear joints is confined at or near the bond line (Figure 5.2). The infrared response at the bond line measured utilizing TSA in both Methods A and B show that failure initiation can be defined as the formation of discontinuities in the external bond line of the single lap shear joint. The combination of acoustic emission and TSA provides a wealth of information used for damage detection. Acoustic emission alone provides information on damage and its accumulation up to saturation impending ultimate failure, but infrared thermography provides

a refinement on detecting the damage severity and a visual inspection of the location of damage.

5.4 Conclusions

The study of this section presented an effective new IR–TSA method for detecting damage initiation and progression in single–lap composite joints. The proposed full–field method was correlated with AE and mechanical load–deformation measurements. Select results were presented for long and short bond–area joints as well as fabric versus quasi–isotropic uni–tape laminates. These results show a promising potential to extend the proposed new testing technique to other joint types and composite structural components.

CHAPTER 6

CONCLUSIONS AND FURTHER RESEARCH

A comprehensive study has been conducted on qualitative and quantitative Infrared Thermography and Thermoelastic Stress Analysis methods used with different composite materials and structural systems. A brief summary of major conclusions followed by further research recommendations is presented in this chapter.

6.1 Conclusions

An experimental thermoelastic stress/strain analysis (TSA) technique developed by El–Hajjar and Haj–Ali (2003) was expanded on in this study to measure the sum of the normal surface strains in a variety of FRP composites including Carbon/epoxy, S2–glass/epoxy, and thick–section E–glass/polyester laminates. The new method relates the Thermoelastic signal to the sum of the normal surface strains in FRP composites, and it provides a full–field measurement of the strain invariant that can be used to verify computational models. Chapter 2 provides steps to acquire a thermomechanical calibration constant and verification of a finite element open–hole model. The experimental technique shows excellent correlation with computational models under a multi–axial state of stress.

Fiberboard systems are inspected for hidden damage and defects with thermoelastic stress analysis in Chapter 3. Several general and easily implemented methodologies are presented along with setups, sensitivity enhancement guides, and detection tools provide industry with a toolbox of examples to investigate various product enhancement interests. General setups and methodologies are developed with the intent of saving industry valuable time and capital for the implementation of infrared thermography in a manufacturing environment. Combinations of mechanical and thermal excitation sources have been investigated not only to show the

possibilities of defect detection using infrared thermography, but various setups have also been presented to encourage the use of infrared thermography by providing a helpful guide for what works and what doesn't work with current infrared technologies.

Traditional measurements of stiffness degradation with an extensometer were coupled with in–situ TSA fatigue measurements of a notched S2–glass/epoxy quasi isotropic, and un–notched thick–section E–glass/polyester FRP composites in Chapter 4. Stiffness and area measurements of the S2–glass/epoxy specimen having TSA values below a threshold were correlated, and the results are proportional within a portion of the fatigue life. The stiffness measurements were relatively constant for the duration of the fatigue life of the E–glass/polyester system, but the TSA values in this case increased throughout the fatigue life. The effect of internal degradation of the material can be linked to the observed TSA test results. This showed the effectiveness of TSA as a measure of in–situ fatigue damage progression. Different TSA damage metrics were examined during this study to illustrate their advantage over traditional measurement methods.

An effective new IR–TSA method is presented in Chapter 5 for detecting damage initiation and progression in single–lap composite joints. The proposed full–field method was correlated with AE and mechanical load–deformation measurements. Select results were presented for long and short bond–area joints as well as fabric versus quasi–isotropic uni–tape laminates. These results show a promising potential to extend the proposed new testing technique to other composite lap joint types and composite structural components.

6.2 Further Research

Further research is recommended to expand the use of infrared thermography as a quantitative non–destructive tool in the areas of fracture mechanics and fatigue. Expanding on the research in Chapter 2, further testing is needed to provide insight into the effects of the thickness of the isotropic coating and alternative surface coatings. If an additional isotropic

surface coat is not applied, two calibration constants may be needed to describe the system under a multiaxial state of stress. Also, experimental methods using two calibration constants to eliminate the need for coating is the subject for future research. Determining the extent of the adiabatic conditions and how they relate to geometry, material, and loading conditions is an important aspect for future development.

In fracture mechanics, for example, the experimental technique developed by El–Hajjar and Haj–Ali (2003) couples the relation between the the sum of the normal surface strains and the thermoelastic signal. This relation can be used with numerical methods to determine stress intensity factors (SIFs), KI and KII, under mixed–mode loading conditions. Lekhnitskii's (1963) solution can be implemented with the least square method to investigate notched anisotropic FRP material systems. Traditionally, the thermoelastic data could be directly related to the first stress invariant by calibrating two thermal coefficients, but an isotropic coat can be applied to the surface of the composite system (as shown in Chapter 2) that may increase the accuracy of the method.

Quantitative infrared (IR) thermography can be used to with composites to to describe the fatigue damage process, and the full field data can be reduced to analyze various material and structural systems. For example, infrared thermography can be used to detect expressions of damage initiation at and around a rivet. The temperature changes on the surface of a riveted lap joint caused by damage during fatigue can be tracked, and thermoelastic stress analysis (TSA) technique can be used to relate the surface deformation to the IR emission. Cracking behind the rivet head can be analyzed using the fracture mechanics approach as explained in this section, and the damage evolution can be characterized using the proposed IR–TSA method along with a full–field data reduction approach.

The TSA metrics for fatigue presented in Chapter 4 shows promise and can be used in the future to construct fatigue S–N curves. Also, metrics used in this study and others can describe

the irreversible damage of material due to fatigue or crack growth are valuable for stochastic cumulative damage models. Stochastic methods, such as Markov chain models can be used to fit the evolution of thermographic data measured during the fatigue process.

REFERENCES

ABAQUS, (2002), Hibbitt, Karlsson and Sorensen, Inc., “User’s manual”, Version, 6.3.

Ando, K., and Ohta, Masamitsu. (1999), “Variability of fracture toughness by the crack tip position in an annual ring of coniferous wood.” *Journal of Wood Science*, 45, 275–283.

ASTM D 3039/D 3039M, (2000), “Standard test method for tensile properties of polymer matrix composite materials.”, Annual Book of ASTM standards.

ASTM D 5766/D 5766M–02a, (2002), “Standard test method for Open Hole Tensile Strength of Polymer Matrix Composite Laminates.”, Annual Book of ASTM standards.

Bakis, C. E., and Reifsnider, K. L., (1991), “The adiabatic thermoelastic effect in laminated fiber composites,” Journal of composite materials, vol. 25, pp. 809–830.

Bakis, C. E. Y., H. R., Stinchcomb, W. W., and Reifsnider, K.L. (1989) “Damage Initiation and Growth in Notched Laminates Under Reversed Cyclic Loading.” *Composite Materials: Fatigue and Fracture, Second Volume, ASTM STP 1012*, Philadelphia, 66–83.

Barone, S., and Patterson, E. A., (1998), “Polymer coatings as strain witness in thermoelasticity,” Journal of strain analysis, vol. 33, No 3, pp. 223–232.

Biot, M. A., (1956), “Thermoelasticity and irreversible thermodynamics,” Journal Applied Physics, vol. 27, no. 3, pp. 240–253.

Bremond, P., and Potet, P. (2001) “Lock–In Thermography: A tool to analyse and locate thermo–mechanical mechanisms in materials and structures.” *Proceedings of SPIE*.

Cunningham, P. R., Dulieu–Barton, J. M., Dutton, A. G., and Shenoi, R. A., (2001), “Thermoelastic characterisation of damage around a circular hole in a GRP component,” Key Engineering Materials, vol. 204–205, pp. 453–463.

DeltaTherm Operation Manual, (2001), Stress Photonics Inc. Madison, WI.

Dulieu–Smith, J. M., Quinn, S., Shenoi, R. A., Read, P. J. C. L., and Moy, S. S. J., (1997), “Thermoelastic stress analysis of a GRP tee joint,” Applied Composite Materials, vol. 4, pp. 283–303.

Dunlap, R. W. (1966), *A study of stress measurements using the thermoelastic effect*, Ann Arbor.

Dunn, S. A., (1993), “On the effects of through–thickness thermal conduction on stress measurement by thermoelastic techniques,” Experimental Mechanics, vol. 33 pp. 32–36.

Dunn, S. A., (1992), “Analysis of thermal conduction effects on thermoelastic temperature for composite materials,” Journal of Applied Mechanics, vol. 59, pp. 552–558.

El–Hajjar, R. F., and Haj–Ali, R. M., (2003), “A quantitative thermoelastic stress analysis method for pultruded composites,” Composites Science and Technology, vol. 63, no. 7, pp. 967–978.

El–Hajjar, R. F., and Haj–Ali, R.M. (2003), “Surface Strain Measurement in Pultruded Composites using Infra Red Thermography.” *Tenth International Conference on Composites/Nano Engineering ICCE–10*, New Orleans, LA.

El–Hajjar, R. F. (2004), “Experimental study and analytical modeling of translayer fracture in pultruded FRP composites.” xvi, 173 leaves.

El–Hajjar, R. F., and Haj–Ali, R.M. (2004), “Infrared (IR) Thermography for Strain Analysis in Pultruded Fiber Reinforced Plastics.” *Experimental Techniques, Society for Experimental Mechanics (SEM)*, 28(2).

Haj–Ali, R. M. and El–Hajjar, R. F., (2003), “Crack propagation analysis of Mode–I fracture in pultruded composites using micromechanical constitutive models,” Mechanics of Materials, vol. 35, no. 9, pp. 885–902.

Haj–Ali, R. M., and El–Hajjar, R.F. (2004), “A Thermoelastic Method for Strain Measurement in Coated Orthotropic Materials.” *Experimental Mechanics*.

Haj–Ali, R., M. and, Kilic, H., (2002), “Nonlinear behavior of pultruded FRP composites,” Composites Journal Part B: Engineering. vol. 33, no. 3, pp. 173–191.

Haj–Ali, R. M., Kilic, M., and Zureick, A–H, (2001), “Three–dimensional micromechanics –based constitutive framework for analysis of pultruded composite structures,” ASCE Journal of Engineering Mechanics , vol. 127, no. 7, pp. 653–660.

Horn, G. P., Mackin, T. J. , and Kurath, P. (2002), “Composite Machining Damage Quantification Using Thermoelastic Stress Analysis.” *Polymer Composites*, Vol. 23 No. 2, 193–199.

Johnson, S. and Haj–Ali, R. (2004), “Infrared Thermography for Fatigue Damage Detection in FRP Composites.” *Proceedings of the American Society of Composites*, Atlanta, GA.

Johnson, S., Kim, H., El–Hajjar, R. and Haj–Ali, R. (2004), “An IR Technique for Damage Characterization in Thick–Section Composites.” *Proceedings of the Society for Experimental Mechanics*, Costa Mesa, CA.

Kageyama, K., Ueki, Kiyoshi, and Kikuchi, M. (1989), “Fatigue Damage Analysis of Notched Carbon/Epoxy Laminates by Thermoelastic Emission and Three Dimensional Finite Element Methods.” *Proceedings of the 7th Conference on composite and materials ICCM–7*.

Kelvin, (1878), (Thomson, W.), “On the thermoelastic, thermomagnetic and pyro–electric properties of matter”, Phil. Mag., vol. 5, pp. 4–27.

Kilic, H. and Haj–Ali, R. (2003a), “Elastic–degrading analysis of pultruded composite

structures," Composites Structures, vol. 60, no. 1, pp. 43–55.

Kilic, H. and Haj–Ali, R. (2003b), "Progressive damage and nonlinear analysis of pultruded composite structures," Composites part B: Engineering, vol. 34, no. 3, pp. 235–250.

Kyriakopoulos, M. K., De Wilde, W. P., Van Hemelrijck, D., and Schillemans, L., (1992), "A finite element approach for thermal–structural response in fibre reinforced composite systems," 3rd International Conference on Computer Aided Design in Composite Material Technology – CADCOMP 92, pp. 599–614.

Lessard, L. B., and Chang, F. K. (1991), "Damage Tolerance of Laminated Composites Containing an Open Hole and Subjected to Compressive Loadings: Part II—Experiment." *Journal of Composite Materials*, 25(1), 44–64.

Lin, S. T., and Rowlands, R. E., (1995), "Thermoelastic stress analysis of orthotropic composites", Experimental Mechanics , vol. 35 , no. 3, pp. 257–265.

Lohr, D. T., Enke, N.F., and Sandor, B.I., (1987), "Analysis of Fatigue Damage Evolution by Differential Infrared Thermography." *Proceedings of the SEM Conference on Dynamic Failure*.

Luong, M. P. (1998), "Nondestructive evaluation of fatigue limit of metals using infrared thermography." *Proceedings of the Materials Research Society Symposium*, 275–280.

Mackenzie, A. K., (1989), "Effects of surface coatings on infrared measurements of Thermoelastic Responses," SPIE, vol. 1084, pp. 59–71.

Mackin, T. J., and Roberts, M.C. (2000), "Evaluation of Damage Evolution in Ceramic–Matric Composites Using Thermoelastic Stress Analysis." *Journal of the American Ceramic Society*, 83(2), 337–43.

Mackin, T. J., and Vernon, P. J., (2001), "Detecting sub–surface cracking in laminated membranes using infrared imaging," Polymer Composites, vol. 22, no.6, pp. 752–761.

Matthews, F.L. and Rawlings, R.D. (1994), *Composite materials: Engineering and Science*, Chapman & Hall, London.

Matlab, (2001), Version 6.1, The MathWorks, Inc, Natick, MA.

O'Brian, T. K. (1993) "Local Delamination in Laminates with Angle Ply Matrix Cracks, Part II: Delamination Fracture Analysis and Fatigue Characterization." *Composite Materials: Fatigue and Fracture, Fourth Volume, ASTM STP 1156*, Philadelphia, 507–538.

O'Brian, T. K. and Hooper, S.J. (1993) "Local Delamination in Laminates with Angle Ply Matrix Cracks, Part I: Tension Tests and Stress Analysis." *Composite Materials: Fatigue and Fracture, Fourth Volume, ASTM STP 1156*, Philadelphia, 491–506.

Oliver, D. E., (1988), "Stress pattern analysis by thermal emission (SPATE), "Experimental Techniques, 3–6, March.

Reifsnider, K. L., Henneke, E.G., II, and Stinchcomb, W.W. (1997) “Delamination in Quasi–Isotropic Graphite–Epoxy Laminates.” *Composite Materials: Testing and Design (Fourth Conference), ASTM STP 617*, 93–105.

Scrivner, G. C. a. C., W.S. (1993) “Effects of Stress Ratio on Edge Delamination Characteristics in Laminated Composites.” *Composite Materials: Fatigue and Fracture, Fourth Volume, ASTM STP 1156*, Philadelphia, 538–551.

Smith, I., Landis, E., and Gong, M. (2003), *Fracture and fatigue in wood*, J. Wiley, Hoboken, NJ.

Swain, R. E., Bakis, C. E., and Reifsnider, K.L. (1993) “Effect of Interleaves on the Damage Mechanisms and Residual Strength of Notched Composite Laminates Subjected to Axial Fatigue Loading.” *Composite Materials: Fatigue and Fracture, Fourth Volume, ASTM STP 1156*, Philadelphia, 552–574.

Talreja, R. (1987), *Fatigue of Composite Materials*, Technomic Publishing Company, Pennsylvania, USA.

Thomson, W., (Kelvin), (1878), “On the thermoelastic, thermomagnetic, and pyro–electric properties of matter,” Phil. Mag., vol. 5, pp. 4–27.

Van Hemelrijck, D., Schillemans, L., De Roey, F., Daerden, I., Boulpaep, F., De Wilde, P., and Cardon, A., (1992), “Thermoelastic stress analysis of fibre reinforced composite systems”, 3rd International Conference on Computer Aided Design in Composite Material Technology – CADCOMP 92, pp. 626–633.

Wang, H., Dinwiddie, R.B., Jiang, L., Liaw, P.K., Brooks, C.R., Klarstrom, D.L. (2000) “Application of high–speed IR imaging during mechanical fatigue tests.” *Proceedings of SPIE – The International Society for Optical Engineering*, 186–193.

Welch, C. S., and Zickel, M. J., (1993), “Thermal coating characterization using thermoelasticity,” Review of Progress in Quantitative Nondestructive Evaluation, vol. 12, Thomson, D. O., and Chimenti, D. E., Eds., Planum Press, NY, NY.

Xian, X., Zheng, W., and Hu, W. (1986) “Evaluation of the Damage of Carbon/Epoxy Composite Laminates under Static and Fatigue Loading by Thermographic Analyses.” *Proceedings of the International Symposium on Composite Materials and Structures*, 710–716.

Yamauchi, T., and Hirano, Hironobu. (2000), “Examination of the onset of stable crack growth under fracture toughness tesing of paper.” *Journal of Wood Science*, 46, 79–84.

Yamauchi, T., and Tanaka, A. (2002), “Tearing test for paper using a tensile tester.” *Journal of Wood Science*, 48, 532–535.

Zhang, D., and Sandor, B.I. (1989), “Thermographic analysis of stress concentrations in a composite.” *Experimental Mechanics*, 29(2), 121–5.

Zhang, D., and Sandor, B.I. (1990), “A Thermoelasticity theory for damage in anisotropic materials.” *Fatigue and Fracture of Engineering Materials and Structures,* 13(5), 497–509.

Zhang, D., Enke, N. F., and Sandor, B. I., (1990), “Thermographic stress analysis of composite materials,” Experimental Mechanics, vol. 30, 1, pp. 68–73.